UNIVERSIDADE DE LISBOA
FACULDADE DE CIÊNCIAS
DEPARTAMENTO DE FÍSICA

Two automated VMAT segmentation approaches: iCycle-Eclipse integration and a native SCP-based algorithm

Tomás da Cruz Gonçalves dos Santos

Mestrado em Engenharia Biomédica e Biofísica

Dissertação orientada por:
Ben Heijmen
Brígida Ferreira

2025

Acknowledgements

Writing this thesis has been a deeply rewarding and intellectually challenging experience. I feel immense gratitude for everyone who walked this path with me, offering their guidance, support, and encouragement when I needed it most.

I would like to express my sincere gratitude to Professor Ben Heijmen, who was the first point of contact in this journey and made this project possible, just as he has done for so many others. I am especially thankful for the way he welcomed all of us who were far from home into his group.

I am deeply grateful to Sebastiaan Breedveld for his guidance and generosity. Our meetings were always thought-provoking, and your endless patience helped me truly understand, rather than simply learn.

I am grateful to the Erasmus Medical Center and the Radiotherapy Department for providing the resources and environment that made this research possible.

This work was also supported by the Erasmus+ Programme, which enabled my academic mobility and internship.

I would like to thank all my colleagues at Erasmus Medical Center for their warm welcome, in particular Jesús, Nicola, Anouk, Manon, Linda, Eva, and Axel.

Quero agradecer à Professora Brígida por todo o apoio que me deu durante a tese, ao Professor Matela por me ter levantado o véu da Física Médica, e à Sandra Vieira por me ter mostrado o caminho.

O meu agradecimento final vai para a minha família. À minha mãe, que me deu asas para voar e um lar para onde voltar. Ao meu avô, que sempre alimentou em mim o sonho da vida académica. À Inês, companheira de uma (pequena) vida, que continua sempre ao meu lado — sem ti, não teria chegado onde estou.

Resumo

A Radioterapia de Intensidade Modulada em Arco (VMAT – *Volumetric Modulated Arc Therapy*) é uma das técnicas mais avançadas e amplamente utilizadas na prática clínica de radioterapia externa. Esta modalidade caracteriza-se por permitir a irradiação contínua ao longo de uma (ou várias) rotação completa ou parcial da cabeça de tratamento em torno do doente. Durante esta rotação, ocorre uma variação simultânea da intensidade do feixe, da posição das folhas do colimador multifolhas (MLC – *Multileaf Collimator*) e da velocidade de rotação da própria cabeça de tratamento. A natureza dinâmica do VMAT possibilita a criação de planos de tratamento com elevada conformidade dosimétrica, permitindo uma melhor adaptação da dose ao alvo e à proteção dos orgãos de risco adjacentes, reduzindo o tempo total de tratamento em comparação com técnicas como a Radioterapia de Intensidade Modulada (IMRT - *Intensity Modulated Radiation Therapy*).

Contudo, obter planos VMAT de elevada qualidade clínica não é uma tarefa simples. O processo de otimização dos segmentos ao longo do arco envolve múltiplas variáveis interdependentes e está sujeito a diversas limitações físicas e geométricas impostas pela unidade de tratamento, ex: acelerador linear. Além disso, a conversão de planos otimizados, como os gerados por software de otimização multi-critério, em formatos tecnicamente válidos pode comprometer a qualidade dosimétrica final se não forem respeitados os constrangimentos do acelerador linear. Neste contexto, o presente trabalho propõe duas abordagens distintas e complementares para a otimização da segmentação VMAT baseada em *Beam's Eye View* (BEV). O objetivo é preservar a distribuição de dose ideal calculada por algoritmos avançados de otimização, garantindo simultaneamente a sua viabilidade clínica em aceleradores lineares convencionais.

A primeira abordagem consiste na análise da integração entre o Erasmus-iCycle, um motor de otimização multi-critério desenvolvido para gerar planos de tratamento Pareto-ótimos, e o sistema de planeamento comercial Eclipse, amplamente utilizado em ambiente clínico. O iCycle permite a definição de listas de desejos ("wish-lists") personalizadas para cada caso clínico, incorporando prioridades específicas para estruturas alvo e orgãos de risco, sem se restringir às limitações impostas pelo equipamento. Por esta razão, os planos produzidos pelo iCycle apresentam frequentemente um perfil idealizado, cuja implementação direta na prática clínica requer processos de conversão e adaptação.

Neste estudo, foram selecionados dez doentes com diagnóstico de adenocarcinoma da próstata. Para cada caso, foi inicialmente gerado um plano de referência no Erasmus-iCycle, com base em critérios clínicos previamente estabelecidos. Esses planos foram depois convertidos, usando o sistema Eclipse, em planos VMAT clinicamente compatíveis com os aceleradores lineares, utilizando uma abordagem automatizada baseada em Objetivos por Linhas (Line Objectives). A avaliação dos resultados foi realizada por meio da análise dos histogramas dose-volume (DVH), com especial atenção às métricas relacionadas com a cobertura do volume-alvo (V95%, D98%), homogeneidade da dose (Dmean, D2%) e proteção dos orgãos de risco (V50Gy e Dmean para bexiga, reto e cabeças femorais). Os dados obtidos revelaram que, em geral, a qualidade dosimétrica dos planos Eclipse foi semelhante à dos planos iCycle, embora se tenham verificado ligeiras perdas na homogeneidade da dose e um aumento marginal da exposição do reto a doses elevadas. Ainda assim, as coberturas dos volumes-alvo permaneceram dentro de critérios clínicos aceitáveis, indicando que, com ajustes apropriados na lista de desejos do iCycle, é possível melhorar a compatibilidade entre os planos de referência e a viabilidade clínica de planos VMAT.

A segunda abordagem desenvolvida neste trabalho testa a implementação de um algoritmo nativo de otimização automática de segmentos VMAT baseado em Programação Sequencial Convexa (SCP - Sequential Convex Programming), implementado em MATLAB. Este método tem como objetivo replicar, com elevada fidelidade, a distribuição de dose gerada pelo iCycle, produzindo diretamente segmentos VMAT viáveis para tratamento no acelerador linear. Ao contrário da abordagem anterior, que depende da segmentação de mapas de fluência, o algoritmo SCP parte diretamente da dose tridimensional como referência e utiliza-a como base para a construção iterativa de um plano de tratamento composto por múltiplos segmentos BEV ao longo do arco.

Em cada iteração, o algoritmo resolve um problema de otimização aproximadamente convexo, cuja função objetivo é baseada na soma dos desvios quadráticos, sujeita a restrições lineares, utilizando o otimizador *quadprog*. A cada passo, os segmentos são atualizados tendo por base a minimização da função objetivo, ajustando as formas geométricas do MLC para aproximar a dose resultante à dose de referência. Foram testadas diferentes configurações de resolução espacial dos beamlets ($5\,mm \times 5\,mm$ e $5\,mm \times 2\,mm$), número de pontos de controlo por arco (72 e 180) e valores de prioridade das estruturas envolvidas. Um dos casos clínicos foi utilizado como teste para avaliar algumas combinações de parâmetros, permitindo identificar a configuração mais adequada, posteriormente aplicada aos restantes nove doentes.

Os resultados demonstraram que os planos gerados pelo algoritmo SCP foram capazes de reproduzir, com grande fidelidade, a distribuição dosimétrica dos planos iCycle. As métricas de cobertura do PTV mantiveram-se dentro dos critérios clínicos, com pequenas diferenças observadas nos valores de V95% e D98%. Verificou-se também uma boa preservação da proteção dos orgãos de risco, com pequenas variações entre os diferentes casos. A principal limitação observada foi o aumento do tempo de cálculo quando se utilizava uma resolução mais fina, o que elevou o tempo total de otimização de cerca de 10 minutos para mais de 2 horas. Contudo, essa configuração apresentou melhorias claras na homogeneidade da dose, especialmente em regiões com estruturas críticas próximas do volume-alvo.

Um dos principais pontos fortes do algoritmo SCP é a sua flexibilidade. O método permite a introdução de restrições adicionais, como a regularidade entre segmentos consecutivos e a penalização de formas geométricas irregulares, o que contribui para a geração de planos mais uniformes, viáveis e robustos à variação mecânica do equipamento. Esta flexibilidade torna o SCP uma ferramenta valiosa para o desenvolvimento de sistemas de planeamento personalizados, com potencial para ser adaptado a diferentes localizações anatómicas e condições clínicas.

Este trabalho também identifica limitações relevantes nas duas abordagens propostas. Na integração iCycle-Eclipse, a principal limitação é a falta de transparência dos algoritmos do Eclipse, dificultando a análise das discrepâncias dosimétricas entre os planos convertidos e os de referência. Para superar isso, sugere-se o desenvolvimento de interfaces mais abertas que permitam maior controlo sobre a segmentação.

No caso do algoritmo SCP, apesar da sua elevada fidelidade dosimétrica, destacam-se a elevada exigência computacional e a dependência de um plano de referência de qualidade. A sua aplicação clínica requer melhorias de eficiência. Além disso, a dependência de planos iCycle bem otimizados levanta a necessidade de explorar abordagens conjuntas de otimização da dose e dos campos viáveis.

Em termos de aplicações clínicas futuras, tanto a abordagem baseada na integração com o Eclipse

como o algoritmo SCP poderão ser adaptados para outros locais anatómicos além da próstata. Situações clínicas com maior complexidade geométrica, como tumores de cabeça e pescoço, pulmão ou ginecológicos, poderão beneficiar substancialmente da capacidade de controlar a forma dos segmentos com base em distribuições de dose previamente otimizadas.

Do ponto de vista clínico, as duas abordagens analisadas são complementares. A integração entre o iCycle e o Eclipse oferece uma solução prática para centros clínicos que pretendem beneficiar da qualidade dosimétrica de otimizadores multi-critério, desde que se faça um ajustamento cuidadoso das listas de desejos. Por outro lado, o algoritmo SCP apresenta-se como uma ferramenta de investigação com grande potencial de aplicação futura, permitindo o controlo total sobre o processo de segmentação VMAT e possibilitando avanços em direção a sistemas de planeamento autónomos.

Em conclusão, este trabalho demonstra que é possível converter planos de tratamento otimizados em formatos compatíveis com os aceleradores lineares, com qualidade dosimétrica equivalente e compatibilidade com os sistemas clínicos. A segmentação BEV surge como uma abordagem eficaz para garantir essa conversão, promovendo uma maior integração entre otimização teórica e prática clínica. O desenvolvimento de algoritmos dedicados, como o SCP, poderá abrir caminho para soluções de planeamento mais inteligentes, automatizadas e adaptáveis à realidade de cada doente, contribuindo assim para a evolução da radioterapia personalizada.

Palavras-chave: VMAT (Volumetric Modulated Arc Therapy), Otimização de Planos de Tratamento, Erasmus-iCycle, Segmentação BEV (Beam's Eye View), Programação Convexa Sequencial (SCP)

Abstract

Volumetric Modulated Arc Therapy (VMAT) is a modern technique in external radiotherapy that allows efficient and highly conformal dose delivery through continuous gantry rotation and dynamic modulation of beam intensity, dose rate, and multileaf collimator (MLC) positions. Despite its advantages, translating idealized fluence maps into clinically deliverable VMAT plans remains a challenging task.

This thesis explores two complementary approaches to optimize VMAT segmentation from a Beam's Eye View (BEV) perspective, aiming to preserve the dosimetric quality of Erasmus-iCycle plans while ensuring compatibility with clinical treatment planning systems (TPS) and linear accelerators (LINACs).

The first approach involves integrating Erasmus-iCycle with the Eclipse TPS. Ten prostate cancer cases were analyzed by converting iCycle-optimized fluence plans into Eclipse-based VMAT formats. Dose-volume histogram (DVH) analysis was used to compare target coverage (V95%, D98%), dose homogeneity (Dmean, D2%), and organ-at-risk (OAR) sparing. While Eclipse preserved the general dosimetric quality, minor trade-offs in heterogeneity and rectal dose were observed, suggesting the need for refined optimization settings.

The second approach introduces a native segmentation algorithm based on Sequential Convex Programming (SCP), designed to emulate the Erasmus-iCycle dose distribution using direct aperture optimization. Implemented in MATLAB, the SCP method was first validated on a test case and then applied across the patient cohort. It produced plans with strong agreement to reference distributions, offering greater flexibility and allowing the inclusion of constraints to enhance deliverability and mechanical stability.

Overall, this work demonstrates the clinical feasibility and value of BEV-driven segmentation strategies, providing a foundation for automated, customizable VMAT planning that can be extended to other treatment sites and advanced radiotherapy techniques.

Keywords: VMAT, Erasmus-iCycle, Treatment Planning Optimization, BEV Segmentation, SCP

Table of Contents

List of Figures

List of Tables

List of Abbreviations

BEV	Beam's Eye View
CT	Computed Tomography
DAO	Direct Aperture Optimization
DNA	Deoxyribonucleic Acid
DVH	Dose Volume Histogram
EBRT	External Beam Radiotherapy
EMC	Erasmus Medical Center
FMO	Fluence Map Optimization
IGRT	Image-Guided Radiotherapy
IMRT	Intensity-Modulated Radiation Therapy
LINAC	Linear Accelerator
MCO	Multicriteria Optimization
MLC	Multileaf Collimator
MRI	Magnetic Resonance Imaging
MU	Monitor Units
OAR	Organ at Risk
PET	Positron Emission Tomography
PTV	Planning Target Volume
RT	Radiotherapy
SCP	Sequential Convex Programming
TNM	Tumor, Node, Metastasis (Staging System)
TPS	Treatment Planning System
VMAT	Volumetric Modulated Arc Therapy

1 Introduction

1.1 Motivation

Modern radiotherapy aims to deliver highly conformal radiation doses to tumor volumes while minimizing exposure to surrounding healthy tissues. Volumetric Modulated Arc Therapy (VMAT) has become a widely adopted technique in this context due to its ability to modulate both the shape and intensity of the radiation beam as the linear accelerator (LINAC) rotates around the patient. However, creating high-quality, deliverable volumetric modulated arc therapy plans remains a complex and time-consuming task that depends heavily on the experience and time availability of treatment planners.

To address this challenge, automated treatment planning systems (TPS) such as Erasmus-iCycle have been developed [1]. Erasmus-iCycle performs multi-criteria optimization to generate Pareto-optimal treatment plans based on pre-defined clinical priorities. While it has demonstrated the ability to produce high-quality dose distributions, it lacks the ability to generate deliverable multileaf collimator segments. As a result, its output must be translated into deliverable plans using clinical TPS, such as Eclipse, or supplemented with custom segmentation algorithms. This integration gap limits the clinical aproval and implementation of fully automated workflows and prevents direct deployment of Erasmus-iCycle plans on a LINAC.

This thesis investigates two approaches for bridging this gap and enabling fully automated VMAT plan generation. The first approach explores the translation of Erasmus-iCycle plans into deliverable Eclipse plans using a technique based on Line Objectives. The second approach evaluates the feasibility of generating deliverable multileaf collimator segments through a native algorithm based on Sequential Convex Programming (SCP), which approximates non-convex segmentation problems through iterative convex subproblems.

The main objective of this work is to assess whether high-quality Erasmus-iCycle plans can be reproduced in a clinically deliverable form using either a commercial TPS or an in-house SCP-based algorithm. By analyzing the dose distributions and deliverability of reconstructed plans for a cohort of prostate cancer patients, this study aims to provide insights into the effectiveness, limitations, and potential of both integration strategies. The findings are expected to contribute to the development of more efficient and robust automated planning pipelines in radiotherapy.

1.2 Cancer

Cancer is a disease characterized by the uncontrolled proliferation of mutated cells, which are subject to evolutionary pressures through natural selection [2]. According to the somatic mutation theory, cancer originates from the accumulation of mutations in genes that regulate cell growth and division. These mutations disrupt normal control mechanisms, resulting in unchecked cellular multiplication [3]. Since the referred mutations can appear in any tissue there are a range of different cancers, each with unique characteristics. [4].

In healthy multicellular organisms, malfunctioning or damaged cells are typically removed through processes such as apoptosis, a programmed cell death through which the cell is removed from the body [5], or autophagy, where the cell is broken down and recycled [6]. When these regulatory mechanisms fail due to genetic mutations, the affected cells may avoid destruction and continue to proliferate abnormally.

This can lead to the formation of a mass of tissue known as a tumor. If left untreated, the expanding tumor may disrupt the normal function of surrounding organs and tissues [4].

Tumors can be classified as either benign or malignant. Benign tumors do not invade surrounding tissues or spread to distant body locations; they often exhibit high rates of apoptosis and generally pose no immediate threat to life. In contrast, malignant tumors are cancerous and have the potential to invade nearby structures and metastasize to distant parts of the body via the bloodstream or lymphatic system [4]. Due to their aggressive nature, malignant tumors often require urgent medical intervention to prevent further progression and systemic complications.

1.3 Cancer treatment workflow

While the specific course of cancer treatment may vary depending on the cancer type, stage, and patient-specific factors, the overall clinical workflow generally follows four main phases: diagnosis, pre-treatment, treatment, and follow-up care.

1.3.1 Diagnosis

The first phase of the cancer treatment workflow is diagnosis, during which the presence of a tumor is confirmed. Depending on the suspected type and location of the cancer, physicians may recommend one or more diagnostic tests.

Imaging techniques such as X-rays, computed tomography (CT), magnetic resonance imaging (MRI), and positron emission tomography (PET) scans are commonly used to detect tumors and assess their size and location. Imaging techniques play a key role in diagnosing cancers, including ovarian [7], breast [8], colorectal [9], lung [10], and head and neck cancers [11].

Biopsies involve extracting tissue samples from suspected tumors for microscopic analysis to confirm if it is cancerous. Techniques include image-guided percutaneous biopsies [12], endoscopic biopsies [13], and surgical biopsies [14].

Blood tests can detect cancer-related biomarkers, such as tumor antigens or cell-free DNA, offering non-invasive diagnostic insights [15]. An example is CancerSEEK, a test designed to screen for multiple cancers [16].

Endoscopy, using a camera-equipped flexible tube, allows direct visualization and tissue sampling from internal organs, especially useful in cancers such as esophageal cancer [17, 18].

The choice of diagnostic method depends on tumor characteristics and patient-specific factors. Early and accurate diagnosis is crucial for timely intervention and improved outcomes [19, 20].

1.3.2 Pre-Treatment

The pre-treatment phase focuses on developing a personalized treatment plan tailored to the patient's specific diagnosis and clinical context. This plan is based on several critical factors, most notably the type and stage of cancer.

The type of cancer refers to the specific cells that have undergone malignant transformation, such as in prostate cancer, lung cancer, or leukemia. Accurate identification is essential, as different cancer types

vary in biological behavior and require distinct therapeutic strategies.

Cancer staging describes the extent of disease progression and is a key determinant in treatment planning. It considers tumor size, lymph node involvement, and the presence of metastasis. Staging guides the choice, sequencing, and intensity of treatments, and is typically performed using the Tumor, Node, and Metastasis (TNM) classification system [21].

1.3.3 Treatment

Cancer treatment involves a range of therapeutic approaches, often used in combination to enhance effectiveness and improve outcomes [22]. The main treatment modalities include surgery, chemotherapy, hormonal therapy, and radiotherapy.

Surgical intervention involves the removal of part or all of the affected tissue and is frequently the first-line treatment for many cancers [23]. Its primary goal is to physically eliminate the tumor. In early-stage cancers, surgery may offer a curative outcome, while in more advanced stages, it can serve a palliative role by relieving symptoms or reducing tumor size.

Chemotherapy and hormonal therapy are systemic treatments that target cancer cells throughout the body. Chemotherapy uses cytotoxic drugs that kill rapidly dividing cells, including cancerous ones [24]. Hormonal therapy is used specifically for hormone-sensitive cancers, such as breast and prostate cancer [25, 26]. It works by blocking the effects of hormones or suppressing their production to slow cancer progression.

Radiotherapy (RT) uses ionizing radiation to damage the DNA of cancer cells, impairing their ability to grow and divide, ultimately leading to cell death [27]. It can be delivered externally via external beam radiotherapy (EBRT) or internally through brachytherapy or radionuclide therapy. In non-curative settings, RT is also used for palliative purposes, aiming to alleviate symptoms and enhance quality of life [28].

Treatment selection is guided by a multidisciplinary team comprising oncologists, radiologists, medical physicists, and other specialists. Together, they develop a personalized treatment protocol tailored to the specific type and stage of cancer. This individualized approach helps optimize treatment efficacy and patient outcomes [29].

1.3.4 Post-Treatment (or Follow-up care)

Follow-up care is a vital part of cancer management, aimed at monitoring patients after treatment to detect recurrence and manage long-term side effects. It involves regular check-ups and diagnostic tests, with the frequency tailored to individual risk factors [30, 31].

1.4 Basics of Radiotherapy

RT is a non-invasive cancer treatment that uses high-energy ionizing radiation to destroy cancer cells. The therapeutic goal of RT is to deliver a sufficient dose to eradicate the tumor while minimizing exposure to surrounding healthy tissues. Achieving this balance is critical to maximizing treatment effectiveness and reducing side effects [28].

1.4.1 Physics of radiotherapy

Radiation is a form of energy that travels as waves or particles and can be categorized into electromagnetic radiation, such as X-rays and gamma rays, and particle radiation, like protons and neutrons.

RT relies on ionizing radiation, whether electromagnetic or particle-based, which has enough energy to remove tightly bound electrons from atoms. This ionization process generates free radicals and directly damages cellular DNA, making it a powerful tool for destroying cancer cells [28].

This thesis focuses specifically on the use of electromagnetic ionizing radiation in RT, particularly X-rays (also referred to as high-energy photons).

1.4.1.1 Photon production

High-energy photons used in RT are commonly generated by directing accelerated electrons onto a high atomic number target, typically tungsten. When these electrons interact with the target material, they decelerate rapidly and change direction, emitting bremsstrahlung radiation [32]. Discrete X-ray emission lines characteristic of the target may also be present, though at the high energies used in EBRT (6–15 MV), these lines are negligible. This process is fundamental to the operation of a LINAC, the standard device in EBRT. LINACs generate high-energy photons capable of penetrating deep into tissues, with their dose distribution described by the percentage depth dose (PDD) curve. As shown in Figure 1.1, the PDD represents the relative dose deposited at different tissue depths, normalized to the maximum dose point.

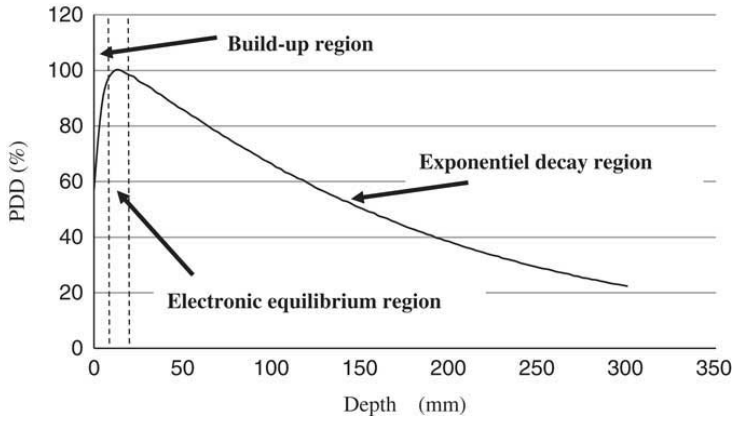

Figure 1.1: Percentage depth dose (PDD) curve for a LINAC using high-energy X-ray photons. The curve illustrates the dose distribution as a function of depth in tissue, showing the characteristic build-up region, peak dose, and gradual dose fall-off due to attenuation and scattering.

Alternatively, high-energy photons can be produced via the natural radioactive decay of certain isotopes, a phenomenon first observed by Henri Becquerel in 1896 [33]. These radioactive sources are used in diferent RT techniques. Brachytherapy places sealed sources directly inside or near the tumor, while radionuclide therapy delivers unsealed radioactive compounds systemically. Radiosurgery techniques, such as Gamma Knife, use focused photon beams (often from Cobalt-60 sources) for precise, high-dose treatments.

Although all these methods are used clinically, EBRT is the most widely adopted due to its non-invasive nature and treatment flexibility [34].

1.4.1.2 Photon interactions

Once produced, photons interact with matter through various mechanisms, depending on their energy and the atomic number of the target material. In the context of photon beam RT, three major interactions are relevant: photoelectric effect, Compton scattering and pair production.

In the photoelectric effect, a photon transfers all its energy to an inner-shell electron, ejecting it from the atom and causing ionization. The photon is completely absorbed in the process. This effect is more prominent at lower photon energies and in materials with high atomic numbers. It was first explained by Einstein [35].

In Compton scattering, a photon transfers part of its energy to an outer-shell electron, freeing it from the atom and scattering the photon at a lower energy and different direction [36]. This interaction dominates in soft tissue at the energy levels typically used in EBRT (6–15 MV).

At photon energies above 1.022 MeV, the photon can interact with a nucleus to produce an electron-positron pair. This pair production results in the complete absorption of the photon's energy and is more significant at higher energies [37].

The biological effects of radiation come from the transfer of photon energy to cellular material, quantified as absorbed dose. This is defined as the energy deposited per unit mass and is measured in grays (Gy), where $1\,Gy = 1\,J/kg$ [38]. Ionizing radiation primarily affects cells by damaging DNA—the key target in RT [27].

Radiation-induced DNA damage occurs through two main mechanisms. In direct action, radiation ionizes DNA molecules directly. In indirect action, it interacts with water molecules to generate free radicals, which then damage DNA. In photon RT, indirect action is the dominant pathway. In contrast, proton therapy primarily induces DNA damage via direct ionization [34, 39].

1.5 External Beam Radiotherapy

A key characteristic of EBRT, as introduced in Section 1.4.1.1, is that the radiation source is located outside the patient's body. The most commonly used device for EBRT is the LINAC, shown in Figure 1.2. During treatment, high-energy X-ray beams are generated and precisely directed toward the tumor using a rotating gantry, which can move 360º around the patient. The patient lies on a treatment couch while multiple beams from different angles are used to concentrate dose delivery at the tumor site, thereby sparing surrounding healthy tissue [34].

Figure 1.2: Two medical LINACs; Left: Elekta Infinity (Photo: Elekta AB); Right: Varian Vitalbeam (Photo: Varian Medical Systems);

Standard EBRT beam delivery involves a rotating gantry and a stationary couch, enabling coplanar beam arrangements in which all beams lie within a single geometric plane (Figure 1.3a). For more complex tumor geometries, non-coplanar arrangements, achieved by rotating both the gantry and the couch, can offer improved dose conformity (Figure 1.3b). These setups provide greater flexibility in beam angles, enhancing treatment quality. However, non-coplanar techniques are often more time-consuming and require couch adjustments, typically performed and verified by RT technician [40].

Some specialized systems, such as CyberKnife, overcome this limitation by mounting the LINAC on a robotic arm. This allows for automated, highly maneuverable non-coplanar beam delivery without the need for manual intervention, increasing both precision and efficiency.

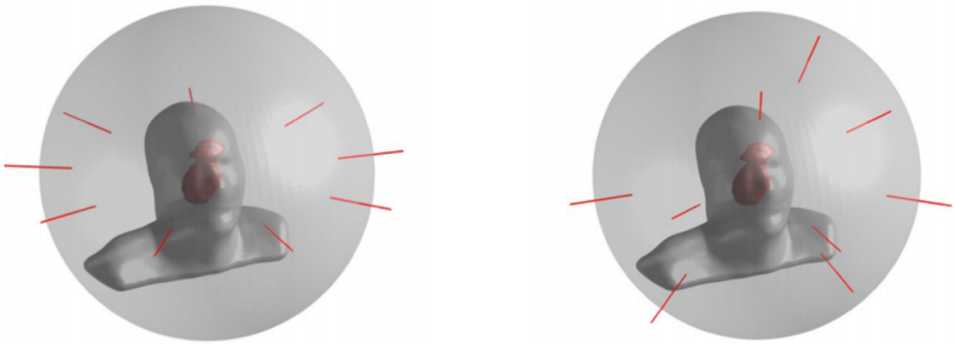

(a) Coplanar **(b)** Non-Coplanar

Figure 1.3: Possible treatment geometries for a) coplanar and b) non-coplanar beam arrangements. In coplanar beam arrangements, all beams are in the same plane, and only the gantry rotates; in non-coplanar beam arrangements, both the gantry and the couch rotate. Adapted from [41]

1.5.1 Modern RT Delivery Techniques

Technological advances over the past few decades have transformed RT, enabling more precise and effective treatments. These innovations have led to the development of advanced planning and delivery techniques that significantly improve dose conformity and reduce exposure to healthy tissues. Two major milestones in this evolution are image-guided radiotherapy (IGRT) and intensity-modulated radiotherapy (IMRT) [42, 43].

1.5.1.1 Image-guided radiotherapy

IGRT integrates imaging techniques such as CT, MRI, or ultrasound before and/or during treatment to monitor the tumor and surrounding anatomy, comparing their positions with the planning setup. IGRT improves treatment accuracy by accounting for tumor motion and anatomical changes that can occur throughout the course of therapy. Variations due to breathing, bladder and bowel filling, or slight patient positioning shifts can alter the tumor's shape, size, or location. By detecting these changes in real time, IGRT enables on-the-fly adjustments to the radiation beams, ensuring precise targeting [44].

This approach is especially valuable for tumors located near critical organs where small deviations could lead to significant healthy tissue damage. By reducing geometric uncertainties, IGRT supports the delivery of higher tumor doses while minimizing exposure to surrounding tissues, ultimately lowering toxicity and improving clinical outcomes [45].

1.5.1.2 Intensity-modulated radiation therapy (IMRT)

IMRT is an advanced RT technique that uses multiple radiation beams with varying intensities to precisely shape the dose distribution around a tumor. Unlike conventional conformal RT, which delivers a uniform dose, IMRT uses inverse planning to determine the optimal beam intensities and shapes that best achieve the prescribed dose distribution while minimizing exposure to surrounding healthy tissue [46].

In IMRT, each beam is divided into smaller segments or subfields (Figure 1.4c) using a multi-leaf collimator (MLC, Figure 1.4a). Each segment has a distinct shape tailored to conform closely to the tumor's geometry (Figure 1.4b). This allows for highly conformal dose distributions, enabling dose escalation to the tumor while reducing radiation to nearby organs at risk [47, 48].

(a) MLC

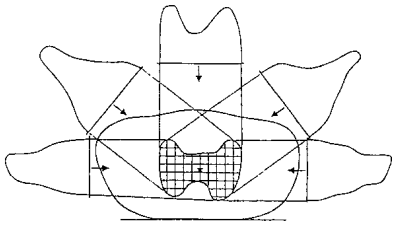

(b) IMRT

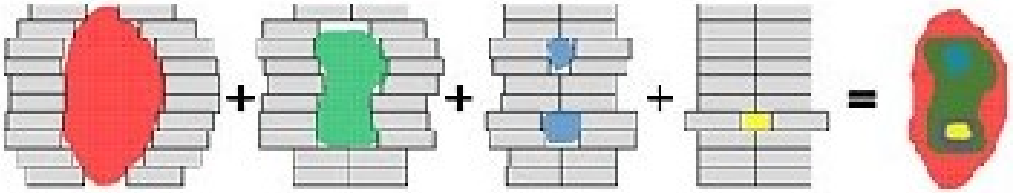

(c) Subfields in IMRT

Figure 1.4: (a) Photograph of the Millennium 120-leaf multileaf collimator (MLC) from Varian. (b) Schematic illustration of the IMRT concept based on Brahme's original principle (1988) (c) Example of how IMRT uses subfields with varying intensities thus producing an intensity modulated pattern for one irradiation direction. These subfields are modulated to shape the dose distribution, enabling high tumor coverage (represented by the curve) while minimizing exposure to nearby healthy organs. Adapted from [49]

The use of inverse planning is a key feature of IMRT. Instead of manually adjusting beam parameters, the planner defines clinical objectives and the planning system calculates the optimal beam intensities and segment shapes to meet those goals. This approach increases flexibility and precision in treatment planning, often resulting in improved clinical outcomes and reduced toxicity [46].

IMRT is considered the gold standard for EBRT due to its superior dose conformity and target coverage. However, its planning process is complex, requiring the optimization of multiple parameters, including beam angles, dose objectives, and organ-at-risk tolerances. In current clinical practice, beam geometries are often selected using site-specific templates or manual input from experienced planners. While plan quality can be refined through iterative adjustments, it remains partially dependent on the planner's expertise. Personalized beam configurations—when optimally selected—can further enhance treatment outcomes by improving tumor coverage and sparing healthy tissue [50].

1.5.1.3 Volumetric modulated arc therapy

VMAT is an advanced RT technique in which radiation is delivered continuously as the treatment machine's gantry rotates around the patient. Unlike static-field IMRT, which uses fixed beam angles, VMAT dynamically modulates beam intensity, dose rate, and MLC positions throughout the arc, resulting in highly conformal dose distributions with greater delivery efficiency [51, 43].

VMAT is especially effective for treating complex tumor geometries or tumors located near critical structures, even more than IMRT. By using one or more full or partial arcs, each individually optimized, VMAT enables personalized plans that enhance target coverage while sparing surrounding healthy tissues. Compared to static-field IMRT, VMAT typically achieves comparable or superior dose conformity and homogeneity (Figure 1.5), while significantly reducing treatment time and the number of monitor units (MU) required [48, 43].

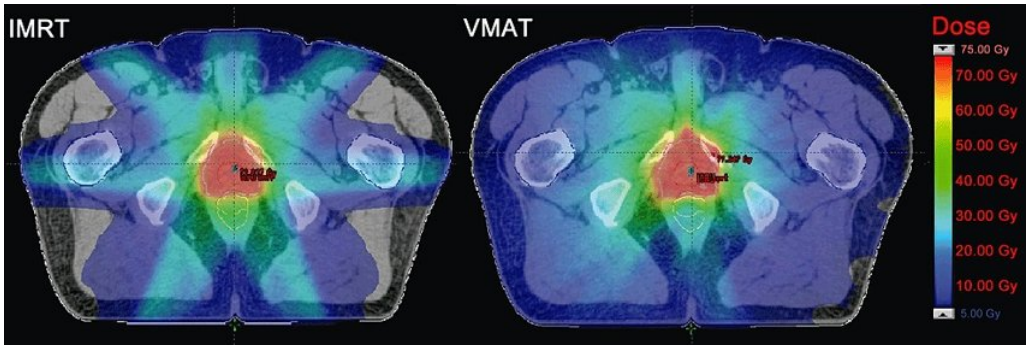

Figure 1.5: Comparison of dose distributions between IMRT and VMAT. IMRT (left) delivers radiation using multiple static beams, each with individually modulated intensity, while VMAT (right) delivers radiation dynamically as the gantry rotates around the patient. VMAT provides similar or improved dose conformity with reduced treatment time and fewer monitor units, enhancing treatment efficiency. Adapted from [52]

The success of VMAT relies on precise MLC control, ensuring that the beam conforms to the tumor shape throughout the arc (Figure 1.4a). As discussed in Section 1.5.1.2, accurate MLC segmentation plays a critical role in treatment quality, with optimized modulation contributing to improved clinical outcomes.

2 VMAT MLC Segmentation

RT teams typically follow a general treatment workflow that involves importing patient data into a TPS, generating a treatment plan, and delivering it using a LINAC. However, at the Erasmus Medical Center (EMC) in Rotterdam, The Netherlands, a more streamlined and efficient workflow has been developed through the full automation of treatment plan optimization.

The process begins with loading patient data into Erasmus-iCycle [53], a specialized in-house developed software that generates an optimal treatment plan. This plan is subsequently imported into the clinical TPS, Eclipse (Varian Medical Systems, Inc., Palo Alto), where any necessary manual adjustments can be made. Once finalized, the treatment plan is transferred via the department's Record & Verify system to the treatment room, where the LINAC uses it to deliver radiation to the patient.

The following sections will describe the EMC workflow in more detail, with particular emphasis on the role and significance of a native automated MLC segmentation algorithm. Automating this component has the potential to further enhance treatment plan quality and clinical efficiency.

2.1 Radiotherapy Treatment Planning

As mentioned in Section 1.3.2, a treatment plan must be created before any RT treatment can begin. In this thesis, the focus is specifically on treatment planning for VMAT. The primary objective of radiotherapy treatment planning is to define the beam parameters that achieve an optimal balance between delivering an effective dose to the target volume and minimizing exposure to surrounding healthy tissues [34].

The planning process typically starts with the acquisition of a CT scan. The resulting images are reviewed, and relevant anatomical structures are identified and delineated on each CT slice. These structures include the target (referred to as the Planning Target Volume (PTV)), which includes the tumor plus a margin to account for uncertainties, and the surrounding organs at risk (OARs) (Figure 2.1). In some cases, MRI or positron emission tomography PET scans are also used to assist in this delineation process [54, 55].

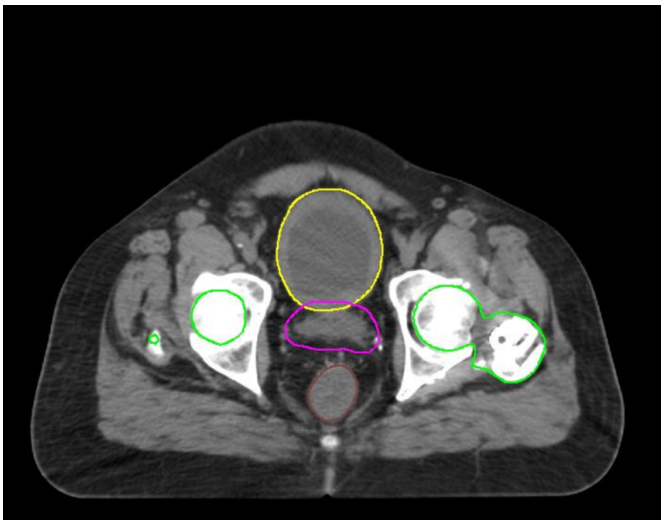

Figure 2.1: An example slice of a CT image from a prostate cancer patient is shown, with the following anatomical structures delineated: Bladder (yellow), Planning Target Volume (PTV) (magenta), Rectum (brown), Left and Right Femurs (green). From [56]

The quality of a treatment plan is influenced by multiple factors, including the treatment modality, the anatomical location and size of the target, the prescribed dose, and the number and configuration of beams or arcs used.

To achieve the best possible clinical outcomes, a multidisciplinary team , comprising radiation oncologists, medical physicists, and radiotherapy technicians, collaborates to develop a treatment protocol tailored to each anatomical site. This protocol includes the prescribed dose, fractionation schedule, dosimetric objectives, and the radiotherapy technique to be employed [57]. Nonetheless, the final treatment plan is always individualized to the patient's anatomy, ensuring that protocol guidelines are adapted to the specific clinical context.

2.1.1 Clinical VMAT treatment plan generation

Within the TPS, the planner is responsible for creating a personalized treatment plan for each patient. This process begins with importing the patient's CT scan, which includes delineated target volumes and OARs. Based on clinical experience and established treatment protocols, the planner determines the number and configuration of beams or arcs to be used.

Subsequently, inverse planning optimization is initiated. In this stage, the planner chooses priority values for each anatomical structure. These values influence the weight of corresponding objectives and constraints within the cost function, guiding the optimization process to reflect the specific clinical goals of the case. The TPS then computes a dose distribution that meets these priorities as closely as possible. If the resulting plan does not meet clinical requirements, the planner may manually adjust the objective weights or modify the beam or arc geometry before re-running the optimization.

In VMAT, the radiation dose is delivered continuously as the gantry rotates around the patient. However, for planning and optimization purposes, this rotation is discretized into a series of control points. Each control point corresponds to a specific gantry angle and defines the instantaneous configuration of the treatment machine, including MLC leaf positions, dose rate, and other relevant parameters. The full VMAT plan is composed of a sequence of such control points, each contributing to the overall dose distribution. The number of control points influences the granularity of modulation and plays a key role in dose conformity and delivery accuracy.

This iterative trial-and-error approach makes clinical treatment planning both time-consuming and variable in quality, depending heavily on the planner's experience and the time available for planning [58, 59, 60].

One of the primary tools for evaluating the quality of the resulting treatment plan is the dose-volume histogram (DVH). The DVH provides a concise, graphical summary of the dose distribution within the patient, illustrating the relationship between dose levels and the percentage of a structure's volume receiving those doses. On a DVH, the y-axis represents the percentage of the structure's volume (ranging from 0% to 100%), and the x-axis represents dose, expressed either as an absolute value or as a percentage of the prescribed dose. The curve indicates, for each dose level, the percentage of the volume that receives at least that dose. For example, at a dose level of 90%, a DVH showing a value of 50% means that half of the target volume receives 90% or more of the prescribed dose (Figure 2.2). This allows clinicians to assess the adequacy of target coverage.

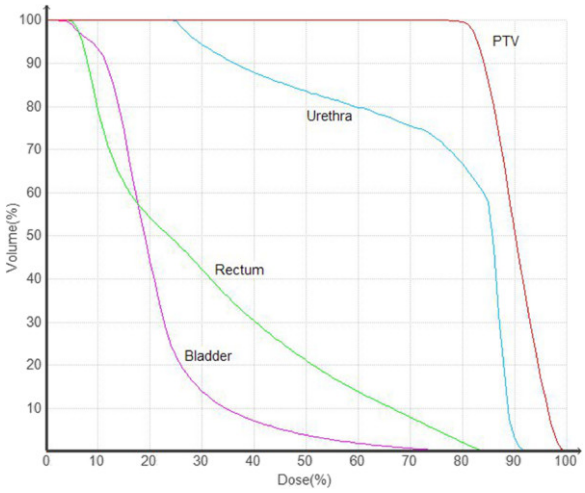

Figure 2.2: An example of a typical dose volume histogram (DVH) for the target (PTV) and normal tissues. From [62]

DVHs can also be generated for OARs to evaluate how much radiation they receive. This helps ensure that dose constraints are respected and radiation-induced toxicities are minimized. The DVH thus provides critical insights into whether the plan achieves a desirable balance between effective tumor control and normal tissue sparing.

By analyzing the DVH, planners can identify areas for improvement in the treatment plan, for instance, increasing the dose to under-covered regions of the PTV or reducing dose to critical structures. The DVH also helps to detect and avoid hot spots ($\geq 110\%, 107\%$ or 105% of the prescribed dose) and cold spots ($\leq 100\%$ of the prescribed dose within the PTV), both of which are indicators of suboptimal dose distribution.

Overall, the DVH is an essential tool in RT planning. It offers a quantitative assessment of dose distribution and supports clinical decision-making, ultimately contributing to the delivery of safe, effective, and personalized treatments [61].

In radiotherapy, the dose distribution refers to the spatial pattern of radiation deposited in the patient's anatomy. It is typically represented in three dimensions and used to visualize how the prescribed dose is spread across the target volume and surrounding organs at risk. A high-quality dose distribution provides uniform coverage of the target while minimizing dose to healthy tissue.

Dose statistics are quantitative measures extracted from the dose distribution. They include metrics such as the mean dose, maximum dose, and minimum dose to a given structure, as well as volumetric indicators like D_{95}(the dose received by 95% of a structure) or V_{70} (the volume percentage receiving at least 70 Gy). These metrics are used to evaluate whether clinical goals and constraints have been met, and they form the basis of comparative plan assessment.

2.2 Automated radiotherapy treatment planning with Erasmus-iCycle

Erasmus-iCycle is the in-house TPS developed for fully automated MCO of RT treatment plans [53]. It simultaneously optimizes beam intensity profiles and beam angles to produce high-quality plans tailored to specific clinical goals. Erasmus-iCycle has been successfully applied in the treatment of a wide range of cancers, including head and neck [63], cervical [64], lung [65], spinal metastases [66], prostate [1, 67], and advanced gastric cancer [68].

In contrast to manual planning, Erasmus-iCycle does not require planners to iteratively adjust priority values throughout the optimization process. By eliminating this manual intervention, the system significantly reduces hands-on planning time while maintaining consistent plan quality. It relies on a treatment site-specific configuration, known as a 'wish-list', that encodes clinical priorities and dosimetric trade-offs [69]. The resulting plans are Pareto-optimal, meaning that any improvement in one objective necessarily involves a compromise in at least one other objective.

As this thesis focuses specifically on VMAT treatments, the discussion will center on Erasmus-iCycle's automated optimization of beam intensity profiles. This is particularly relevant for VMAT, where treatments are delivered using arcs rather than discrete beams.

2.2.1 Details of Erasmus-iCycle for plan generation

Erasmus-iCycle performs MCO by simultaneously accounting for all competing requirements defined by the user. These requirements are specified for each treatment site in the wish-list. Two types of treatment planning elements, referred to as "wishes", can be included in a wish-list:

- **Constraints** are hard limits that must always be satisfied and are not subject to further optimization;
- **Objectives** represent prioritized treatment goals that should be achieved as closely as possible without violating any constraints.

A critical aspect of this optimization process is the prioritization of objectives. Objectives are assigned hierarchical importance, where higher-priority goals must be satisfied before considering lower-priority ones. Throughout the process, all constraints are strictly enforced.

The optimization proceeds in two phases. In the first phase, each objective is minimized sequentially in order of priority, while ensuring compliance with the constraints and any higher-priority objectives already optimized. After optimizing an objective, a new constraint is introduced, either based on the achieved result or the original goal value (if feasible), to lock in the improvement. This ensures that lower-priority objectives cannot compromise the results achieved for higher-priority ones. As a result, lower-priority objectives are subject to an increasing number of constraints. In the second phase, only the objectives that reached their desired goal values in the first phase are optimized again, in accordance with their original priority and under all defined constraints. The final output is a single Pareto-optimal plan that provides a clinically favorable balance of all requirements outlined in the wish-list.

The process of developing a wish-list begins with an initial guess based on the institution's clinical protocol. This starting point is refined through an iterative four-step cycle:

1. Generate plans for a small group of patients using the initial wish-list.
2. Evaluate and compare these automated plans with clinically accepted reference plans.
3. Adjust the wish-list to better reflect physician preferences and improve dosimetric outcomes.
4. Repeat the process until no further meaningful improvements are observed.

This iterative refinement ensures that the wish-list evolves to align with clinical expectations and maximizes plan quality [69].

By mimicking clinical planning strategies, Erasmus-iCycle is capable of producing automated plans that satisfy institutional planning objectives and dosimetric trade-offs. Furthermore, the iterative nature of wish-list development inherently drives improvement, allowing automated plans not only to meet but often to exceed the quality of manually generated clinical plans [64, 70, 63].

Through this approach, automated planning becomes a powerful tool to achieve consistent, high-quality treatment plans that support better patient outcomes.

2.2.2 From Erasmus-iCycle to Eclipse deliverable plans

Erasmus-iCycle is currently used as a pre-optimizer in clinical workflows. While it generates high-quality, Pareto-optimal treatment plans, these plans must be reconstructed within a clinical TPS to be deliverable by a LINAC [70, 1]. At EMC, Erasmus-iCycle is integrated with Eclipse TPS, as described in Section 2.1.1, enabling the translation of Erasmus-iCycle plans into clinically deliverable plans.

This integration enables the automated creation of plan templates in Eclipse, using the dose distributions generated by Erasmus-iCycle as a reference. A central component of this process is the use of Eclipse's "Line Objectives," which allow planners to define a set of dose-volume pairs that approximate the desired dose distribution. Each pair specifies a dose value and the corresponding volume of a structure that should receive at least (or at most) that dose. By combining multiple pairs into a continuous objective curve, the TPS is guided to reproduce the original Erasmus-iCycle dose distribution as closely as possible. These Line Objectives serve as flexible, shape-based constraints that steer the Eclipse optimizer toward a clinically acceptable plan that mirrors the Erasmus-iCycle outcome [71, 72]. Internally, this conversion process is referred to as "translation." Once fully implemented, it can be applied automatically across patients, significantly enhancing the efficiency of the planning workflow.

One of the goals of this thesis is to evaluate the feasibility of this translation process using Line Objectives. If successful, this approach enables the fully automated, multi-criteria generation of VMAT plans that are clinically deliverable. Such plans can match or surpass the quality of those produced by experienced planners while substantially reducing the time required for manual planning [1].

Accurate MLC segmentation is essential for VMAT plan deliverability. However, a current limitation of Erasmus-iCycle is its inability to produce a set of MLC segments capable of delivering the optimized fluence pattern as part of the output. This limitation highlights the need for additional segmentation strategies to bridge the gap between optimization and delivery.

2.2.3 The non-convex mathematical formulation of segmentation

The MLC is a key component of modern radiotherapy delivery systems, consisting of an array of movable tungsten leaves (see Figure 1.4a). These leaves dynamically shape the radiation beam to conform to the tumor's geometry while minimizing exposure to surrounding healthy tissue. Optimizing the MLC apertures involves determining the ideal leaf positions at each control point to deliver the prescribed dose to the PTV while sparing OARs. This process is complex due to the high dimensionality of the problem and the presence of competing clinical objectives and constraints.

A critical intermediate step in this process is fluence map optimization (FMO), where the goal is to compute the optimal intensity pattern, or fluence, of the radiation beam across the treatment field. The fluence map represents how much radiation is delivered through each beamlet (a small subregion of the

beam) and is optimized to achieve the desired dose distribution in the patient. Once an optimal fluence map is determined, the challenge becomes translating this idealized intensity pattern into a physically deliverable set of MLC apertures and associated weights.

An alternative to this traditional two-step approach is Direct Aperture Optimization (DAO). DAO integrates the deliverability constraints of the LINAC directly into the optimization problem by treating aperture shapes and their associated weights as the primary decision variables. This allows the optimization algorithm to generate deliverable apertures from the outset, without requiring a separate segmentation step. DAO has the potential to improve delivery efficiency and reduce monitor units, but its highly non-convex nature makes the optimization problem more difficult to solve, often requiring heuristic or advanced global search methods.

In the context of constrained segmentation optimization, the objective is to maximize PTV coverage and dose homogeneity while respecting strict constraints on the maximum and mean doses to both the PTV and OARs. However, the relationship between machine parameters, specifically, MLC leaf positions and their associated aperture intensities, and the resulting dose distribution is non-convex. This non-convexity arises from both the physical limitations of the LINAC and the complex dose deposition dynamics within the patient's anatomy, making the overall optimization problem particularly challenging to solve using standard methods [73].

Radiotherapy treatment planning description

IMRT planning involves dividing the total radiation dose into smaller, spatially modulated sub-fields, which are delivered from multiple beam angles. During treatment delivery, the MLC dynamically shapes the radiation field for each sub-field, while the beam intensity is modulated to produce a dose distribution that conforms closely to the tumor volume and spares surrounding healthy tissues.

Figure 2.3 illustrates a simplified representation of this process, considering a single beamlet. The optimization procedure begins by discretizing the radiation field into beamlets, small, rectangular elements defined by the MLC leaf pairs. Each beamlet represents a unit of radiation fluence. These beamlets are arranged in a grid for each beam direction, forming what is known as a fluence map. The fluence delivered through each beamlet contributes to the dose received by the patient, which is discretized into voxels within the volume of interest.

The dose distribution within the patient can be modeled as a linear function of the beamlet intensities:

$$d = d(x) = Ax \tag{1}$$

Here, x is a vector containing the intensities of all beamlets across all beams (i.e., the complete fluence maps), and d is a vector representing the dose received by each voxel. The matrix A, known as the *dose influence matrix* or *pencil-beam matrix*, defines how much dose is deposited in each voxel by a unit intensity from each beamlet. This matrix is patient-specific and is computed using the planning CT. While this formulation is mathematically convenient, it discards the spatial context of both voxels and beamlets, as they are represented only as indexed elements in the vectors x and d.

The optimization problem thus consists of finding the optimal fluence maps x, such that the resulting dose distribution $d = Ax$ satisfies a set of clinical objectives and constraints. However, despite the linear relationship between dose and fluence, the overall optimization problem is often non-convex due

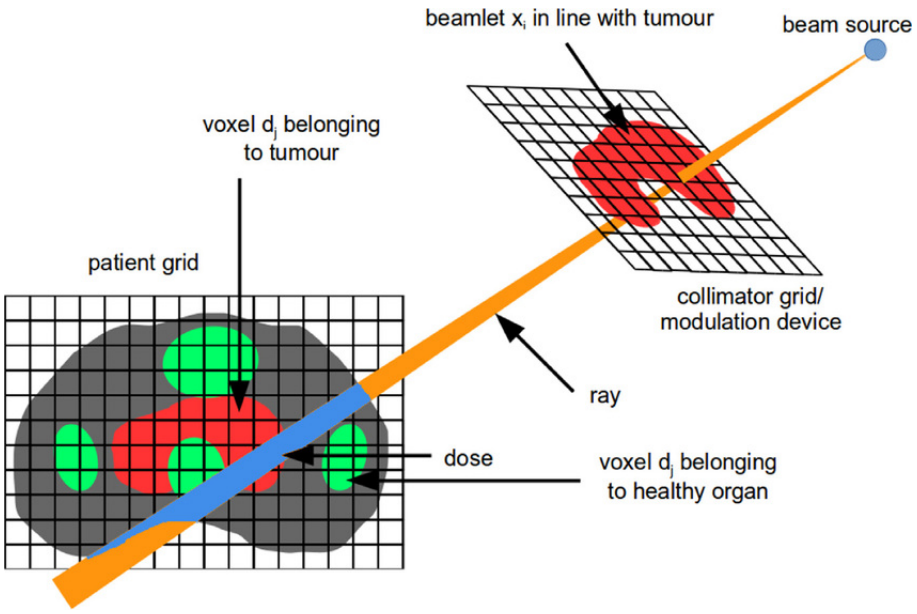

Figure 2.3: Radiotherapy problem decomposition: Radiotherapy uses ionizing radiation that originates from a beam source and is shaped by a multileaf collimator (MLC), which defines the beam's geometry. For optimization purposes, the beam fluence is discretized into small elements called beamlets. The longer a beamlet remains "open," the higher its intensity, resulting in a greater dose delivered to the patient. As the radiation from each beamlet interacts with tissue, it deposits energy in the form of dose. For accurate dose calculation, the patient's body is discretized into voxels. Intensity modulation is achieved by delivering a series of different MLC segments, allowing precise control of the dose distribution for each irradiation direction. From [74]

to the presence of competing clinical goals and non-linear constraint. Various solution methods have been proposed to address this complexity, including global optimization techniques such as simulated annealing [75], as well as more computationally efficient gradient-based methods [76]. Nonetheless, due to the high dimensionality of the problem and the intricate trade-offs involved, identifying globally optimal solutions remains a significant challenge.

The objective function

Optimization in RT treatment planning is guided by an objective function, a mathematical expression that defines the desired radiation dose distribution within the patient and directs the search for an optimal solution. This function incorporates clinical goals through a combination of hard and soft constraints, such as maximum and mean dose limits for OARs and the PTV. The optimization algorithm adjusts the beamlet intensities to minimize the value of the objective function while satisfying all imposed constraints.

Typically, the objective function is composed of two main components. The first penalizes deviations from the prescribed dose, encouraging solutions that closely match clinical targets. The second penalizes excessively high beamlet intensities, which can lead to dose inhomogeneities or hot spots. This promotes a smoother and more uniform dose distribution throughout the treatment volume.

One commonly used objective function is the quadratic penalty function, which is based on the sum of squared deviations from the desired dose distribution. This function penalizes deviations from the desired dose and encourages a smooth and uniform dose distribution. Other functions may be based on points of DVHs (Section 2.1.1) or objectives/constraints, which provide a graphical representation of the dose distribution within the patient's body, or on statistical models that relate the dose distribution to the probability of tumor control or normal tissue complications.

A commonly used form of the objective function is the quadratic penalty function, which minimizes the sum of squared differences between the calculated and prescribed doses. This approach not only steers the solution toward the desired dose distribution but also enforces spatial smoothness. Alternative formulations may use metrics derived from DVHs (Section 2.1.1) or incorporate biological models that estimate the probability of tumor control or normal tissue complications based on the dose distribution.

In this thesis, the optimization problem is formulated as follows:

$$\min_{x} F(x) = \sum_{s \in \{PTV, OARs\}} \|A^s x - d\|_2^2 \tag{2}$$

In this expression, A^s represents the rows of the dose influence matrix corresponding to structure s, x is the vector of beamlet intensities, and d is the reference dose vector. The objective is to minimize the squared deviation between the calculated dose distribution and a reference dose, structure by structure.

Constraints to the segmentation optimization

In RT inverse optimization, several types of constraints must be incorporated to ensure that the resulting treatment plan is both clinically acceptable and physically deliverable. These constraints can be broadly classified into two categories: dosimetric constraints and machine constraints.

Dosimetric constraints refer to limits imposed on the radiation dose delivered to specific anatomical structures. These are designed to protect OARs from excessive radiation while ensuring that the PTV receives sufficient dose coverage. Such constraints are essential for balancing tumor control with toxicity prevention.

Machine constraints, by contrast, are associated with the physical capabilities and technical limitations of the LINAC used for treatment delivery. These constraints ensure that the treatment plan can be executed safely and accurately on the treatment machine. For example, during MLC segmentation optimization, constraints are required to prevent opposing MLC leaves from overlapping and to ensure leaf positions remain within the allowable field size. Additionally, the intensity of each MLC aperture (or segment) must be limited to values within the LINAC's operational range.

A representative formulation of a constrained segmentation optimization problem, adapted from [77], is given by:

$$\begin{aligned}
\min_{x} \quad & F(x) = \sum_{s \in \{PTV\}} \|A^s x - d\|_2^2 && \text{(3a)}\\
\text{subject to} \quad & maximum(A^s x) \leq d_s^{max}; s \in \text{Structure with Max. Hard Constraints} && \text{(3b)}\\
& mean(A^s x) \leq d_s^{mean}; s \in \text{Structure with Mean Hard Constraints} && \text{(3c)}\\
& x = \psi(\mu, l, r) && \text{(3d)}\\
& 0 \leq l \leq r \leq N && \text{(3e)}\\
& 0 \leq \mu \leq U^{\mu} && \text{(3f)}
\end{aligned}$$

In this formulation, constraints (3b) and (3c) enforce the hard limits on maximum and mean dose values for the relevant anatomical structures, ensuring that the clinical dose criteria are met. Constraint (3d) introduces a non-linear mapping function $\psi(\mu, l, r)$, which relates the beamlet intensities x to the

physical configuration of MLC leaves (defined by the left and right leaf positions l and r) and the corresponding aperture intensities μ. This relationship encapsulates the segmentation logic, effectively connecting fluence maps to physically deliverable apertures. Constraint (3e) ensures valid MLC geometry by preventing leaf overlap and enforcing position limits within the field size, where N is the number of columns in the fluence map. Finally, constraint (3f) restricts the aperture intensities to lie within the LINAC's operational limits, where U^{μ} defines the maximum permissible intensity.

The complexity and non-convexity of the segmentation optimization problem arise primarily from the non-linear nature of constraint (3d). The function ψ introduces a coupling between fluence intensity and aperture geometry, making the problem significantly more difficult to solve compared to standard convex dose optimization. As a result, specialized optimization strategies are required to generate clinically viable and deliverable treatment plans.

2.3 Native algorithm for automated segmentation

There are various algorithms available to address the segmentation problem in RT optimization (Section 2.2.3). One DAO approach is based on SCP, which was proposed by Dursun as a method for generating deliverable MLC segments from automatically computed Erasmus-iCycle plans [77].

Convex optimization problems are typically easier to solve than non-convex ones, as they usually yield a unique solution that minimizes or maximizes the objective function. In contrast, non-convex problems often have multiple local optima, and identifying the global optimum among them can be computationally demanding, especially for high-dimensional, complex problems encountered in RT planning.

SCP is an optimization technique specifically designed to address such non-convex problems [78]. It does so by solving a sequence of convex approximations of the original non-convex problem. At each iteration, the algorithm constructs a convex subproblem that is locally valid within a region surrounding the current solution, known as the trust-region. The optimal solution of this subproblem is then evaluated using the original objective function. If this solution represents an improvement, it is accepted as the new starting point for the next iteration. Otherwise, the algorithm either terminates or generates a new convex approximation to continue the optimization.

Convexification relies on exploiting structural properties of the original problem to build valid approximations. These approximations can be either local or global, depending on the size of the trust-region they represent. Local approximations focus on refining the solution in the immediate vicinity of the current point, potentially converging to a nearby local optimum (Figure 2.4, left). Global approximations, by contrast, span larger regions and help capture the broader shape of the objective landscape, thereby facilitating global convergence (Figure 2.4, right). A common strategy is to begin with a broader trust-region to allow for global exploration, and then gradually reduce the trust-region size to fine-tune the solution locally. Enlarging the trust-region when improvements are found promotes exploration, while shrinking it enhances approximation accuracy around promising solutions.

Figure 2.4 illustrates SCP applied to a simple one-dimensional non-convex function with multiple local optima, including $\overline{x}$ and the global optimum x^*. In the left figure, the algorithm begins at an initial point x_0, where a local convex approximation $\hat{f}$ (dashed line) is constructed. The solution x_1, obtained by minimizing this approximation, is better than x_0 in terms of the original function, and thus becomes

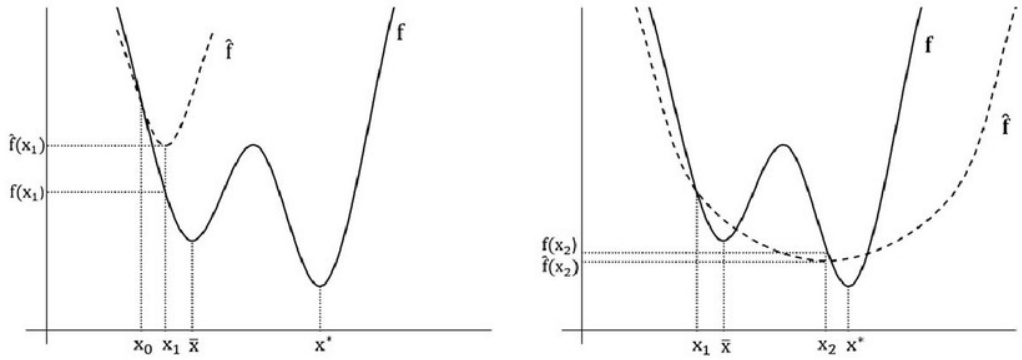

Figure 2.4: Schematic illustration of the concept behind sequential convex programming. (Left figure): a one-dimensional non-convex function f is approximated locally at x_0 by a convex function $\hat{f}$. The optimal solution of $\hat{f}$ is found (x_1) and used as the next solution. (Right figure): a non-convex function f is approximated globally at x_1 by $\hat{f}$ whose optimal solution (x_2) is used as the next solution.

the next iteration point. This process repeats until the algorithm converges to a local optimum $\overline{x}$. The right panel illustrates how a broader, global approximation of the original function allows the algorithm to escape local optima and approach the global solution x^*.

Overall, SCP offers a powerful framework for solving non-convex optimization problems by iteratively solving tractable convex subproblems and guiding the search toward globally optimal or near-optimal solutions. In this study, an SCP-based algorithm was addopted to evaluate the feasibility of generating deliverable VMAT segments that replicate the dose distributions produced by Erasmus-iCycle.

2.4 Research Scope and Approach

Erasmus-iCycle is capable of generating Pareto-optimal and clinically favorable RT treatment plans. However, to be deliverable by a LINAC, these plans must be reconstructed using a clinical TPS. The integration between Erasmus-iCycle and commercial TPS platforms is often limited, with restricted transparency into internal algorithms and workflows. To overcome these limitations, coupling Erasmus-iCycle with a SCP-based algorithm offers a promising alternative. This in-house developed SCP algorithm provides flexibility and control in generating deliverable plans while maintaining compatibility with LINAC specifications. Such an integration has the potential to enhance treatment planning efficiency and customization.

Chapter 3 of this thesis will focus on the integration of Erasmus-iCycle with Eclipse. This integration process—referred to as ”translation” seeks to establish a streamlined connection between Erasmus-iCycle's optimized plans and their reconstruction within Eclipse. The chapter will examine ten prostate cancer patient plans initially computed using Erasmus-iCycle and subsequently reconstructed in Eclipse. Through detailed dosimetric analysis and comparison, we aim to assess the feasibility, consistency, and clinical viability of this integration.

Chapter 4 will investigate a complementary integration strategy, combining Erasmus-iCycle with the SCP-based segmentation algorithm. This approach leverages Erasmus-iCycle's robust dose optimization with the segmentation flexibility offered by SCP. The same set of ten prostate patient plans will be reconstructed using the SCP-based algorithm, enabling a direct comparison with the Eclipse-based reconstructions. This comparative analysis will allow us to evaluate both approaches in terms of deliverability, dosimetric quality, and overall planning performance.

In summary, this thesis explores two integration pathways for translating Erasmus-iCycle plans into clinically deliverable VMAT segments: one through Eclipse and the other via an SCP-based algorithm. By analyzing and comparing these approaches, the study aims to provide valuable insights into their respective advantages and limitations. The outcomes are expected to contribute to improved treatment planning workflows, with the ultimate goal of enhancing plan quality and efficiency in clinical RT.

3 iCycle-Eclipse Translation

In section 2.2.2, a general description of the iCycle-Eclipse translation was provided. In this chapter, a detailed workflow of the translation process is presented, along with a comparative analysis of VMAT treatment plans generated by Eclipse and Erasmus-iCycle. The primary evaluation criteria include PTV coverage, dose homogeneity, and sparing of OARs

3.1 Methods

3.1.1 Overview of Erasmus-iCycle and Eclipse

Erasmus-iCycle creates Pareto-optimal treatment plans by using a set of predefined clinical objectives and constraints, collectively referred to as the wish-list. However, it lacks the capability to generate optimized MLC segments, and therefore cannot produce VMAT plans that are directly deliverable. In contrast, Eclipse is a commercial TPS that performs both MLC segmentation and beam modulation optimization to produce clinically deliverable VMAT plans.

To bridge this gap, the two systems are combined in a sequential workflow, with Erasmus-iCycle used for initial plan optimization and Eclipse for final delivery planning. This integration aims to determine whether Eclipse can convert Erasmus-iCycle's high-quality, non-deliverable plans into clinically usable VMAT treatments while preserving their dosimetric integrity.

3.1.2 Integration Workflow

To overcome this segmentation issue, dose information from the Erasmus-iCycle plan is extracted and converted into Line Objectives. Instead of using conventional discrete dose constraints (e.g., the mean dose or specific dose-volume parameters), multiple dose-volume points from the DVHs of each structure are sampled. These DVH-derived dose points form "continuous" Line Objectives, guiding Eclipse's optimizer toward a deliverable solution closely aligned with the Erasmus-iCycle reference plan. Figure 3.1 illustrates this process for one example patient.

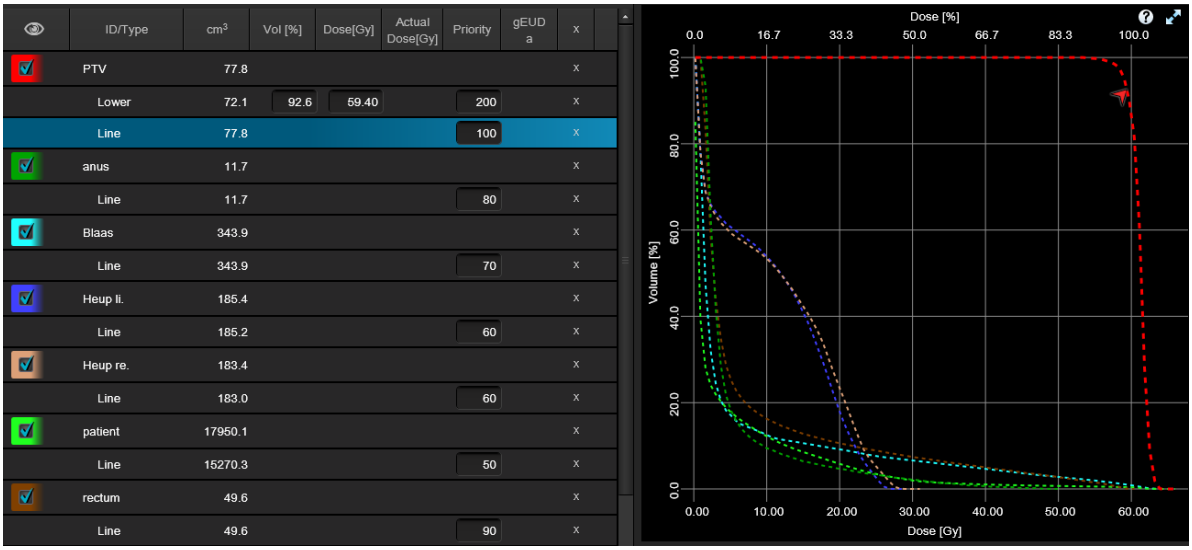

Figure 3.1: Example of Line Objectives imported into Eclipse for a prostate VMAT plan. The left panel shows the list of structures and corresponding dose-volume constraints derived from Erasmus-iCycle, expressed as Line Objectives. The right panel displays the associated DVH used during optimization, enabling Eclipse to approximate the original iCycle dose distribution by guiding the plan towards a continuous dosimetric profile.

Subsequently, these Line Objectives are automatically exported by a script that moved information from the DVHs in .csv format into an objective template in .xml format into a file and imported directly into Eclipse, substituting the traditional dose constraints commonly used during optimization [72]. Within Eclipse, the optimization workflow involves a consistent set of parameters applied uniformly across all patients, with patient-specific customization implicitly achieved through the individualized Line Objectives derived from Erasmus-iCycle. Following optimization, all plans were normalized to ensure that 99% of the PTV received the prescribed dose of 57 Gy.

This workflow facilitates the conversion of non-deliverable Erasmus-iCycle treatment plans into clinically deliverable VMAT plans, preserving dosimetric integrity. These Eclipse-generated plans serve as benchmarks for evaluating the feasibility and accuracy of the integration process, particularly regarding preservation of the original dose distribution characteristics.

3.1.3 Data and Testing

To evaluate this integration methodology, 10 prostate cancer patients who underwent VMAT treatment planning at Erasmus Medical Center were retrospectively selected. Prostate cancer, originating in the prostate gland located directly inferior to the bladder, is commonly treated with VMAT due to its capability for conformal dose delivery and effective sparing of adjacent OARs.

Each patient's original Erasmus-iCycle plan was processed through the previously described workflow, resulting in clinically deliverable VMAT plans in Eclipse. These final plans were then analyzed to assess how well they preserved the dosimetric characteristics of the original Erasmus-iCycle reference plans. The primary evaluation metric was a comparative analysis of DVHs between the iCycle-generated and Eclipse-optimized plans. As all plans were normalized to the prescription dose, direct comparison was possible.

3.2 Results

The dosimetric quality of VMAT treatment plans generated by Erasmus-iCycle and Eclipse was evaluated using DVH analysis. Table 3.1 summarizes key dosimetric parameters for PTV coverage (V95%, D98%), dose homogeneity (Dmean, D2%), and OAR sparing (Rectum: Dmean, V58Gy, V50%; Bladder and Anus: Dmean; Femoral Heads: D0.001cc).

In terms of PTV coverage, Erasmus-iCycle and Eclipse provided similar results, with only negligible differences observed in V95% and D98%. Both systems achieved adequate target volume coverage, with differences typically below clinical significance. Regarding dose homogeneity, Eclipse demonstrated better performance compared to Erasmus-iCycle, as evidenced by consistently lower D2% values. This indicates that Eclipse plans result in fewer hotspots within the target volume, reflecting a more uniform dose distribution.

For OAR sparing, Erasmus-iCycle generally achieved lower mean doses and smaller high-dose volumes for the rectum, specifically for V58Gy and V50Gy. Conversely, Eclipse showed marginally improved sparing of the femoral heads, demonstrated by significant lower mean doses in most patients. Whole-body dose exposure, represented by low- and intermediate-dose metrics (V30Gy, V15Gy, and V3Gy), showed similar distributions between both planning systems. Minor patient-specific variations were observed, but overall, neither method significantly impacted whole-body dose deposition relative to the other.

Table 3.1: Comparison of dose metrics between iCycle and Eclipse treatment plans. For each patient, the values for iCycle and Eclipse are presented, along with the difference (iCycle – Eclipse) to highlight variations in target coverage, dose uniformity, and OAR sparing. In the last table, green indicates dosimetric improvement or favorable outcomes (e.g., improved target coverage or reduced OAR dose), while red indicates dosimetric deterioration or less favorable outcomes (e.g., increased hotspots or elevated OAR doses) and yellow indicates that there isn't significant clinical difference

Treatment		iCycle										
Patient ID		1	2	3	4	5	6	7	8	9	10	Avg (Std)
PTV	V95% (%)	99.00	99.00	99.00	99.00	99.00	99.00	99.00	99.00	99.00	99.00	99.00 (0.00)
	D98% (Gy)	57.83	57.80	57.90	57.82	57.89	58.16	57.84	57.78	57.77	57.95	57.87 (0.11)
	D2% (%)	105.31	104.16	105.08	105.00	105.17	105.30	104.62	104.66	105.20	105.42	104.99 (0.37)
	Dmean (Gy)	61.11	60.77	61.11	61.13	61.18	61.18	60.89	61.10	61.09	61.25	61.08 (0.14)
Rectum	Dmean (Gy)	14.53	14.87	6.92	13.73	13.54	7.39	19.31	11.27	10.47	7.74	11.98 (3.76)
	V58Gy (%)	3.88	4.88	1.29	4.15	6.43	0.60	8.30	2.99	3.44	1.18	3.71 (2.29)
	V50Gy (%)	9.12	11.37	3.55	9.27	11.26	2.76	16.79	7.39	6.96	3.70	8.22 (4.11)
Anus	Dmean (Gy)	12.18	33.36	12.52	7.52	24.20	5.84	8.91	37.68	23.83	21.59	18.76 (10.52)
Bladder	Dmean (Gy)	13.58	11.00	10.92	8.59	4.96	4.84	15.56	12.46	6.13	16.25	10.43 (3.97)
L. Fem. H.	D0.001cc (Gy)	28.38	26.96	28.90	38.10	29.18	27.11	27.48	28.72	30.23	29.85	29.49 (3.05)
R. Fem. H.	D0.001cc (Gy)	25.80	27.87	35.97	34.10	29.62	28.69	23.14	30.35	31.17	32.99	29.97 (3.66)
Patient	Dmean (Gy)	5.05	5.07	3.72	4.67	4.32	3.82	3.98	5.55	3.83	3.61	4.36 (0.65)
	V30Gy (%)	3.28	2.80	2.22	3.42	2.64	1.96	2.14	3.96	2.69	2.22	2.73 (0.61)
	V15Gy (%)	12.44	11.90	8.57	10.88	9.81	8.55	8.98	14.24	8.99	8.59	10.30 (1.89)
	V3Gy (%)	25.54	27.40	20.45	23.86	23.99	21.91	22.88	29.09	19.12	19.08	23.33 (3.19)

Treatment		Eclipse										
Patient ID		1	2	3	4	5	6	7	8	9	10	Avg (Std)
PTV	V95% (%)	99.00	98.99	98.99	99.00	98.99	99.00	98.99	99.00	98.99	99.00	99.00 (0.00)
	D98% (Gy)	57.79	57.69	58.01	57.92	57.57	57.69	57.90	57.93	57.75	58.03	57.83 (0.14)
	D2% (%)	102.75	102.39	102.96	103.02	101.63	101.76	103.88	103.54	103.73	103.24	102.89 (0.73)
	Dmean (Gy)	59.87	59.78	60.08	60.04	59.31	59.57	60.48	60.43	60.08	60.25	59.99 (0.35)
Rectum	Dmean (Gy)	14.62	15.12	7.18	13.86	13.80	7.96	19.10	11.83	10.48	8.02	12.20 (3.62)
	V58Gy (%)	4.86	6.73	1.81	4.95	7.12	1.08	9.91	3.67	4.26	1.73	4.61 (2.62)
	V50Gy (%)	9.45	11.77	3.65	9.30	11.16	3.24	16.13	7.06	7.05	3.67	8.25 (3.94)
Anus	Dmean (Gy)	11.75	32.46	12.43	7.98	23.67	6.41	9.12	36.37	23.50	20.83	18.45 (9.99)
Bladder	Dmean (Gy)	14.25	10.89	11.44	9.61	4.69	5.01	16.60	12.71	5.95	16.25	10.74 (4.18)
L. Fem. H.	D0.001cc (Gy)	28.21	32.95	27.41	31.39	25.95	22.72	23.72	26.11	28.63	22.21	26.93 (3.36)
R. Fem. H.	D0.001cc (Gy)	25.41	25.17	23.53	28.64	25.29	22.19	19.32	29.79	28.35	23.09	25.08 (3.06)
Patient	Dmean (Gy)	4.85	4.91	3.59	4.59	4.27	3.75	3.74	5.80	3.67	3.28	4.25 (0.74)
	V30Gy (%)	2.83	2.42	1.52	2.33	2.05	1.56	1.41	3.14	1.89	1.51	2.07 (0.57)
	V15Gy (%)	11.21	10.77	6.99	10.96	9.07	6.56	6.56	15.09	9.02	6.37	9.26 (2.67)
	V3Gy (%)	25.43	27.86	21.32	24.63	24.47	23.11	23.32	30.55	18.88	19.00	23.86 (3.46)

Treatment		Difference (iCycle - Eclipse)										
Patient ID		1	2	3	4	5	6	7	8	9	10	Avg (Std)
PTV	V95% (%)	0.00	0.01	0.01	0.00	0.01	0.00	0.01	0.00	0.01	0.00	0.01 (0.00)
	D98% (Gy)	0.04	0.11	-0.11	-0.10	0.32	0.46	-0.06	-0.15	0.01	-0.08	0.04 (0.19)
	D2% (%)	2.56	1.77	2.12	1.99	3.54	3.53	0.74	1.11	1.47	2.18	2.10 (0.88)
	Dmean (Gy)	1.24	0.99	1.03	1.09	1.88	1.60	0.41	0.67	1.02	1.00	1.09 (0.40)
Rectum	Dmean (Gy)	-0.09	-0.25	-0.26	-0.14	-0.26	-0.57	0.21	-0.56	0.00	-0.28	-0.22 (0.22)
	V58Gy (%)	-0.98	-1.85	-0.52	-0.80	-0.69	-0.48	-1.62	-0.68	-0.83	-0.55	-0.90 (0.44)
	V50Gy (%)	-0.34	-0.40	-0.11	-0.03	0.10	-0.48	0.66	0.33	-0.09	0.02	-0.03 (0.33)
Anus	Dmean (Gy)	0.43	0.90	0.09	-0.46	0.53	-0.57	-0.20	1.31	0.33	0.76	0.31 (0.57)
Bladder	Dmean (Gy)	-0.67	0.11	-0.52	-1.02	0.27	-0.17	-1.04	-0.25	0.19	0.00	-0.31 (0.46)
L. Fem. H.	D0.001cc (Gy)	0.17	-5.99	1.49	6.71	3.23	4.39	3.76	2.61	1.60	7.64	2.56 (3.59)
R. Fem. H.	D0.001cc (Gy)	0.39	2.70	12.44	5.46	4.33	6.50	3.82	0.56	2.82	9.90	4.89 (3.67)
Patient	Dmean (Gy)	0.20	0.16	0.13	0.08	0.05	0.07	0.24	-0.25	0.16	0.32	0.12 (0.15)
	V30Gy (%)	0.45	0.38	0.70	1.09	0.60	0.40	0.73	0.82	0.80	0.71	0.67 (0.21)
	V15Gy (%)	1.23	1.13	1.58	-0.08	0.74	2.00	2.42	-0.85	-0.03	2.22	1.04 (1.03)
	V3Gy (%)	0.11	-0.46	-0.86	-0.77	-0.48	-1.20	-0.44	-1.46	0.24	0.08	-0.52 (0.54)

These results indicate that the integrated workflow using Erasmus-iCycle as a pre-optimizer and Eclipse as a final optimizer successfully produces clinically deliverable VMAT plans with minimal deviation from the original dosimetric intentions defined by Erasmus-iCycle.

3.2.1 Example Patient

Patient 6 was selected as the example case for this comparison because its anatomical and clinical characteristics were representative of the overall cohort, ensuring that the analysis reflected a typical case rather than an outlier.

Figure 3.2a presents a DVH comparison for Patient 6. The DVHs for the PTV and critical OARs (rectum, bladder, femoral heads, and anus) are overlaid for both Erasmus-iCycle (solid lines) and Eclipse (dashed lines) plans. Both systems provided comparable PTV coverage, with Eclipse demonstrating slightly improved dose homogeneity.

For bladder sparing, Erasmus-iCycle resulted in lower doses, especially in low-dose regions. Similarly, the rectal dose-volume curves indicated that Erasmus-iCycle achieved a more pronounced dose gradient, effectively reducing high-dose volumes. Eclipse, however, provided superior sparing of the femoral heads, evident from lower mean doses. Differences in anus dose sparing were minimal, slightly favoring Erasmus-iCycle.

Additionally, Figure 3.2b displays the axial 3D dose distribution for the same patient at the isocenter plane. The Erasmus-iCycle plan shows distinct modulation, characterized by clearly visible low-dose streaks. Conversely, the Eclipse plan presents smoother dose transitions, indicative of a more uniformly modulated delivery.

The DVHs and dose distributions for the rest of the patients are in the Appendix A.

These findings indicate that the integrated workflow using Erasmus-iCycle as a pre-optimizer and Eclipse as a final optimizer successfully produces clinically deliverable VMAT plans with minimal deviation from the original dosimetric intentions defined by Erasmus-iCycle.

3.3 Discussion

3.3.1 PTV Coverage, Homogeneity and Conformity

Clinically viable VMAT treatment plans must ensure adequate coverage of the PTV, typically assessed using dose-volume parameters such as D98%, D95%, and D50%. Across the patient cohort, Eclipse-generated plans maintained PTV coverage comparable to Erasmus-iCycle benchmarks, consistently staying within clinically acceptable thresholds.

In terms of dose homogeneity, Eclipse plans demonstrated improved performance compared to Erasmus-iCycle plans, as evidenced by consistently lower D2% values. This indicates that Eclipse-generated VMAT plans result in fewer hotspots within the PTV, reflecting a more uniform dose distribution. The improved homogeneity in Eclipse plans can be attributed to the optimization techniques inherent to VMAT, which effectively manage dose modulation while maintaining mechanical feasibility.

These findings suggest that the continuous arc delivery characteristic of VMAT helps achieve a more balanced dose distribution within the target volume. Consequently, Eclipse plans offer better control over

Figure 3.2: Comparison of Dose Distribution and DVH Between Erasmus-iCycle and Eclipse Plans: Patient 6, illustrating the differences between the iCycle (pre-optimized) and Eclipse (final optimized) VMAT plans. The bottom subfigure shows the transverse dose distributions, while the top subfigure presents the DVH analysis of the PTV and OARs.

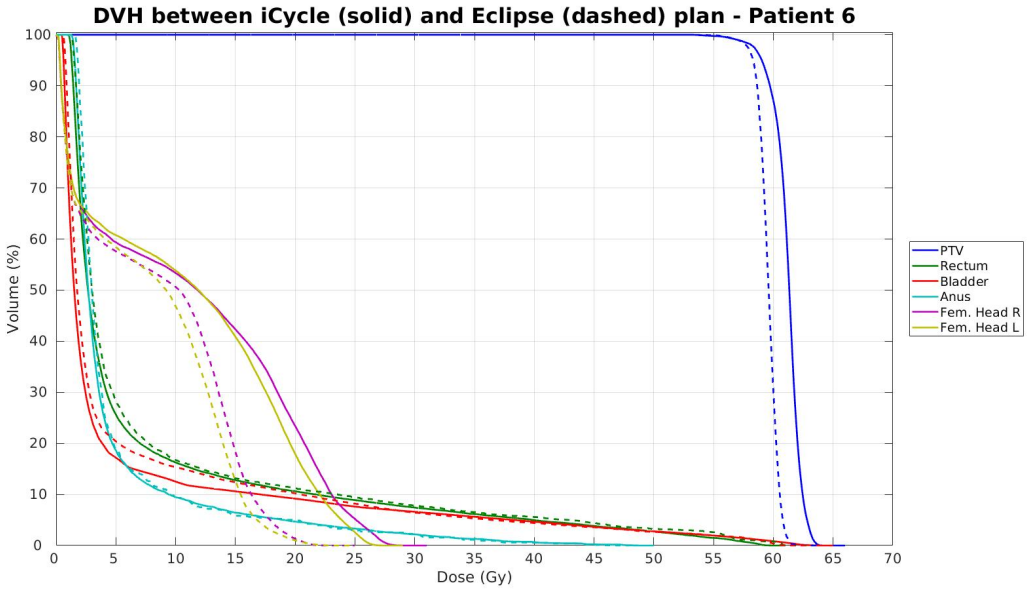

(a) Dose-Volume Histogram : Patient 6. The iCycle plan (solid lines) provides slightly better sparing of the bladder and rectum while maintaining comparable target coverage to the Eclipse plan (dashed lines). However, it results in higher dose exposure to the femoral heads,

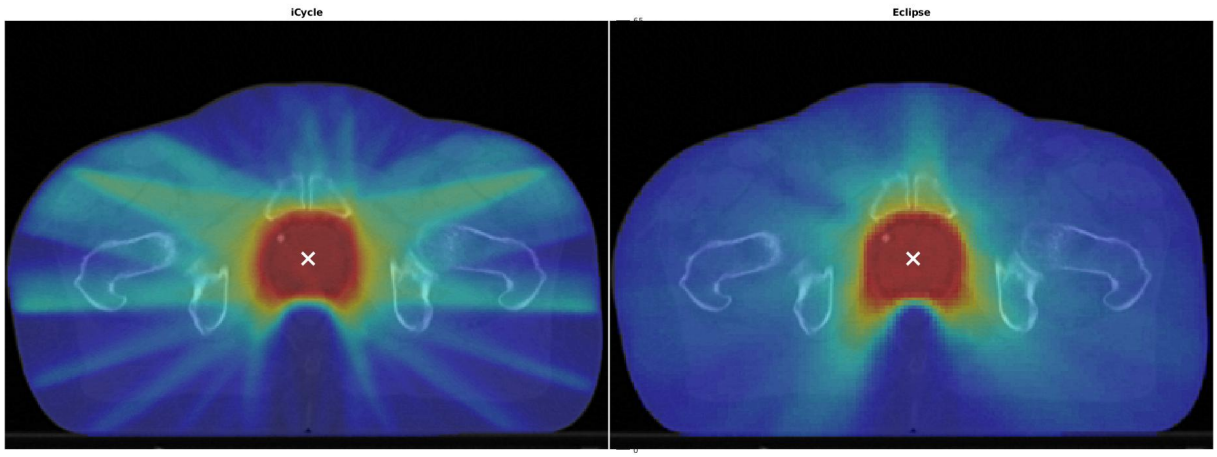

(b) Dose distribution for iCycle (left) and Eclipse (right) plans. The iCycle plan exhibits a more modulated dose pattern, whereas Eclipse results in a smoother dose fall-off. The PTV coverage is comparable, but there are visible differences in dose spillage and modulation.

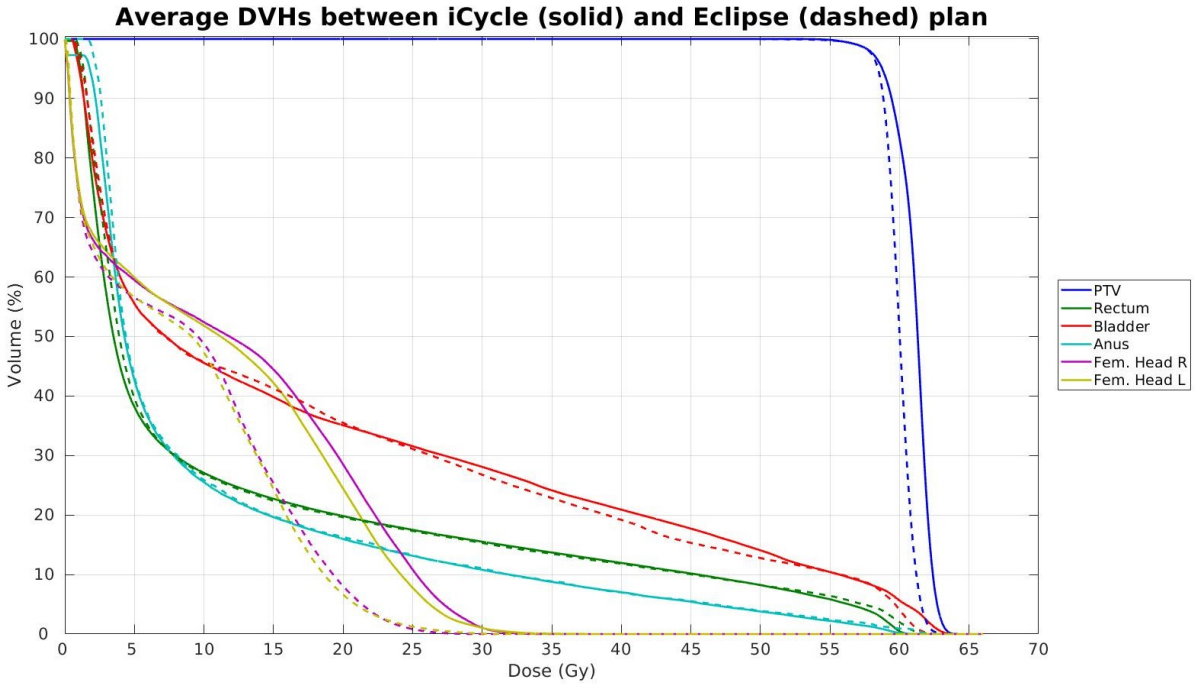

Figure 3.3: Patient-averaged Dose-Volume Histogram comparing Erasmus-iCycle (solid lines) and Eclipse (dashed lines) treatment plans. The plot illustrates systematic differences in dose distribution across the PTV and OARs, including the rectum, bladder, anus, and femoral heads. Notably, the Eclipse plans exhibit a slight increase in high-dose exposure to the rectum and the femoral heads show a significant reduction in mean dose.

dose uniformity compared to Erasmus-iCycle.

3.3.2 OAR Sparing and Dose Constraints

Preservation of OAR sparing during the translation process is critical for clinical acceptability. Comparative analysis of mean dose (Dmean) and specific dose-volume metrics (VXGy) for OARs, such as bladder, rectum, and femoral heads, indicates that Eclipse largely preserved OAR sparing objectives defined by Erasmus-iCycle but with some variations.

Figure 3.3 illustrates patient-averaged DVH comparisons for both Erasmus-iCycle (solid lines) and Eclipse (dashed lines). Notably, the rectum DVH revealed increased exposure in high-dose regions within Eclipse plans, suggesting that the continuous, rotational delivery of VMAT reduces the steepness of dose fall-off achieved by Erasmus-iCycle.

Conversely, femoral heads displayed improved sparing in Eclipse plans, indicated by lower mean doses compared to Erasmus-iCycle plans. Additionally, Eclipse plans exhibited a modest increase in low-dose spread across multiple OARs, which aligns with typical characteristics of VMAT delivery.

Overall, the Eclipse optimization process successfully translates Erasmus-iCycle's primary plans into clinically deliverable plans, despite introducing slight increases in low-dose exposure. These minor variations should be considered in the context of normal tissue exposure implications.

3.3.3 Limitations of Erasmus-iCycle Plans for VMAT Delivery

One important consideration is the difference observed in PTV dose distribution between the Erasmus-iCycle and Eclipse-generated plans. The results indicate that the source plans from Erasmus-iCycle may not be optimally suited for direct conversion into deliverable VMAT plans. Specifically, the observed variations in PTV dose homogeneity suggest that the initial wish-list configuration in iCycle requires further refinement to better align with the practical constraints of VMAT delivery.

Future work should focus on refining the wish-list criteria within Erasmus-iCycle to better accommodate the mechanical and modulation characteristics inherent to VMAT. By incorporating more realistic constraints and optimizing for delivery efficiency, it may be possible to generate iCycle plans that translate more seamlessly into clinically acceptable VMAT treatments.

3.4 Conclusion

This study assessed the feasibility of converting Erasmus-iCycle-optimized fluence maps into deliverable VMAT treatment plans using Eclipse while preserving dosimetric quality. Results indicate that Eclipse effectively retains critical dosimetric characteristics of the original iCycle plans, with some inherent trade-offs related to VMAT delivery constraints.

Eclipse plans maintained clinically acceptable PTV coverage, although minor reductions in D98% were noted, likely due to modulation smoothing in VMAT. Notably, Eclipse demonstrated better dose homogeneity, as evidenced by consistently lower D2% values, indicating fewer hotspots and a more uniform dose distribution within the target volume.

OAR sparing was generally well-preserved, with Eclipse showing slightly increased high-dose exposure for the rectum but improved sparing of the femoral heads. A modest increase in low-dose exposure was also observed, which is characteristic of VMAT delivery.

However, the findings also indicate that the source plans from Erasmus-iCycle may not be optimally suited for direct VMAT conversion, particularly in terms of PTV dose distribution. This suggests that more advanced wish-list tuning is needed to generate iCycle plans that are more compatible with the mechanical constraints of VMAT delivery.

Overall, Eclipse-generated VMAT plans from iCycle fluence maps remain clinically acceptable. Future work should focus on refining the iCycle wish-list to better accommodate VMAT-specific requirements, thereby enhancing the fidelity of the conversion process.

4 SCP-based Algorithm

In section 2.2.3, an overview of the general VMAT segmentation problem was provided. In this chapter, we will now focus on exploring the specifics of the problem and a possible way to find solutions. Our approach used SCP to solve the continuous optimization problem, discretized across several control points (gantry angles). This study focuses on implementing and evaluating an SCP-based optimization algorithm to efficiently and accurately optimize VMAT beam segments, aiming to enhance treatment quality, computational performance, and clinical applicability.

4.1 Methods

4.1.1 VMAT segmentation problem

One of the key differences between IMRT and VMAT is the continuous delivery of radiation in VMAT, typically performed in an arc around the patient. This continuous arc delivery significantly increases the complexity of the segmentation optimization problem compared to IMRT, as the number of beam angles to consider approaches continuity. Direct optimization of a continuous arc is computationally infeasible; therefore, the arc is discretized into a finite number of control points. The optimization then seeks the optimal aperture shapes and corresponding radiation intensities at these discrete angles. Key dosimetric objectives include adequate coverage of the PTV, sparing of OARs, and making sure that specific dose constraints are met. The exponential increase in variables associated with this discretization necessitates efficient optimization strategies, such as SCP.

The SCP algorithm was chosen because it offers efficient convergence by iteratively approximating non-convex problems with convex subproblems, thereby substantially reducing computational complexity compared to direct non-linear optimization approaches.

4.1.2 The SCP-based VMAT algorithm

In this section, a detailed description of a single iteration of the SCP-based VMAT optimization algorithm will be provided, illustrated using a single beam segment for simplicity.

Initial Solution and Trust-Region Definition

Each iteration begins by defining an initial segment shape corresponding to the Beam Eye View (BEV) of the PTV, representing the maximum allowable segment size intersecting the target region (Figure 4.1 left). This initial segment shape is characterized by an aperture intensity of $\mu = 300MU$. MLC leaves are then allowed to move inward from their initial positions, constrained by a trust-region that limits the maximum leaf displacement between consecutive iterations. The trust-region size dynamically adapts according to optimization progress, balancing exploration and precision in the solution space.

Categorization of Beamlets

For computational efficiency, beamlets within each segment are categorized into four distinct groups, as depicted in Figure 4.2a:

1. **External beamlets (Out-of-PTV)**: Always closed.
2. **Closed beamlets**: Currently closed and will remain closed.

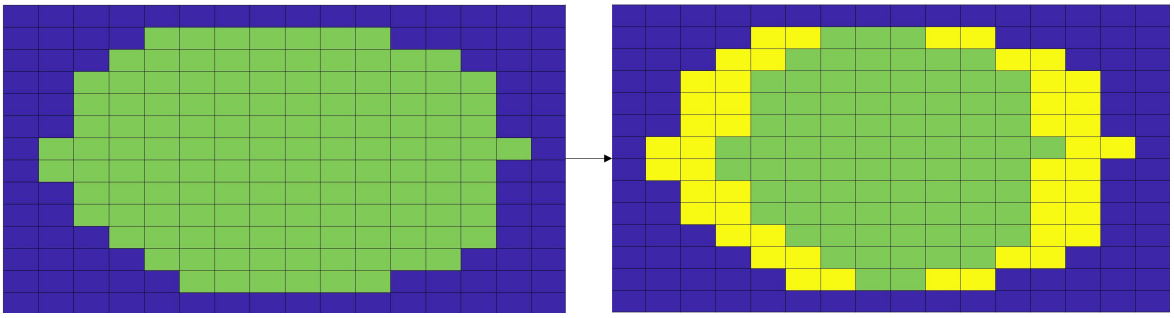

Figure 4.1: Illustration of Beam Eye View (BEV) segment shapes for the SCP-based VMAT algorithm. (*Left figure*): The blue and the green areas represent the external and internal beamlets of the BEV segment, respectively. (*Right figure*): the external and internal beamlets are represented by the blue and green areas, respectively, at the next iteration. The yellow areas indicate beamlets that may be fully or partially open or fully closed, depending on the leaf motion. To simplify the optimization problem, all open beamlets (green area) are merged into a single beamlet known as the interior beamlet. Since the external beamleats (dark blue area) are going to stay closed throughout the optimization they are not considered for optimization purposes.

3. **Interior beamlets (Open)**: Currently open and will remain open.
4. **Boundary beamlets (Unknown)**: Status (open/closed) determined by leaf optimization.

This categorization allows significant dimensionality reduction by merging adjacent beamlets sharing identical statuses, facilitating efficient SCP optimization.

External, closed, and interior beamlets (categories 1, 2, and 3) have fixed intensities: zero for external and closed beamlets, and a fixed intensity μ for interior beamlets. Thus, these beamlets can each be merged into single closed or open beamlet groups. Conversely, the intensity of boundary beamlets varies between 0 and μ, depending on leaf displacement. These boundary beamlets represent the transition zone between open and closed regions.

Convex Approximation and Optimization Formulation

With beamlets grouped, the optimization problem is approximated by a convex formulation:

$$\min_{\hat{x}} \quad F(\hat{x}) = \sum_{s\in\{PTV\}} \|\hat{A}^s\hat{x} - d\|_2^2 \tag{4a}$$

$$\text{Subject to:} \quad maximum(\hat{A}^s\hat{x}) \leq d_s^{max} : s \in \text{Structure with Max. Hard Constraints} \tag{4b}$$

$$mean(\hat{A}^s\hat{x}) \leq d_s^{mean} : s \in \text{Structure with Mean Hard Constraints} \tag{4c}$$

$$0 \leq \hat{x}_{b,k} \leq \hat{x}_b : b = 1, ..., N; k = 1, ..., K \text{ (boundary beamlets)} \tag{4d}$$

$$0 \leq \hat{x}_b \leq U^{\mu} : b = 1, ..., N \text{ (interior beamlets)}, \tag{4e}$$

where $\hat{x}$ and $\hat{A}$ are the adjusted intensity vector and adjusted dose influence matrix, respectively, $\hat{x}_{b,k}$ is the k^{th} boundary beamlet at beam b and $\hat{x}_b$ is the intensity of the interior beamlet, also at beam b. The optimization objective is to achieve a prescribed dose to the PTV while satisfying various dose constraints for the OARs.

However, if a benchmark plan has been computed previously using Erasmus-iCycle for a specific patient, the objective function can incorporate the vector of doses obtained from Erasmus-iCycle. This modification eliminates the necessity for explicit OAR dose constraints, simplifying the optimization formulation to:

$$\min_{\hat{x}} \quad F(\hat{x}) = \sum_{s\in\{PTV,OAR's\}} \|\hat{A}^s\hat{x} - d\|_2^2 \tag{5a}$$

$$\text{Subject to:} \quad 0 \leq \hat{x}_{b,k} \leq \hat{x}_b : b = 1, ..., N; k = 1, ..., K \text{ (boundary beamlets)} \tag{5b}$$

$$0 \leq \hat{x}_b \leq U^\mu : b = 1, ..., N \text{ (interior beamlets)}, \tag{5c}$$

The motivation behind this formulation is to reproduce the dose distribution generated by Erasmus-iCycle, which serves as a high-quality reference. In this context, the dose values used as input are similar to a voxel dose prescription, guiding the optimizer to replicate the desired distribution as closely as possible.

Optimization Solution and Reconstruction

After solving the convex approximated subproblem, the resulting solution is mapped back to the original non-convex VMAT problem. Boundary beamlets are assigned open or closed statuses based on their optimized intensities. A boundary beamlet with an intensity value equal to zero ($\hat{x}_{b,k} = 0$) indicates that all associated beamlets should be closed, whereas an intensity value equal to the maximum allowable beam intensity ($\hat{x}_{b,k} = \mu_b$) implies that all corresponding beamlets should be fully open.

For intermediate intensity values, beamlet solution is computed as a fraction of the maximum intensity, specifically ($\frac{\hat{x}_{b,k}}{\mu_b} * 100\%$ of the beamlets). Due to the discrete nature of beamlets, fractional solutions must be approximated by rounding to the nearest integer number of beamlets.

Example of solution reconstruction

In Figure 4.2, it is assumed that each leaf can move a maximum of one beamlet forward or backward in this example iteration. Examining the first and second rows, both the left and right leaves initially block exactly one beamlet each. By identifying and merging adjacent boundary beamlets, four boundary beamlets and one interior beamlet are defined for optimization purposes.

To illustrate, consider the first and fourth boundary beamlets. The first boundary beamlet includes the first two beamlets in the first row. Given its optimized intensity value of $\hat{x}_{n,1} = 0$, both beamlets should remain closed, prompting the leaf to move one beamlet forward. Conversely, the fourth boundary beamlet consists of the last two beamlets in the second row, which has an optimized intensity value of $\hat{x}_4 = \frac{1}{3}\mu$. This indicates that approximately 33.33% of the neighboring beamlets close to the interior beamlet should be open. However, due to the discrete nature of the beamlets, fractional solutions are not achievable; therefore, this value is rounded to the nearest integer beamlet, resulting in the closure of one beamlet and the opening of the remaining beamlet.

Comparison with previous solutions

Following the reconstruction of the convex approximation solution, the aperture intensities (μ) are optimized while keeping leaf positions fixed. This intensity re-optimization is effectively a straightforward convex fluence map optimization step applied within the original non-convex framework. After intensity optimization, the solution is evaluated against the original non-convex objective function $F(\hat{x})$. If the new solution demonstrates an improvement compared to the previous iteration (lower $F(\hat{x})$ values), it is

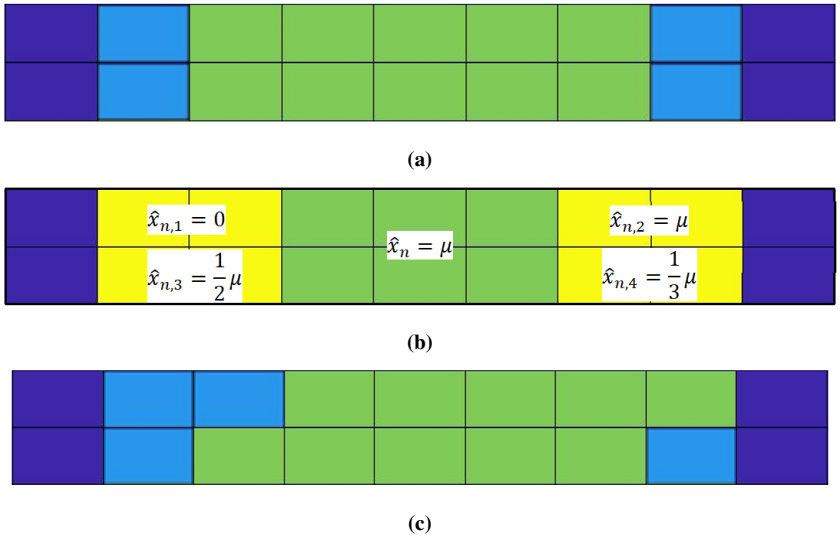

Figure 4.2: An example of a merged optimization solution reconstruction. (a): leaves position at beginning of iteration *i*; (b) optimal solution of the convex approximation problem at beam *b* ; (c) leaves positions at the end of iteration *i*. Note that there can not be half of a beamlet open (or closed). So, when $\hat{x}_{n,4} = \frac{1}{3}\mu$ it translates to $\frac{1}{3} * 2 \approx 1$ beamlet closed. Dark blue, light blue, yellow and green represent external, closed, boundary and open beamlets, respectively

accepted.

However, if the solution does not improve upon the previous one, the trust-region (step-size) must be adjusted to generate a new convex approximation. The SCP-based VMAT algorithm, summarized in Algorithm 1, begins with initial leaf positions set according to the BEV of the target. Initially, a relatively large trust-region is selected. At each subsequent iteration, a candidate solution is obtained by solving the convex approximation problem and followed by intensity re-optimization.

When the candidate solution reduces the objective function value, it is accepted, and the trust-region is expanded to allow global search. Conversely, if no improvement is observed, the candidate solution is rejected, and the trust-region is narrowed, aiming for a more precise convex approximation. This iterative procedure continues until the relative improvement over two consecutive iterations falls below a pre-defined convergence threshold of 2%, or the step-size reaches the minimal allowable limit of two beamlets.

Algorithm 1 Pseudocode for the algorithm. Adapted from [77]

```
Initialize the leaf positions (BEV of target) and step-size
while improvement > ϵ do
    Find the candidate solution x̂ by optimizing the convex approximation problem
    Reconstruct the solution x from x̂
    Optimize aperture intensity μ of x
    if x is better than x_n then
        Update the solution x_n = x
        Enlarge the trust region (step_size = step_size + 1)
    else
        Shrink the trust region (step_size = step_size / 2)
    end if
end while
```

4.1.3 Patient population

The patient population for this study consisted of the same ten patients previously described, ensuring consistency and enabling direct comparison between different optimization methods.

Dose influence matrices and objective dose vectors for each patient were calculated using Erasmus-iCycle. For all ten patients, a VMAT arc discretization of 72 control points was used, representing the number of discrete gantry positions used for segment calculation during arc rotation. To evaluate the impact of a higher arc resolution, an increased number of 180 control points was employed in an additional scenario for one selected patient (patient 6). This patient was chosen because its anatomical characteristics were representative of the cohort, ensuring that parameter testing was performed on a typical case rather than on an outlier.

The standard beamlet resolution for the entire patient cohort was set to $5\,mm \times 5\,mm$. However, to specifically investigate the effects of finer spatial resolution, a higher beamlet resolution of $5\,mm \times 2\,mm$ was applied to the same patient used for the increased control-point evaluation.

4.1.4 Implementation details

The SCP-based VMAT optimization algorithm was implemented in MATLAB (The MathWorks, Inc., Natick, MA, USA). Each iteration's convex subproblem was solved using MATLAB's built-in quadratic optimization solver, `quadprog`, which efficiently handles quadratic objective functions subject to linear constraints.

The algorithm's performance was evaluated under various optimization scenarios for the same test patient. The configurations evaluated included PTV and Rectum optimization, which simultaneously optimized target coverage while sparing the rectum, and a full clinical scenario optimization, which incorporated comprehensive optimization constraints for multiple structures. These structures included the PTV, several concentric shells around the PTV (with distances of 5 mm, 10 mm, 15 mm, 25 mm, and 50 mm), and critical OARs, including the Rectum, Bladder, Anus, and Femoral Heads.

4.1.5 Dosimetric Evaluation Metrics

To quantitatively evaluate the dosimetric performance of the SCP-based VMAT plans, comparisons were made against reference plans generated by the Erasmus-iCycle planning system. DVHs served as the primary tool for assessing dosimetric quality, as they effectively illustrate dose coverage of the PTV and sparing of OARs.

Key dosimetric metrics, as used in the previous chapter, were specifically analyzed and compared between SCP-based plans and Erasmus-iCycle reference plans. These metrics provided comprehensive insights into the clinical acceptability, dosimetric quality, and the potential advantages or limitations of the SCP-based algorithm in replicating Erasmus-iCycle reference plan quality.

4.2 Results

4.2.1 Parameter Tuning on Selected Patient

To identify a good set of parameters for the SCP-based VMAT optimization algorithm, one patient from the dataset was randomly selected for exploratory testing, patient 6 (the same used in the previous study). The primary objective was to explore how different configurations affect dosimetric quality and computational efficiency. The three main aspects evaluated were beam angle sampling, beamlet resolution, and optimization priority.

Beam Angle Sampling

The number of control points (beam angles) significantly impacts both the plan quality and computation time. Two configurations were tested: 72 and 180 control points.

As illustrated in Figure 4.3c, increasing the number of control points from 72 to 180 resulted in improved dose conformity and slightly better PTV coverage. However, this enhancement came at the cost of a notable increase in computation time. Despite the higher resolution, the differences in dosimetric metrics, such as D98% and D2% for the PTV, were minimal. Therefore, the trade-off between computational efficiency and marginal dosimetric gain led to selecting the 72 control points configuration as a better setup.

Beamlet Resolution

Beamlet resolution determines the spatial granularity of dose distribution within the treatment volume. Two resolutions were tested: $5\,mm \times 5\,mm$ and $2\,mm \times 5\,mm$.

As shown in Figures 4.3d and 4.3b, using the finer resolution improved dose homogeneity, particularly in regions where critical structures were close to the PTV. However, the computational time increased significantly rising from approximately 10 minutes to around 2 hours due to the larger number of beamlets to optimize. The difference between the two configurations was noticeable but not clinically significant, suggesting that the standard resolution ($5\,mm \times 5\,mm$) offered a reasonable balance between computational efficiency and dosimetric quality.

Optimization Priorities: PTV and Rectum vs. All Structures

Optimization priorities were evaluated by comparing two setups: PTV and Rectum Optimization and All Structures Optimization (PTV, concentric dose shells, rectum, bladder, anus, and femoral heads).

The PTV and Rectum optimization configuration yielded faster convergence and slightly better PTV coverage. However, when including all relevant structures, the plan quality improved in terms of OAR sparing, especially for the femoral heads, as shown in Figure 4.3a. Despite a slight increase in computational time, the comprehensive optimization proved beneficial in maintaining clinically acceptable doses to all structures. Consequently, the configuration optimizing all structures was chosen for further evaluation.

Final Parameter Choice

Based on these tests, the chosen parameter set for the remaining patients was:

1. Beam Angle Sampling: 72 control points
2. Beamlet Resolution: 5 mm × 5 mm
3. Optimization Priorities: All structures

This configuration provided a balance between dosimetric quality and computational efficiency. Figure 4.3d and 4.4 shows the DVH and 3D dose distribution, respectively, for the selected patient optimized with the chosen parameters.

Figure 4.3: DVHs comparison between Erasmus-iCycle (solid) and SCP-based algorithm (dashed) for Patient 6, illustrating the impact of parameter tuning.

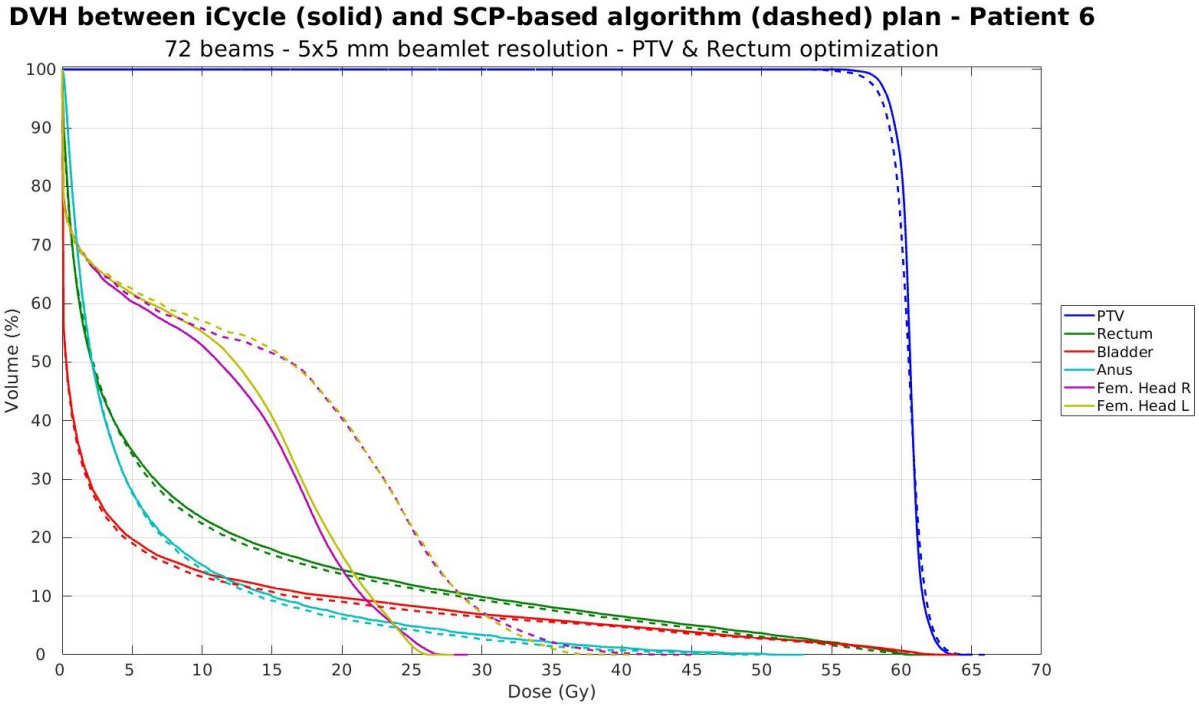

(a) DVH comparison between Erasmus-iCycle (solid) and SCP-based algorithm (dashed) for Patient 6. The plan was generated using 72 control points and a beamlet resolution of $5\,mm \times 5\,mm$, focusing on PTV and Rectum optimization. The plot highlights the trade-offs between prioritizing critical structures and maintaining adequate PTV coverage

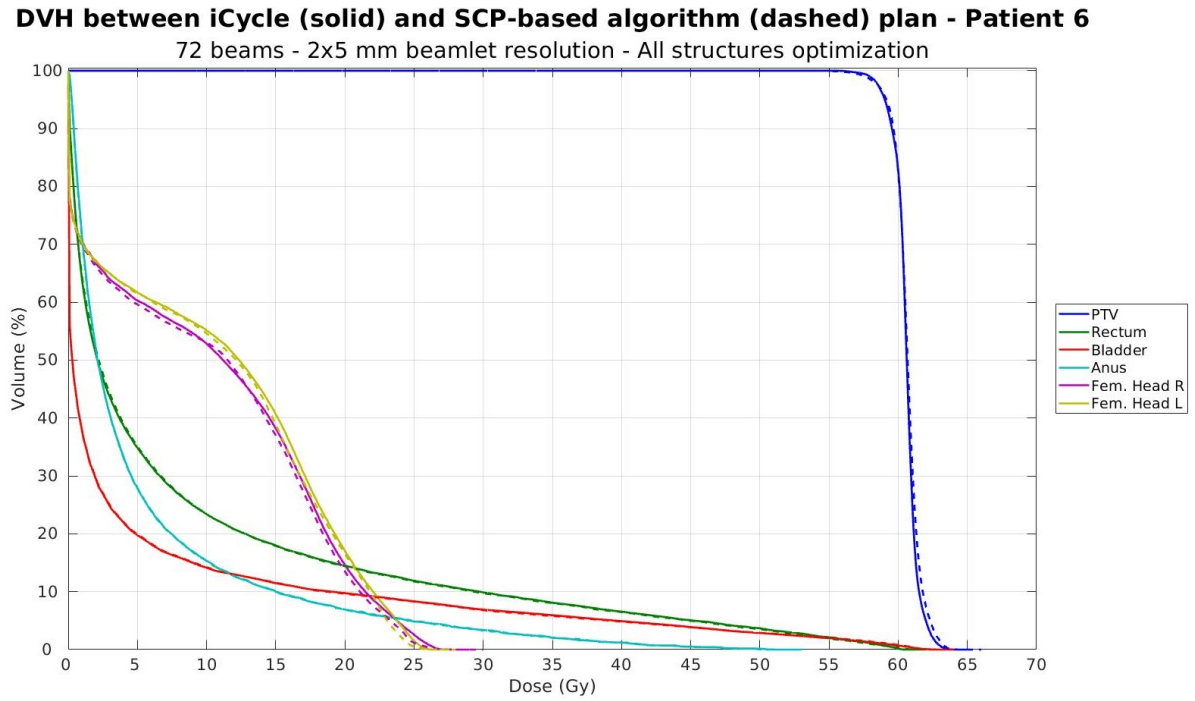

(b) DVH comparison between Erasmus-iCycle (solid) and SCP-based algorithm (dashed) for Patient 6. The plan was generated using 72 control points and a beamlet resolution of $2\,mm \times 5\,mm$, optimizing all relevant structures. The plot demonstrates the impact of intermediate resolution and moderate beam sampling on PTV coverage and OAR sparing.

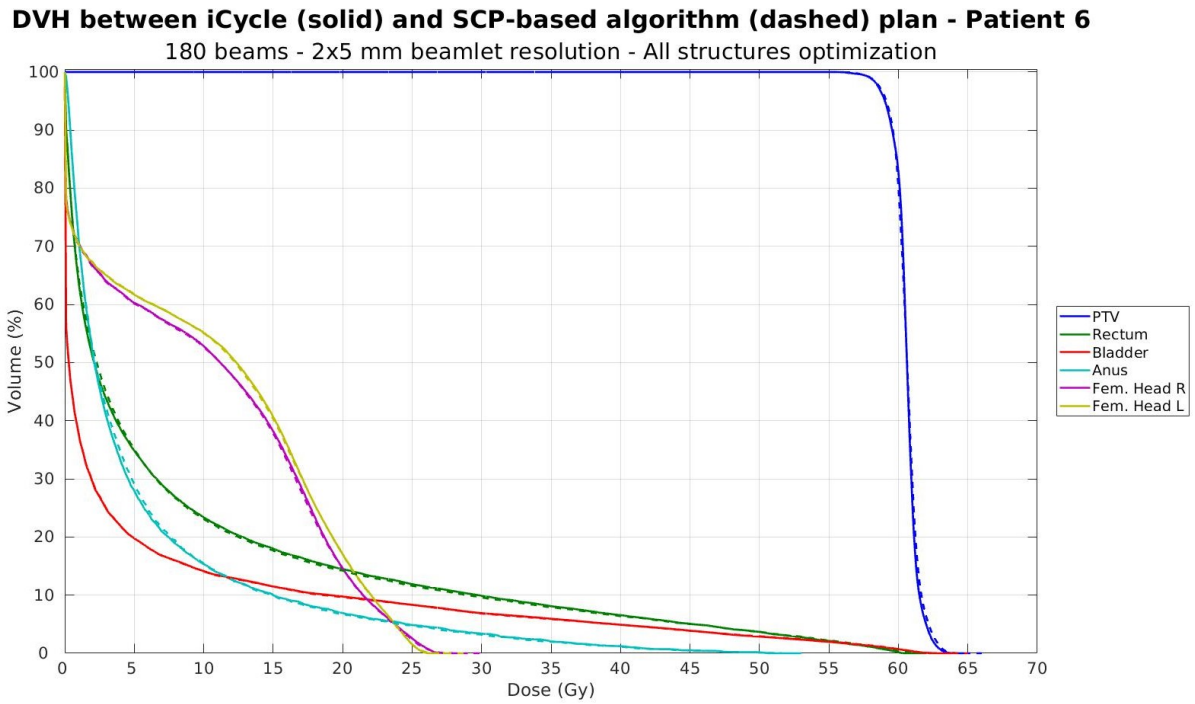

(c) DVH comparison between Erasmus-iCycle (solid) and SCP-based algorithm (dashed) for Patient 6. The plan was generated using 180 control points and a beamlet resolution of $2\,mm \times 5\,mm$, optimizing all relevant structures. The plot shows the effect of increased angular resolution on dose conformity and the potential for improved OAR sparing

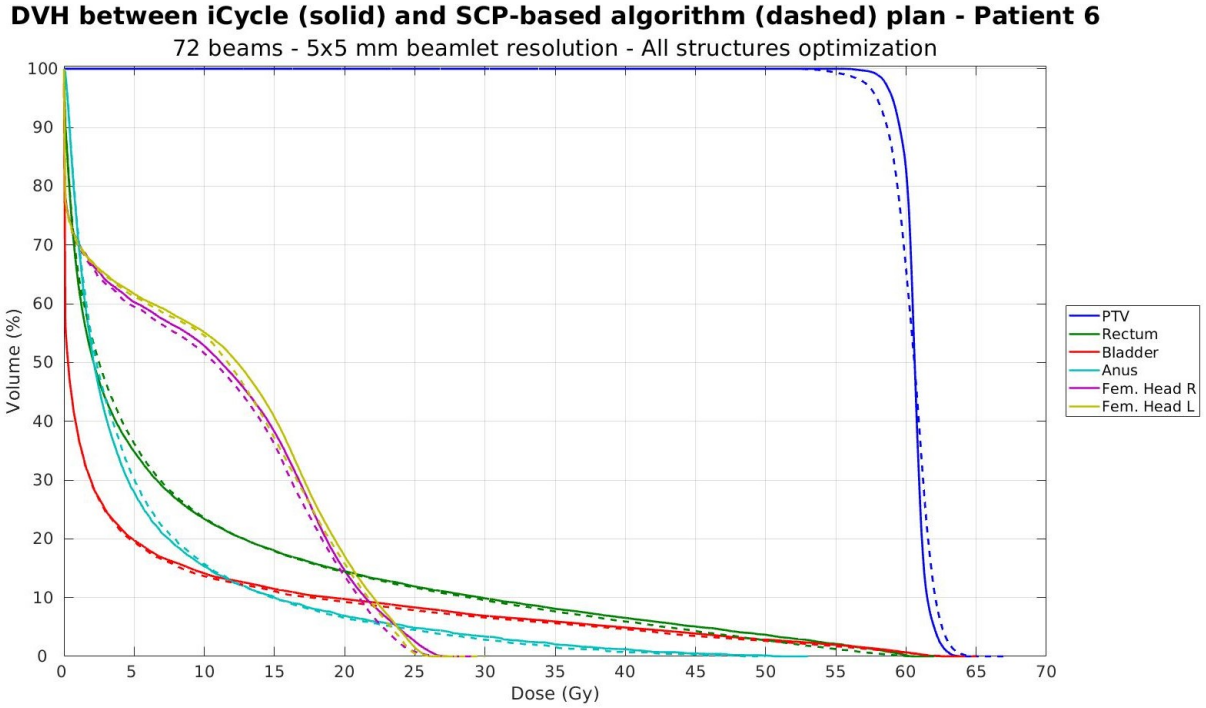

(d) DVH comparison between Erasmus-iCycle (solid) and SCP-based algorithm (dashed) for Patient 6. The plan was generated using 72 control points and a beamlet resolution of $5\,mm \times 5\,mm$, optimizing all relevant structures. The plot illustrates the balance between computational efficiency and dosimetric quality when using standard beamlet resolution with moderate angular sampling.

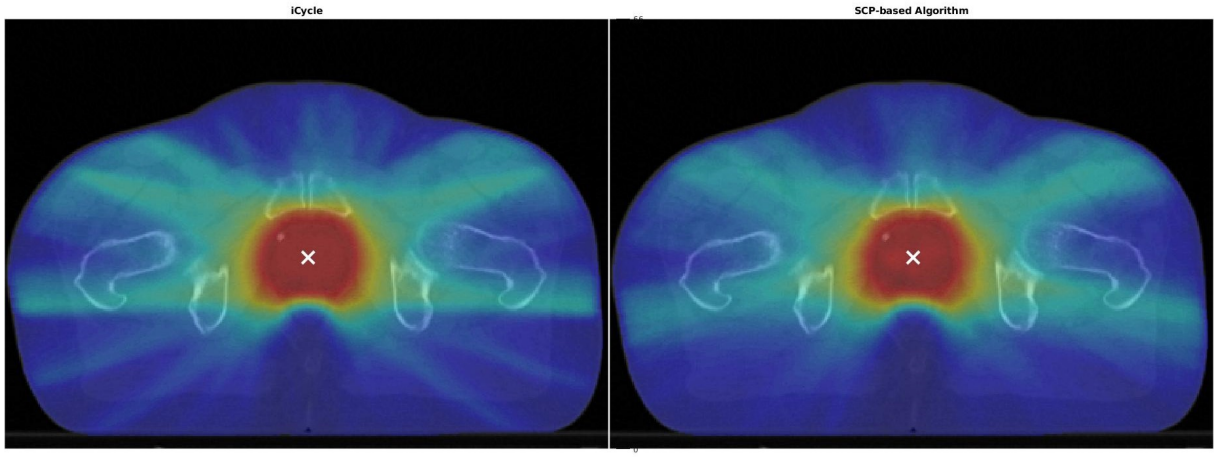

Figure 4.4: Axial dose distribution, at the isocenter, comparison between Erasmus-iCycle (left) and SCP-based algorithm (right) for Patient 6. The plans were generated using 72 control points and a beamlet resolution of 5x5 mm, optimizing all relevant structures. The images highlight the differences in dose conformity and gradient around the PTV, demonstrating the similar dose coverage achieved by both planning approaches.

Validation on the Full Patient Cohort

Following the parameter tuning performed on the selected patient, the choosen parameter set was applied to the remaining nine patients from the cohort to assess the generalizability and robustness of the SCP-based VMAT algorithm.

The DVHs and dose distributions for the rest of the patients are in the Appendix B.

4.2.2 Dosimetric Validation

Following the application of the parameter set to the full patient cohort, we compared the SCP-based VMAT plans with the reference Erasmus-iCycle plans. The evaluation focused on key dosimetric metrics related to PTV coverage and dose uniformity, including V95% (%), D98% (Gy), D2% (%), and Dmean (Gy). All the data is presented in Table 4.1.

PTV coverage

The SCP-based plans showed an average V95% of 98.05%, compared to 99.65% for the Erasmus-iCycle plans. This indicates that the SCP-based plans tend to have slightly lower PTV coverage compared to the benchmark iCycle plans. Similarly, the average D98% for SCP-based plans was 57.1 Gy, marginally lower than the Erasmus-iCycle value of 58.3 Gy. This reduction in D98% suggests that the SCP-based plans may deliver a slightly lower minimum dose to the PTV.

Regarding hot spots, the SCP-based plans exhibited an average D2% of 104.66%, which is 1.10% higher than the Erasmus-iCycle value of 103.56%. This indicates that the SCP-based method may result in slightly more pronounced dose peaks, highlighting a potential area for improvement in hotspot control. The mean dose for the PTV was nearly identical between the two methods, with SCP-based plans averaging 60.5 Gy compared to 60.6 Gy for Erasmus-iCycle. This negligible difference suggests that both planning methods deliver a consistent average dose to the PTV.

Table 4.1: Comparison of dosimetric metrics between SCP-based VMAT plans and Erasmus-iCycle plans for the full patient cohort. The table presents key metrics including PTV coverage (V95%, D98%, D2%, Dmean), OAR sparing (rectum, anus, bladder, and femoral heads), and overall patient dose metrics. Differences indicate the relative performance of SCP-based plans compared to the reference iCycle plans, green indicates dosimetric improvement or favorable outcomes (e.g., improved target coverage or reduced OAR dose), while red indicates dosimetric deterioration or less favorable outcomes (e.g., increased hotspots or elevated OAR doses) and yellow indicates that there isn't significant clinical difference

Optimization		iCycle										
Patient ID		1	2	3	4	5	6	7	8	9	10	Avg (Std)
PTV	V95% (%)	99.00	99.70	99.74	99.72	99.66	99.68	99.77	99.70	99.80	99.72	99.65 (0.22)
	D98% (Gy)	57.71	58.55	58.37	58.35	58.33	58.40	58.50	58.36	58.31	58.41	58.33 (0.22)
	D2% (%)	104.17	103.03	104.00	103.27	103.03	104.19	103.31	103.10	103.38	104.12	103.56 (0.47)
	Dmean (Gy)	60.57	60.58	60.58	60.58	60.57	60.58	60.58	60.58	60.58	60.58	60.58 (0.00)
Rectum	Dmean (Gy)	16.98	16.25	7.42	14.91	14.75	8.56	21.54	11.77	11.73	8.90	13.28 (4.20)
	V58Gy (%)	4.10	6.84	1.86	5.20	7.51	1.12	10.61	4.06	4.20	1.69	4.72 (2.80)
	V50Gy (%)	10.19	12.65	4.30	10.52	12.66	3.68	19.13	8.26	7.86	4.55	9.38 (4.51)
Anus	Dmean (Gy)	12.96	35.39	13.11	7.30	25.98	5.51	8.82	39.22	26.38	24.06	19.87 (11.37)
Bladder	Dmean (Gy)	15.95	13.71	13.48	9.78	5.66	5.43	18.25	14.46	6.80	19.59	12.31 (4.88)
L. Fem. H.	D0.001cc (Gy)	26.37	26.11	24.89	31.99	26.90	26.20	24.82	25.58	29.49	25.51	26.79 (2.14)
R. Fem. H.	D0.001cc (Gy)	23.90	26.10	23.86	31.17	27.48	27.16	19.98	27.66	28.02	28.02	26.33 (2.92)
Patient	Dmean (Gy)	4.67	4.66	3.32	4.22	3.97	3.54	3.53	5.28	3.54	3.28	4.00 (0.65)
	V30Gy (%)	3.08	2.91	2.09	2.81	2.63	2.01	1.79	3.77	2.38	2.03	2.55 (0.58)
	V15Gy (%)	11.78	11.86	8.02	10.85	9.61	8.59	8.28	13.97	9.29	8.30	10.05 (1.88)
	V3Gy (%)	26.30	27.22	20.31	23.71	24.17	22.28	23.19	28.89	19.61	19.50	23.52 (3.07)

Optimization		SCP-based Algorithm										
Patient ID		1	2	3	4	5	6	7	8	9	10	Avg (Std)
PTV	V95% (%)	96.05	98.73	98.41	98.00	98.04	97.71	98.74	98.46	98.18	98.19	98.05 (0.73)
	D98% (Gy)	56.07	57.49	57.23	57.00	57.03	56.81	57.40	57.26	57.10	57.13	57.05 (0.38)
	D2% (%)	105.12	104.35	104.53	104.77	104.64	105.17	104.41	104.16	104.46	104.97	104.66 (0.32)
	Dmean (Gy)	60.35	60.48	60.52	60.51	60.49	60.43	60.46	60.46	60.42	60.52	60.46 (0.05)
Rectum	Dmean (Gy)	16.70	15.90	7.27	14.51	14.50	8.47	21.09	11.62	11.53	8.70	13.03 (4.10)
	V58Gy (%)	2.66	5.77	1.44	4.04	6.27	0.48	8.97	3.18	3.43	1.20	3.74 (2.49)
	V50Gy (%)	8.50	11.31	3.77	9.40	11.59	2.72	17.78	7.42	7.09	3.75	8.33 (4.31)
Anus	Dmean (Gy)	12.57	34.48	12.71	7.11	25.35	5.31	8.54	38.43	25.70	23.27	19.35 (11.13)
Bladder	Dmean (Gy)	15.88	13.30	13.37	9.78	5.92	5.46	17.80	14.10	7.01	18.95	12.16 (4.63)
L. Fem. H.	D0.001cc (Gy)	27.71	26.82	25.27	31.87	27.69	27.17	25.30	26.51	30.78	26.11	27.52 (2.08)
R. Fem. H.	D0.001cc (Gy)	24.03	25.99	23.05	31.88	27.36	27.04	20.22	28.31	28.94	28.19	26.50 (3.16)
Patient	Dmean (Gy)	4.61	4.58	3.26	4.15	3.91	3.49	3.47	5.20	3.48	3.21	3.93 (0.64)
	V30Gy (%)	3.00	2.82	1.81	2.68	2.37	1.93	1.63	3.31	2.31	1.89	2.37 (0.54)
	V15Gy (%)	11.71	11.46	8.11	10.80	9.38	8.50	8.21	14.05	9.17	8.08	9.95 (1.89)
	V3Gy (%)	26.19	27.10	20.22	23.58	23.97	22.13	23.19	28.91	19.46	19.42	23.42 (3.09)

Treatment		Difference (iCycle - SCP)										
Patient ID		1	2	3	4	5	6	7	8	9	10	Avg (Std)
PTV	V95% (%)	2.95	0.97	1.33	1.72	1.61	1.96	1.03	1.24	1.62	1.53	1.60 (0.54)
	D98% (Gy)	1.64	1.06	1.13	1.35	1.30	1.59	1.10	1.10	1.21	1.28	1.28 (0.19)
	D2% (%)	-0.96	-1.31	-0.53	-1.50	-1.61	-0.97	-1.10	-1.06	-1.08	-0.85	-1.10 (0.30)
	Dmean (Gy)	0.23	0.10	0.07	0.08	0.09	0.15	0.12	0.12	0.16	0.06	0.12 (0.05)
Rectum	Dmean (Gy)	0.28	0.35	0.15	0.39	0.26	0.09	0.45	0.15	0.20	0.20	0.25 (0.11)
	V58Gy (%)	1.44	1.08	0.42	1.17	1.23	0.65	1.64	0.87	0.77	0.49	0.98 (0.38)
	V50Gy (%)	1.69	1.34	0.54	1.13	1.06	0.97	1.35	0.83	0.77	0.80	1.05 (0.32)
Anus	Dmean (Gy)	0.39	0.92	0.41	0.19	0.63	0.20	0.29	0.79	0.68	0.79	0.53 (0.25)
Bladder	Dmean (Gy)	0.07	0.41	0.11	0.00	-0.26	-0.03	0.45	0.36	-0.21	0.64	0.15 (0.28)
L. Fem. H.	D0.001cc (Gy)	-1.34	-0.71	-0.38	0.12	-0.79	-0.97	-0.48	-0.93	-1.29	-0.60	-0.74 (0.41)
R. Fem. H.	D0.001cc (Gy)	-0.13	0.11	0.80	-0.71	0.12	0.12	-0.24	-0.65	-0.93	-0.17	-0.17 (0.48)
Patient	Dmean (Gy)	0.07	0.09	0.06	0.08	0.06	0.05	0.06	0.08	0.06	0.07	0.07 (0.01)
	V30Gy (%)	0.08	0.09	0.28	0.14	0.26	0.08	0.16	0.46	0.08	0.14	0.18 (0.12)
	V15Gy (%)	0.07	0.40	-0.09	0.05	0.22	0.08	0.06	-0.08	0.12	0.22	0.10 (0.14)
	V3Gy (%)	0.11	0.12	0.10	0.13	0.20	0.15	0.00	-0.02	0.14	0.08	0.10 (0.06)

OAR Sparing

The SCP-based plans demonstrated improved sparing for most OARs compared to the Erasmus-iCycle plans. The mean dose to the rectum was slightly lower in the SCP-based plans (13.0 Gy) compared to iCycle (13.3 Gy). Additionally, the high-dose metrics for the rectum showed a reduction, with the SCP-based method achieving a V58Gy of 3.74% and a V50% of 8.33%, compared to 4.72% and 9.38% in iCycle plans, respectively.

Other OARs also showed minor differences. The mean dose to the anus was slightly lower in SCP-based plans (19.4 Gy) compared to iCycle (19.9 Gy), and the bladder mean dose was reduced from 12.3 Gy in iCycle to 12.2 Gy in SCP-based plans.

However, both femoral heads presented a small increase in D0.001cc when using the SCP-based method. The left femoral head had a D0.001cc of 27.5 Gy compared to 26.8 Gy with iCycle, and the right femoral head had a D0.001cc of 26.5 Gy compared to 26.3 Gy.

Patient Dose Metrics

The SCP-based plans also exhibited a slight reduction in overall patient dose. The mean dose was 3.93 Gy for SCP-based plans compared to 4.00 Gy for iCycle. Low-dose volume metrics, including V30Gy, V15Gy, and V3Gy, were consistently lower in SCP-based plans, indicating reduced low-dose exposure to non-target tissues.

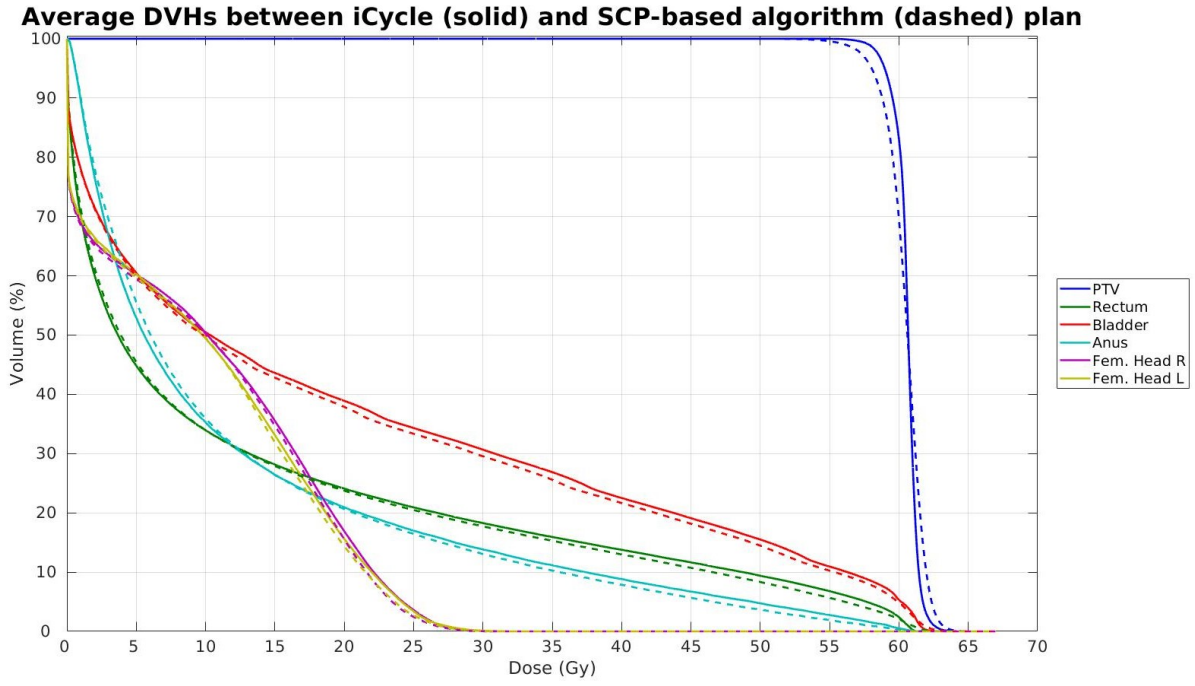

Figure 4.5: Average DVHs comparing SCP-based VMAT plans (dashed lines) and Erasmus-iCycle plans (solid lines) for the full patient cohort. The SCP-based plans demonstrate similar PTV coverage with slightly higher dose peaks (D2%) and comparable OAR sparing

4.3 Discussion

The primary objective of this study was to assess whether the SCP-based algorithm could generate VMAT segments that closely mimic the original Erasmus-iCycle plan doses. Rather than aiming to improve dosimetric quality, the SCP-based method is specifically designed to reproduce the iCycle dose distribution within the context of VMAT planning. By comparing the dosimetric outcomes between the SCP-based plans and the reference Erasmus-iCycle plans, we aimed to evaluate how accurately the SCP-based method replicates the benchmark dose patterns.

The SCP-based plans generally maintained comparable PTV coverage to the Erasmus-iCycle plans. Although the V95% and D98% metrics were slightly lower for SCP-based plans, the differences were minimal and may not be clinically significant, as the clinical goal set in Eclipse for V95% is 98%, and values above this threshold are considered acceptable. These differences could potentially be reduced by increasing the number of control points or enhancing the beamlet resolution. This slight reduction indicates that the SCP algorithm effectively replicates the iCycle dose distribution, even though maintaining the highest coverage levels in complex anatomical cases can be challenging.

A notable difference was observed in the D2% values, where SCP-based plans demonstrated slightly higher hot spots compared to Erasmus-iCycle. This outcome suggests that while the SCP algorithm is proficient at creating VMAT segments that reproduce iCycle's dose patterns, there is a tendency to generate slightly more pronounced dose peaks. Despite this, the mean dose (PTV Dmean) remained consistent between both methods, indicating that the overall dose distribution within the PTV was not significantly affected.

The SCP-based algorithm successfully replicated the OAR dose distribution patterns from the Erasmus-iCycle plans. The observed differences in OAR sparing between SCP-based and iCycle plans were relatively minor and did not indicate a systematic deviation. For instance, the mean doses to the rectum, anus, and bladder were slightly lower in SCP-based plans, but these variations likely reflect small inconsistencies inherent in reproducing complex dose distributions rather than intentional optimization or improvement.

The slight increase in dose to the femoral heads in SCP-based plans compared to Erasmus-iCycle may reflect the inherent difficulty of precisely replicating iCycle's dose patterns in peripheral structures while maintaining the overall dose distribution. This finding suggests that the SCP algorithm, while effective at dose reproduction for PTV and adjacent OARs, may require further adjustment when dealing with peripheral dose gradients.

Challenges in VMAT Segment Deliverability

Although the primary objective of the SCP-based algorithm was to reproduce the Erasmus-iCycle dose distribution, the practical deliverability of the resulting VMAT segments poses a significant challenge. While the SCP algorithm successfully generated segments that closely mimic the iCycle dose patterns, the nature of the produced segments raises concerns regarding their feasibility for real-world treatment delivery.

VMAT segments must be deliverable by the LINAC, which requires that the segments be smooth, contiguous, and feasible within the mechanical constraints of the MLC system. The SCP-based segments, however, often exhibit irregular, fragmented, or highly modulated shapes that do not comply with

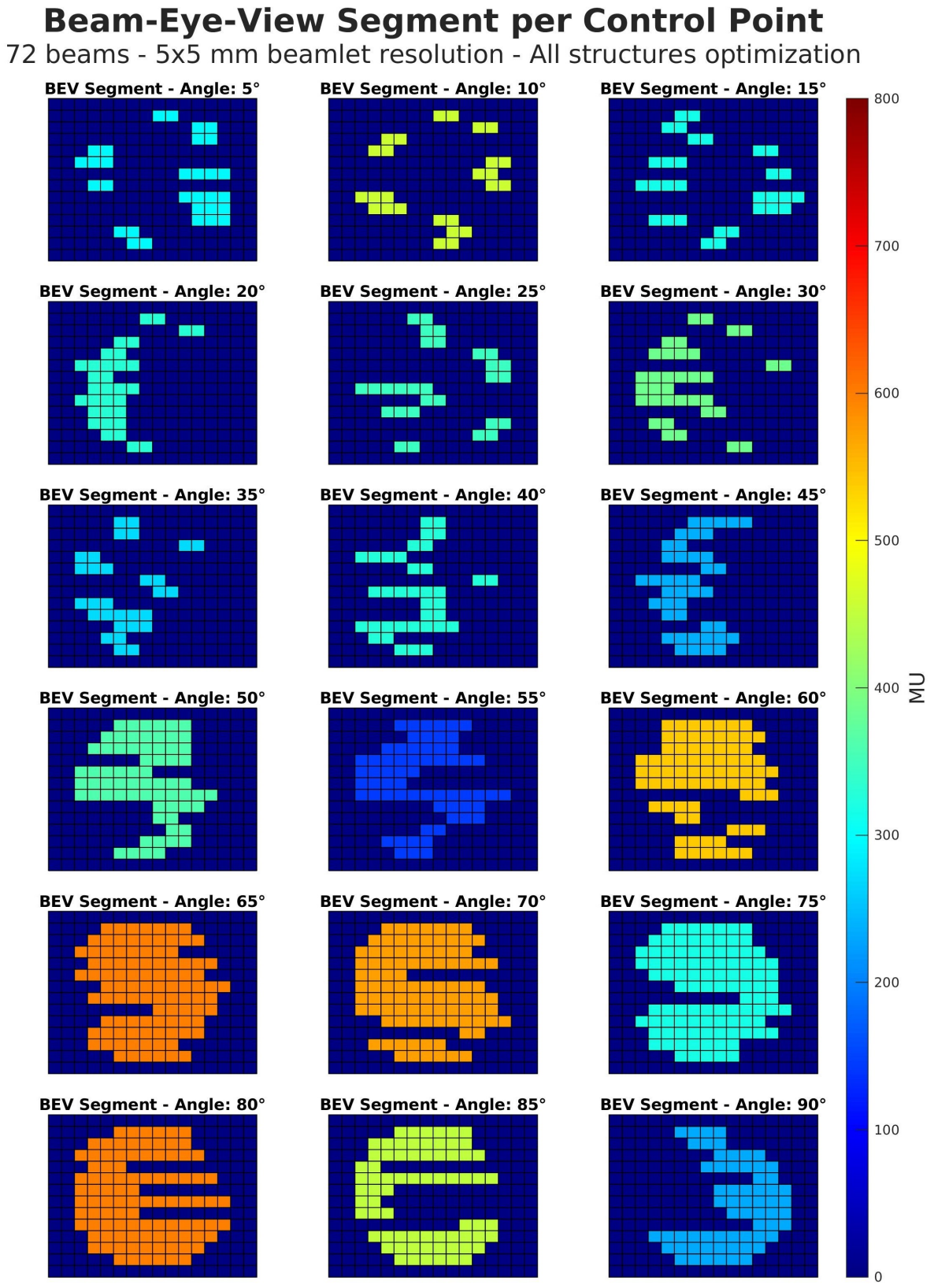

Figure 4.6: Beam-Eye-View (BEV) segments generated by the SCP-based VMAT algorithm for a range of control point angles (5° to 90°). The segments exhibit irregular and non-contiguous shapes, which, despite accurately reproducing the iCycle dose distribution, pose significant challenges for practical deliverability using standard LINAC systems.

the physical limitations of MLC movement. This discrepancy highlights a fundamental gap between mathematical optimization and practical implementation.

The image shown in Figure 4.6 illustrates the BEV segments generated by the SCP algorithm for various control points. Despite their ability to achieve the desired dose distribution, the irregular and scattered segment shapes, particularly at intermediate angles, are not deliverable as they would require rapid and complex leaf movements that are not achievable by standard LINAC hardware.

The challenge arises because the SCP algorithm is solely focused on dose reproduction rather than accounting for machine constraints. This limitation underscores the need for incorporating deliverability criteria directly into the optimization process. One potential improvement could be the introduction of additional constraints during SCP optimization to enforce smoother and more contiguous segment shapes, better aligning with clinical practice requirements.

The complete set of segments for patient 6 with an SCP optimization with the choosen set of parameters is in Appendix C.

4.4 Conclusion

The SCP-based VMAT algorithm successfully achieved its primary objective of reproducing the dose distribution generated by the Erasmus-iCycle planning system. Rather than aiming to improve the original plan, the SCP algorithm was specifically designed to replicate the dose patterns while optimizing segment shapes for each control point.

The SCP-based plans maintained comparable PTV coverage to the Erasmus-iCycle plans, with minor differences in V95% and D98% metrics. The slightly higher D2% values in SCP-based plans indicate a tendency for increased hot spots. Despite this, the mean dose remained consistent between both methods, reflecting the algorithm's ability to maintain overall dose levels.

The SCP-based method also demonstrated comparable OAR sparing to the Erasmus-iCycle plans, with slight improvements in some metrics, such as mean doses to the rectum and bladder. However, increased doses to the femoral heads highlight the need for further optimization, particularly for peripheral structures.

A key limitation is the deliverability of the generated VMAT segments, as the irregular segment shapes often do not meet LINAC requirements. Integrating deliverability constraints into the SCP optimization process is essential for clinical application.

In summary, the SCP-based algorithm is effective in replicating Erasmus-iCycle dose distributions while offering computational benefits. However, improving segment deliverability is essential to transitioning from computational models to clinical practice.

5 Final Discussion and Conclusion

This thesis aimed to develop and evaluate methods for optimizing BEV segments for each control point in VMAT within the context of External Radiotherapy. Two primary approaches were explored: 1) Integration between iCycle and Eclipse to establish a benchmark, and 2) a native algorithm based on SCP to reproduce the Erasmus-iCycle dose distribution in VMAT plans.

The first approach focused on translating iCycle-generated plans into deliverable VMAT plans within the Eclipse TPS. A dataset of 10 patients was used to evaluate the translation process and compare the dosimetric quality between the original iCycle plans and the resulting VMAT plans. Once the optimization workflow was identified, it was applied to the remaining nine patients. The goal was to analyze the dosimetric quality of the resulting VMAT plans when benchmarked against the original iCycle plans.

The results demonstrated that the integration between iCycle and Eclipse allowed for the generation of VMAT plans that closely approximated the dosimetric characteristics of the original iCycle plans. The optimization workflow, determined through testing on the initial patient, provided a consistent approach that could be generalized across the remaining patient dataset.

In the second approach, a native SCP-based algorithm was implemented with the objective of reproducing the Erasmus-iCycle dose distribution. Unlike traditional optimization methods that aim to improve dose quality, this approach was focused on replicating the iCycle plan characteristics within a VMAT framework. The results indicated that the SCP-based method successfully maintained dose distribution fidelity, aligning closely with the iCycle benchmarks.

Another limitation of this work is the absence of formal statistical analysis across the patient cohort. While descriptive comparisons provided valuable insights into the performance of both approaches, statistical testing would have allowed a more rigorous assessment of inter-patient variability and strengthened the generalizability of the findings.

One of the key findings of this research was the demonstration that the iCycle-to-Eclipse translation process could be streamlined through the proposed parameter optimization method. Additionally, the SCP-based algorithm showcased its potential to serve as a reliable tool for reproducing existing dose distributions, rather than creating novel optimizations.

Future work may focus on enhancing the SCP-based method to incorporate quality improvements while preserving the original iCycle plan characteristics. This could be achieved by promoting aperture shape regularity and encouraging similarity between neighboring apertures, which are known to improve plan deliverability and reduce modulation complexity. Notably, recent work by Dursun [79] has demonstrated the successful clinical implementation of a fully automated SCP-based VMAT planning algorithm that integrates convex surrogate metrics for plan complexity and uses Eclipse scripting to streamline clinical deployment. While this publication became available only after the conclusion of this thesis, it validates the direction pursued here and highlights further opportunities to refine SCP-based optimization with clinically meaningful delivery constraints. Additionally, further investigation into the scalability of the method across different clinical scenarios and tumor sites may offer valuable insights into its broader applicability.

In conclusion, this thesis contributes to the field of radiotherapy planning by offering a structured approach to optimizing VMAT plans based on existing iCycle benchmarks. The integration with Eclipse and the development of an SCP-based method reflect practical solutions for enhancing plan deliverability while maintaining dosimetric fidelity. This work lays the foundation for future innovations in automated radiotherapy plan translation and optimization.

Bibliography

[1] P. W. Voet, M. L. Dirkx, S. Breedveld, A. Al-Mamgani, L. Incrocci, and B. J. Heijmen, "Fully automated volumetric modulated arc therapy plan generation for prostate cancer patients," *International Journal of Radiation Oncology, Biology and Physics*, vol. 88, no. 5, pp. 1175–1179, Apr. 2014. [Online]. Available: https://doi.org/10.1016/j.ijrobp.2013.12.046

[2] J. S. Brown, S. R. Amend, R. H. Austin, R. A. Gatenby, E. U. Hammarlund, and K. J. Pienta, "Updating the definition of cancer," *Molecular Cancer Research*, vol. 21, no. 11, p. 1142–1147, Jul. 2023. [Online]. Available: http://dx.doi.org/10.1158/1541-7786.MCR-23-0411

[3] C. O. Nordling, "A new theory on the cancer-inducing mechanism," *British Journal of Cancer*, vol. 7, no. 1, p. 68–72, Mar. 1953. [Online]. Available: http://dx.doi.org/10.1038/bjc.1953.8

[4] D. Hanahan and R. A. Weinberg, "The hallmarks of cancer," *Cell*, vol. 100, no. 1, p. 57–70, Jan. 2000. [Online]. Available: http://dx.doi.org/10.1016/S0092-8674(00)81683-9

[5] R. S. Wong, "Apoptosis in cancer: from pathogenesis to treatment," *Journal of Experimental &amp Clinical Cancer Research*, vol. 30, no. 1, Sep. 2011. [Online]. Available: https://doi.org/10.1186/1756-9966-30-87

[6] N. Mizushima and M. Komatsu, "Autophagy: Renovation of cells and tissues," *Cell*, vol. 147, no. 4, pp. 728–741, Nov. 2011. [Online]. Available: https://doi.org/10.1016/j.cell.2011.10.026

[7] M. P. Engbersen, W. Van Driel, D. Lambregts, and M. Lahaye, "The role of ct, pet-ct, and mri in ovarian cancer," *The British Journal of Radiology*, vol. 94, no. 1125, p. 20210117, Sep. 2021. [Online]. Available: http://dx.doi.org/10.1259/bjr.20210117

[8] D. Lother, M. Robert, E. Elwood, S. Smith, N. Tunariu, S. R. Johnston, M. Parton, B. Bhaludin, T. Millard, K. Downey, and B. Sharma, "Imaging in metastatic breast cancer, ct, pet/ct, mri, wb-dwi, cca: review and new perspectives," *Cancer Imaging*, vol. 23, no. 1, May 2023. [Online]. Available: http://dx.doi.org/10.1186/s40644-023-00557-8

[9] S. Kijima, "Preoperative evaluation of colorectal cancer using ct colonography, mri, and pet/ct," *World Journal of Gastroenterology*, vol. 20, no. 45, p. 16964, 2014. [Online]. Available: http://dx.doi.org/10.3748/wjg.v20.i45.16964

[10] H. S. Kim, K. S. Lee, Y. Ohno, E. J. van Beek, and J. Biederer, "Pet/ct versus mri for diagnosis, staging, and follow-up of lung cancer: Pet/ct versus mri in lung cancer," *Journal of Magnetic Resonance Imaging*, vol. 42, no. 2, p. 247–260, Nov. 2014. [Online]. Available: http://dx.doi.org/10.1002/jmri.24776

[11] T. Szyszko and G. Cook, "Pet/ct and pet/mri in head and neck malignancy," *Clinical Radiology*, vol. 73, no. 1, p. 60–69, Jan. 2018. [Online]. Available: http://dx.doi.org/10.1016/j.crad.2017.09.001

[12] S. Gupta and D. C. Madoff, "Image-guided percutaneous needle biopsy in cancer diagnosis and staging," *Techniques in Vascular and Interventional Radiology*, vol. 10, no. 2, p. 88–101, Jun. 2007. [Online]. Available: http://dx.doi.org/10.1053/j.tvir.2007.09.005

[13] K. L. Obstein, "Advanced endoscopic technologies for colorectal cancer screening," *World Journal of Gastroenterology*, vol. 19, no. 4, p. 431, 2013. [Online]. Available: http://dx.doi.org/10.3748/wjg.v19.i4.431

[14] C.-H. Chang, K.-C. Kao, H.-C. Hu, C.-Y. Hung, L.-F. Li, C.-Y. Wu, C.-W. Wang, J.-Y. Fu, C.-C. Huang, N.-H. Chen, C.-T. Yang, and Y.-H. Tsai, "The utility of surgical lung biopsy in cancer patients with acute respiratory distress syndrome," *Journal of Cardiothoracic Surgery*, vol. 8, no. 1, May 2013. [Online]. Available: http://dx.doi.org/10.1186/1749-8090-8-128

[15] B. M. Cranfield, M. M. Koo, G. A. Abel, R. Swann, S. McPhail, G. P. Rubin, and G. Lyratzopoulos, "Primary care blood tests before cancer diagnosis: National cancer diagnosis audit data," *British Journal of General Practice*, vol. 73, no. 727, p. e95–e103, Sep. 2022. [Online]. Available: http://dx.doi.org/10.3399/BJGP.2022.0265

[16] J. D. Cohen, L. Li, Y. Wang, C. Thoburn, B. Afsari, L. Danilova, C. Douville, A. A. Javed, F. Wong, A. Mattox, R. H. Hruban, C. L. Wolfgang, M. G. Goggins, M. Dal Molin, T.-L. Wang, R. Roden, A. P. Klein, J. Ptak, L. Dobbyn, J. Schaefer, N. Silliman, M. Popoli, J. T. Vogelstein, J. D. Browne, R. E. Schoen, R. E. Brand, J. Tie, P. Gibbs, H.-L. Wong, A. S. Mansfield, J. Jen, S. M. Hanash, M. Falconi, P. J. Allen, S. Zhou, C. Bettegowda, L. A. Diaz, C. Tomasetti, K. W. Kinzler, B. Vogelstein, A. M. Lennon, and N. Papadopoulos, "Detection and localization of surgically resectable cancers with a multi-analyte blood test," *Science*, vol. 359, no. 6378, p. 926–930, Feb. 2018. [Online]. Available: http://dx.doi.org/10.1126/science.aar3247

[17] J. J. Bergman, "The endoscopic diagnosis and staging of oesophageal adenocarcinoma," *Best Practice amp; Research Clinical Gastroenterology*, vol. 20, no. 5, p. 843–866, Jan. 2006. [Online]. Available: http://dx.doi.org/10.1016/j.bpg.2006.04.010

[18] D. H. Sekons, C. K. McSherry, W. Calhoun, B. Pudalov, H. L. Beaton, and H. Shinya, "Contribution of endoscopy to diagnosis and treatment of gastric cancer," *The American Journal of Surgery*, vol. 147, no. 5, p. 662–665, May 1984. [Online]. Available: http://dx.doi.org/10.1016/0002-9610(84)90136-3

[19] M. A. Richards, "The size of the prize for earlier diagnosis of cancer in england," *British Journal of Cancer*, vol. 101, no. S2, pp. S125–S129, Dec. 2009. [Online]. Available: https://doi.org/10.1038/sj.bjc.6605402

[20] J. Wardle, K. Robb, S. Vernon, and J. Waller, "Screening for prevention and early diagnosis of cancer." *American Psychologist*, vol. 70, no. 2, pp. 119–133, Feb. 2015. [Online]. Available: https://doi.org/10.1037/a0037357

[21] P. Denoix, "Tumor, node and metastasis (tnm)," *Bull Inst Nat Hyg (Paris)*, vol. 1, no. 1, pp. 1–69, 1944.

[22] M. Arruebo, N. Vilaboa, B. Sáez-Gutierrez, J. Lambea, A. Tres, M. Valladares, and Á. González-Fernández, "Assessment of the evolution of cancer treatment therapies," *Cancers*, vol. 3, no. 3, pp. 3279–3330, Aug. 2011. [Online]. Available: https://doi.org/10.3390/cancers3033279

[23] J. Coffey, J. Wang, M. Smith, D. Bouchier-Hayes, T. Cotter, and H. Redmond, "Excisional surgery for cancer cure: therapy at a cost," *The Lancet Oncology*, vol. 4, no. 12, pp. 760–768, Dec. 2003. [Online]. Available: https://doi.org/10.1016/s1470-2045(03)01282-8

[24] P. Nygren, "What is cancer chemotherapy?" *Acta Oncologica*, vol. 40, no. 2–3, p. 166–174, Jan. 2001. [Online]. Available: http://dx.doi.org/10.1080/02841860151116204

[25] K. L. Jones and A. U. Buzdar, "A review of adjuvant hormonal therapy in breast cancer," *Endocrine-Related Cancer*, vol. 11, no. 3, pp. 391–406, Sep. 2004. [Online]. Available: https://doi.org/10.1677/erc.1.00594

[26] B. A. Hellerstedt and K. J. Pienta, "The current state of hormonal therapy for prostate cancer," *CA: A Cancer Journal for Clinicians*, vol. 52, no. 3, pp. 154–179, May 2002. [Online]. Available: https://doi.org/10.3322/canjclin.52.3.154

[27] S. P. Jackson and J. Bartek, "The dna-damage response in human biology and disease," *Nature*, vol. 461, no. 7267, p. 1071–1078, Oct. 2009. [Online]. Available: http://dx.doi.org/10.1038/nature08467

[28] R. Baskar, K. A. Lee, R. Yeo, and K.-W. Yeoh, "Cancer and radiation therapy: Current advances and future directions," *International Journal of Medical Sciences*, vol. 9, no. 3, p. 193–199, 2012. [Online]. Available: http://dx.doi.org/10.7150/ijms.3635

[29] E. P. Balogh, P. A. Ganz, S. B. Murphy, S. J. Nass, B. R. Ferrell, and E. Stovall, "Patient-centered cancer treatment planning: Improving the quality of oncology care. summary of an institute of medicine workshop," *The Oncologist*, vol. 16, no. 12, p. 1800–1805, Nov. 2011. [Online]. Available: http://dx.doi.org/10.1634/theoncologist.2011-0252

[30] E. S. M Hewitt, S Greenfield, *From cancer patient to cancer survivor: lost in transition*. National Academies Press, Oct. 2005. [Online]. Available: http://dx.doi.org/10.17226/11468

[31] L. A. Jacobs and L. N. Shulman, "Follow-up care of cancer survivors: challenges and solutions," *The Lancet Oncology*, vol. 18, no. 1, p. e19–e29, Jan. 2017. [Online]. Available: http://dx.doi.org/10.1016/S1470-2045(16)30386-2

[32] W. Nakel, "The elementary process of bremsstrahlung," *Physics Reports*, vol. 243, no. 6, p. 317–353, Jul. 1994. [Online]. Available: http://dx.doi.org/10.1016/0370-1573(94)00068-9

[33] H. Becquerel, "Sur les radiations invisible emises par les corps phosphorescents," *Comptes rendus*, vol. 122, pp. 501–503, 1896.

[34] E. Podgorsak and S. H. Benedict, *Review of Radiation Oncology Physics: A Handbook for Teachers and Students*. International Atomic Energy Agency, 2004. [Online]. Available: http://www-naweb.iaea.org/nahu/DMRP/RadiationOncologyPhysicsHandbook.html

[35] A. EINSTEIN, *On a Heuristic Point of View about the Creation and Conversion of Light*. Elsevier, 1967, p. 91–107. [Online]. Available: http://dx.doi.org/10.1016/B978-0-08-012102-4.50014-0

[36] A. H. Compton, "A quantum theory of the scattering of x-rays by light elements," *Physical Review*, vol. 21, no. 5, p. 483–502, May 1923. [Online]. Available: http://dx.doi.org/10.1103/physrev.21.483

[37] C. D. Anderson, "Energies of cosmic-ray particles," *Physical Review*, vol. 41, no. 4, p. 405–421, Aug. 1932. [Online]. Available: http://dx.doi.org/10.1103/PhysRev.41.405

[38] BIPM, *Le Système international d'unités / The International System of Units ('The SI Brochure')*, 9th ed. Bureau international des poids et mesures, 2019. [Online]. Available: http://www.bipm.org/en/si/si_brochure/

[39] J. song Wang, H. juan Wang, and H. li Qian, "Biological effects of radiation on cancer cells," *Military Medical Research*, vol. 5, no. 1, Jun. 2018. [Online]. Available: https://doi.org/10.1186/s40779-018-0167-4

[40] G. Smyth, P. M. Evans, J. C. Bamber, and J. L. Bedford, "Recent developments in non-coplanar radiotherapy," *The British Journal of Radiology*, vol. 92, no. 1097, p. 20180908, May 2019. [Online]. Available: https://doi.org/10.1259/bjr.20180908

[41] E. Wild, M. Bangert, S. Nill, and U. Oelfke, "Noncoplanar VMAT for nasopharyngeal tumors: Plan quality versus treatment time," *Medical Physics*, vol. 42, no. 5, pp. 2157–2168, Apr. 2015. [Online]. Available: https://doi.org/10.1118/1.4914863

[42] J. Thariat, J.-M. Hannoun-Levi, A. Sun Myint, T. Vuong, and J.-P. Gérard, "Past, present, and future of radiotherapy for the benefit of patients," *Nature Reviews Clinical Oncology*, vol. 10, no. 1, p. 52–60, Nov. 2012. [Online]. Available: http://dx.doi.org/10.1038/nrclinonc.2012.203

[43] M. Teoh, C. H. Clark, K. Wood, S. Whitaker, and A. Nisbet, "Volumetric modulated arc therapy: a review of current literature and clinical use in practice," *The British Journal of Radiology*, vol. 84, no. 1007, pp. 967–996, Nov. 2011. [Online]. Available: https://doi.org/10.1259/bjr/22373346

[44] D. A. Jaffray, "Image-guided radiotherapy: from current concept to future perspectives," *Nature Reviews Clinical Oncology*, vol. 9, no. 12, p. 688–699, Nov. 2012. [Online]. Available: http://dx.doi.org/10.1038/nrclinonc.2012.194

[45] A. Bujold, T. Craig, D. Jaffray, and L. A. Dawson, "Image-guided radiotherapy: Has it influenced patient outcomes?" *Seminars in Radiation Oncology*, vol. 22, no. 1, pp. 50–61, Jan. 2012. [Online]. Available: https://doi.org/10.1016/j.semradonc.2011.09.001

[46] A. Taylor, "Intensity-modulated radiotherapy - what is it?" *Cancer Imaging*, vol. 4, no. 2, pp. 68–73, 2004. [Online]. Available: https://doi.org/10.1102/1470-7330.2004.0003

[47] K. Cheung, "Intensity modulated radiotherapy: advantages, limitations and future development," *Biomedical Imaging and Intervention Journal*, vol. 2, no. 1, Jan. 2006. [Online]. Available: https://doi.org/10.2349/biij.2.1.e19

[48] S. Rana, "Intensity modulated radiation therapy versus volumetric intensity modulated arc therapy," *Journal of Medical Radiation Sciences*, vol. 60, no. 3, pp. 81–83, Aug. 2013. [Online]. Available: https://doi.org/10.1002/jmrs.19

[49] T. Bortfeld, "IMRT: a review and preview," *Physics in Medicine and Biology*, vol. 51, no. 13, pp. R363–R379, Jun. 2006. [Online]. Available: https://doi.org/10.1088/0031-9155/51/13/r21

[50] M. Bangert, "New concepts for beam angle selection in imrt treatment planning : From heuristics to combinatorial optimization," Ph.D. dissertation, 2011. [Online]. Available: http://archiv.ub.uni-heidelberg.de/volltextserver/id/eprint/12272

[51] S. O. Hunte, C. H. Clark, N. Zyuzikov, and A. Nisbet, "Volumetric modulated arc therapy (vmat): a review of clinical outcomes—what is the clinical evidence for the most effective implementation?" *The British Journal of Radiology*, vol. 95, no. 1136, Aug. 2022. [Online]. Available: http://dx.doi.org/10.1259/bjr.20201289

[52] B. T. Nguyen, C. Hornby, T. Kron, J. Cramb, A. Rolfo, D. Pham, A. Haworth, K. Tai, and F. Foroudi, "Optimising the dosimetric quality and efficiency of post-prostatectomy radiotherapy: A planning study comparing the performance of volumetric-modulated arc therapy (vmat) with an optimised seven-field intensity-modulated radiotherapy (imrt) technique," *Journal of Medical Imaging and Radiation Oncology*, vol. 56, no. 2, p. 211–219, Apr. 2012. [Online]. Available: http://dx.doi.org/10.1111/j.1754-9485.2011.02324.x

[53] S. Breedveld, P. R. M. Storchi, P. W. J. Voet, and B. J. M. Heijmen, "iCycle: Integrated, multicriterial beam angle, and profile optimization for generation of coplanar and noncoplanar IMRT plans," *Medical Physics*, vol. 39, no. 2, pp. 951–963, Jan. 2012. [Online]. Available: https://doi.org/10.1118/1.3676689

[54] H. Menon, C. Guo, V. Verma, and C. B. Simone, "The role of positron emission tomography imaging in radiotherapy target delineation," *PET Clinics*, vol. 15, no. 1, pp. 45–53, Jan. 2020. [Online]. Available: https://doi.org/10.1016/j.cpet.2019.08.002

[55] V. Verma, J. I. Choi, A. Sawant, R. P. Gullapalli, W. Chen, A. Alavi, and C. B. Simone, "Use of PET and other functional imaging to guide target delineation in radiation oncology," *Seminars in Radiation Oncology*, vol. 28, no. 3, pp. 171–177, Jul. 2018. [Online]. Available: https://doi.org/10.1016/j.semradonc.2018.02.001

[56] W. C. Sleeman IV, S. Srinivasan, P. Ghosh, J. Palta, and R. Kapoor, *Big data applications in radiation oncology: challenges and opportunities*. IOP Publishing, Oct. 2022, pp. 8–1–8–28. [Online]. Available: http://dx.doi.org/10.1088/978-0-7503-3603-1ch8

[57] P. Nilsson, C. Ceberg, E. Kjellén, G. Gagliardi, K. Blomgren, S. Nilsson, M. Johansson, and B. Glimelius, "A template for writing radiotherapy protocols," *Acta Oncologica*, vol. 54, no. 2, p. 275–279, Dec. 2014. [Online]. Available: http://dx.doi.org/10.3109/0284186X.2014.981285

[58] I. J. Boero, A. J. Paravati, B. Xu, E. E. Cohen, L. K. Mell, Q.-T. Le, and J. D. Murphy, "Importance of radiation oncologist experience among patients with head-and-neck cancer treated with intensity-modulated radiation therapy," *Journal of Clinical Oncology*, vol. 34, no. 7, pp. 684–690, Mar. 2016. [Online]. Available: https://doi.org/10.1200/jco.2015.63.9898

[59] V. Batumalai, M. G. Jameson, D. F. Forstner, P. Vial, and L. C. Holloway, "How important is dosimetrist experience for intensity modulated radiation therapy? a comparative analysis of a head and neck case," *Practical Radiation Oncology*, vol. 3, no. 3, pp. e99–e106, Jul. 2013. [Online]. Available: https://doi.org/10.1016/j.prro.2012.06.009

[60] B. E. Nelms, G. Robinson, J. Markham, K. Velasco, S. Boyd, S. Narayan, J. Wheeler, and M. L. Sobczak, "Variation in external beam treatment plan quality: An inter-institutional study of planners and planning systems," *Practical Radiation Oncology*, vol. 2, no. 4, pp. 296–305, Oct. 2012. [Online]. Available: https://doi.org/10.1016/j.prro.2011.11.012

[61] R. Drzymala, R. Mohan, L. Brewster, J. Chu, M. Goitein, W. Harms, and M. Urie, "Dose-volume histograms," *International Journal of Radiation Oncology*Biology*Physics*, vol. 21, no. 1, p. 71–78, May 1991. [Online]. Available: http://dx.doi.org/10.1016/0360-3016(91)90168-4

[62] G. Bolzicco, M. S. Favretto, N. Satariano, E. Scremin, C. Tambone, and A. Tasca, "A single-center study of 100 consecutive patients with localized prostate cancer treated with stereotactic body radiotherapy," *BMC Urology*, vol. 13, no. 1, Oct. 2013. [Online]. Available: http://dx.doi.org/10.1186/1471-2490-13-49

[63] P. W. Voet, M. L. Dirkx, S. Breedveld, D. Fransen, P. C. Levendag, and B. J. Heijmen, "Toward fully automated multicriterial plan generation: A prospective clinical study," *International Journal of Radiation Oncology, Biology and Physics*, vol. 85, no. 3, pp. 866–872, Mar. 2013. [Online]. Available: https://doi.org/10.1016/j.ijrobp.2012.04.015

[64] A. W. M. Sharfo, S. Breedveld, P. W. J. Voet, S. T. Heijkoop, J.-W. M. Mens, M. S. Hoogeman, and B. J. M. Heijmen, "Validation of fully automated VMAT plan generation for library-based plan-of-the-day cervical cancer radiotherapy," *PLOS ONE*, vol. 11, no. 12, p. e0169202, Dec. 2016. [Online]. Available: https://doi.org/10.1371/journal.pone.0169202

[65] G. D. Gala, M. L. P. Dirkx, N. Hoekstra, D. Fransen, N. Lanconelli, M. van de Pol, B. J. M. Heijmen, and S. F. Petit, "Fully automated VMAT treatment planning for advanced-stage NSCLC patients," *Strahlentherapie und Onkologie*, vol. 193, no. 5, pp. 402–409, Mar. 2017. [Online]. Available: https://doi.org/10.1007/s00066-017-1121-1

[66] D. Buergy, A. W. M. Sharfo, B. J. M. Heijmen, P. W. J. Voet, S. Breedveld, F. Wenz, F. Lohr, and F. Stieler, "Fully automated treatment planning of spinal metastases – a comparison to manual planning of volumetric modulated arc therapy for conventionally fractionated irradiation," *Radiation Oncology*, vol. 12, no. 1, Jan. 2017. [Online]. Available: https://doi.org/10.1186/s13014-017-0767-2

[67] M. Buschmann, A. W. M. Sharfo, J. Penninkhof, Y. Seppenwoolde, G. Goldner, D. Georg, S. Breedveld, and B. J. M. Heijmen, "Automated volumetric modulated arc therapy planning for whole pelvic prostate radiotherapy," *Strahlentherapie und Onkologie*, vol. 194, no. 4, pp. 333–342, Dec. 2017. [Online]. Available: https://doi.org/10.1007/s00066-017-1246-2

[68] A. W. M. Sharfo, F. Stieler, O. Kupfer, B. J. M. Heijmen, M. L. P. Dirkx, S. Breedveld, F. Wenz, F. Lohr, J. Boda-Heggemann, and D. Buergy, "Automated VMAT planning for postoperative adjuvant treatment of advanced gastric cancer," *Radiation Oncology*, vol. 13, no. 1, Apr. 2018. [Online]. Available: https://doi.org/10.1186/s13014-018-1032-z

[69] M. Hussein, B. J. M. Heijmen, D. Verellen, and A. Nisbet, "Automation in intensity modulated radiotherapy treatment planning—a review of recent innovations," *The British Journal of Radiology*, vol. 91, no. 1092, p. 20180270, Dec. 2018. [Online]. Available: https://doi.org/10.1259/bjr.20180270

[70] A. W. M. Sharfo, P. W. Voet, S. Breedveld, J. W. M. Mens, M. S. Hoogeman, and B. J. Heijmen, "Comparison of VMAT and IMRT strategies for cervical cancer patients using automated planning," *Radiotherapy and Oncology*, vol. 114, no. 3, pp. 395–401, Mar. 2015. [Online]. Available: https://doi.org/10.1016/j.radonc.2015.02.006

[71] L. Cozzi, R. Vanderstraeten, A. Fogliata, F.-L. Chang, and P.-M. Wang, "The role of a knowledge based dose–volume histogram predictive model in the optimisation of intensity-modulated proton plans for hepatocellular carcinoma patients," *Strahlentherapie und Onkologie*, vol. 197, no. 4, pp. 332–342, Jul. 2020. [Online]. Available: https://doi.org/10.1007/s00066-020-01664-2

[72] K. Fjellanger, L. B. Hysing, B. J. M. Heijmen, H. E. S. Pettersen, I. M. Sandvik, T. H. Sulen, S. Breedveld, and L. Rossi, "Enhancing radiotherapy for locally advanced non-small cell lung cancer patients with ice, a novel system for automated multi-criterial treatment planning including beam angle optimization," *Cancers*, vol. 13, no. 22, p. 5683, Nov. 2021. [Online]. Available: http://dx.doi.org/10.3390/cancers13225683

[73] J. Unkelbach, T. Bortfeld, D. Craft, M. Alber, M. Bangert, R. Bokrantz, D. Chen, R. Li, L. Xing, C. Men, S. Nill, D. Papp, E. Romeijn, and E. Salari, "Optimization approaches to volumetric modulated arc therapy planning," *Medical Physics*, vol. 42, no. 3, pp. 1367–1377, Feb. 2015. [Online]. Available: https://doi.org/10.1118/1.4908224

[74] S. Breedveld, D. Craft, R. van Haveren, and B. Heijmen, "Multi-criteria optimization and decision-making in radiotherapy," *European Journal of Operational Research*, vol. 277, no. 1, pp. 1–19, Aug. 2019. [Online]. Available: https://doi.org/10.1016/j.ejor.2018.08.019

[75] K. Otto, "Volumetric modulated arc therapy: IMRT in a single gantry arc," *Medical Physics*, vol. 35, no. 1, pp. 310–317, Dec. 2007. [Online]. Available: https://doi.org/10.1118/1.2818738

[76] S. Ulrich, S. Nill, and U. Oelfke, "Development of an optimization concept for arc-modulated cone beam therapy," *Physics in Medicine and Biology*, vol. 52, no. 14, pp. 4099–4119, Jun. 2007. [Online]. Available: https://doi.org/10.1088/0031-9155/52/14/006

[77] P. Dursun, M. Zarepisheh, G. Jhanwar, and J. O. Deasy, "Solving the volumetric modulated arc therapy (VMAT) problem using a sequential convex programming method," *Physics in Medicine &amp Biology*, vol. 66, no. 8, p. 085004, Apr. 2021. [Online]. Available: https://doi.org/10.1088/1361-6560/abee58

[78] K. Schittkowski and C. Zillober, "Sequential convex programming methods," in *Lecture Notes in Economics and Mathematical Systems*. Springer Berlin Heidelberg, 1995, pp. 123–141. [Online]. Available: https://doi.org/10.1007/978-3-642-88272-2_8

[79] P. Dursun, L. Hong, G. Jhanwar, Q. Huang, Y. Zhou, J. Yang, H. Pham, L. Cervino, J. M. Moran, J. O. Deasy, and M. Zarepisheh, "Automated vmat treatment planning using sequential convex programming: algorithm development and clinical implementation," *Physics in Medicine amp; Biology*, vol. 68, no. 15, p. 155006, Jul. 2023. [Online]. Available: http://dx.doi.org/10.1088/1361-6560/ace09e

A iCycle-Eclipse Translation: Patient-Specific DVHs and Dose Distributions

Figure A.1: Comparison of Dose Distribution and DVH Between Erasmus-iCycle and Eclipse Plans: Comparison of the dose distribution and DVHs for Patient 1, illustrating the differences between the iCycle (pre-optimized) and Eclipse (final optimized) VMAT plans. The bottom subfigure shows the transverse dose distributions, while the top subfigure presents the DVH analysis of the PTV and OARs.

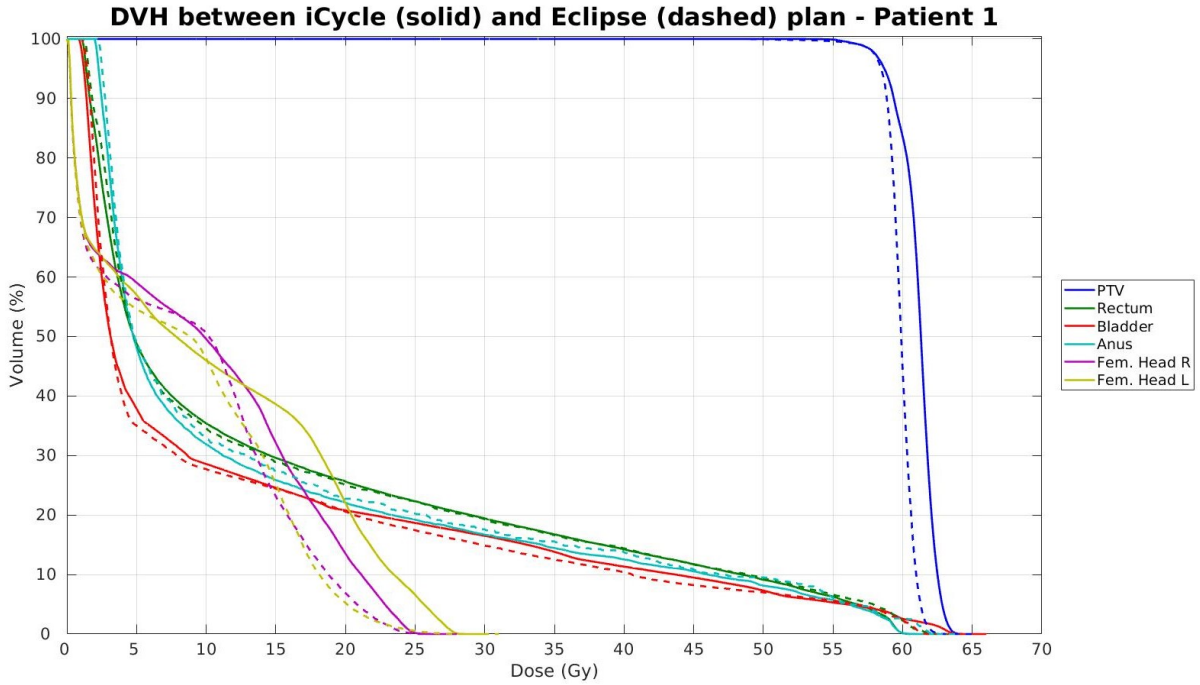

(a) Dose-Volume Histogram : DVH comparison for Patient 1, showing dose distributions for the PTV and OARs. The iCycle plan (solid lines) achieves better OAR sparing, particularly for the bladder and rectum, while maintaining target coverage, compared to the Eclipse plan (dashed lines).

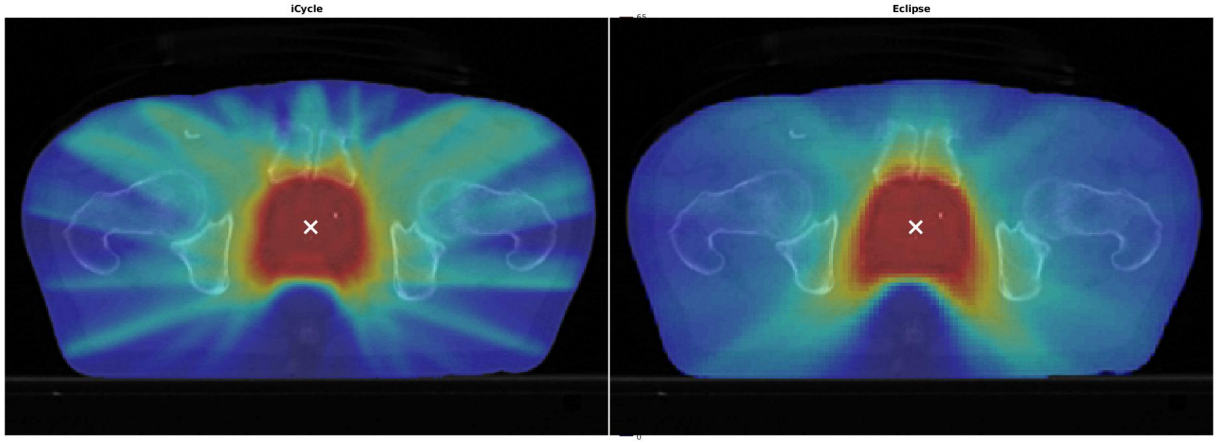

(b) Transverse Dose Distribution: Transverse dose distribution for iCycle (left) and Eclipse (right) plans. The iCycle plan exhibits a more modulated dose pattern, whereas Eclipse results in a smoother dose fall-off. The PTV coverage is comparable, but there are visible differences in dose spillage and modulation.

Figure A.2: Comparison of Dose Distribution and DVH Between Erasmus-iCycle and Eclipse Plans: Comparison of the dose distribution and DVHs for Patient 2, illustrating the differences between the iCycle (pre-optimized) and Eclipse (final optimized) VMAT plans. The bottom subfigure shows the transverse dose distributions, while the top subfigure presents the DVH analysis of the PTV and OARs.

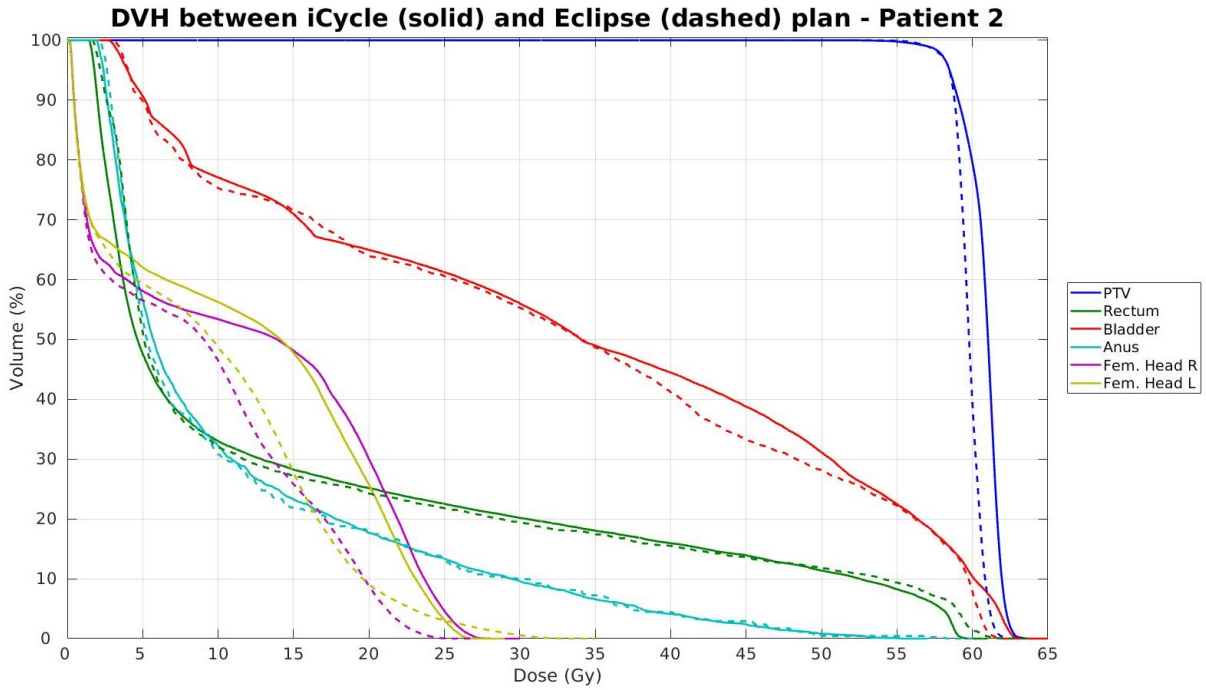

(a) Dose-Volume Histogram : DVH comparison for Patient 2, showing dose distributions for the PTV and OARs. The iCycle plan (solid lines) achieves better OAR sparing, particularly for the bladder and rectum, while maintaining target coverage, compared to the Eclipse plan (dashed lines).

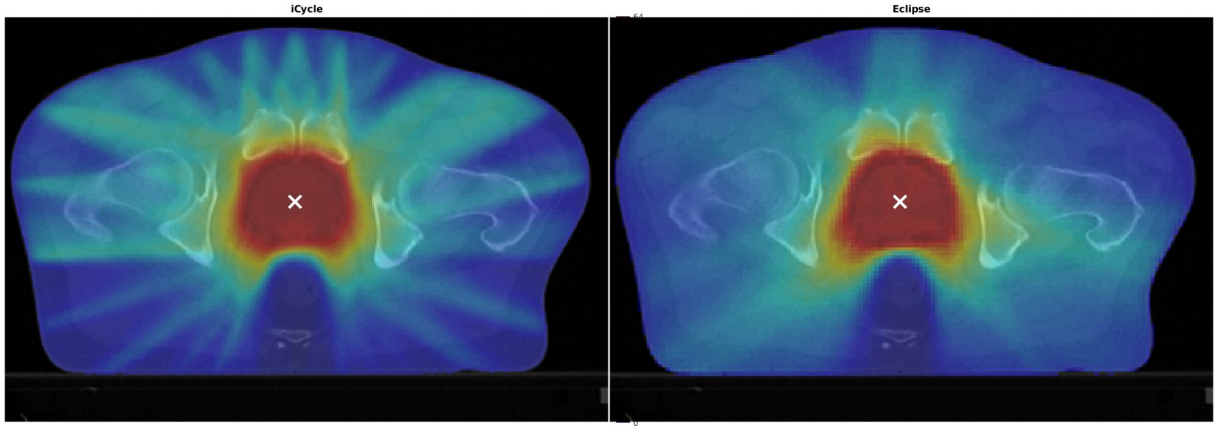

(b) Transverse Dose Distribution: Transverse dose distribution for iCycle (left) and Eclipse (right) plans. The iCycle plan exhibits a more modulated dose pattern, whereas Eclipse results in a smoother dose fall-off. The PTV coverage is comparable, but there are visible differences in dose spillage and modulation.

Figure A.3: Comparison of Dose Distribution and DVH Between Erasmus-iCycle and Eclipse Plans: Comparison of the dose distribution and DVHs for Patient 3, illustrating the differences between the iCycle (pre-optimized) and Eclipse (final optimized) VMAT plans. The bottom subfigure shows the transverse dose distributions, while the top subfigure presents the DVH analysis of the PTV and OARs.

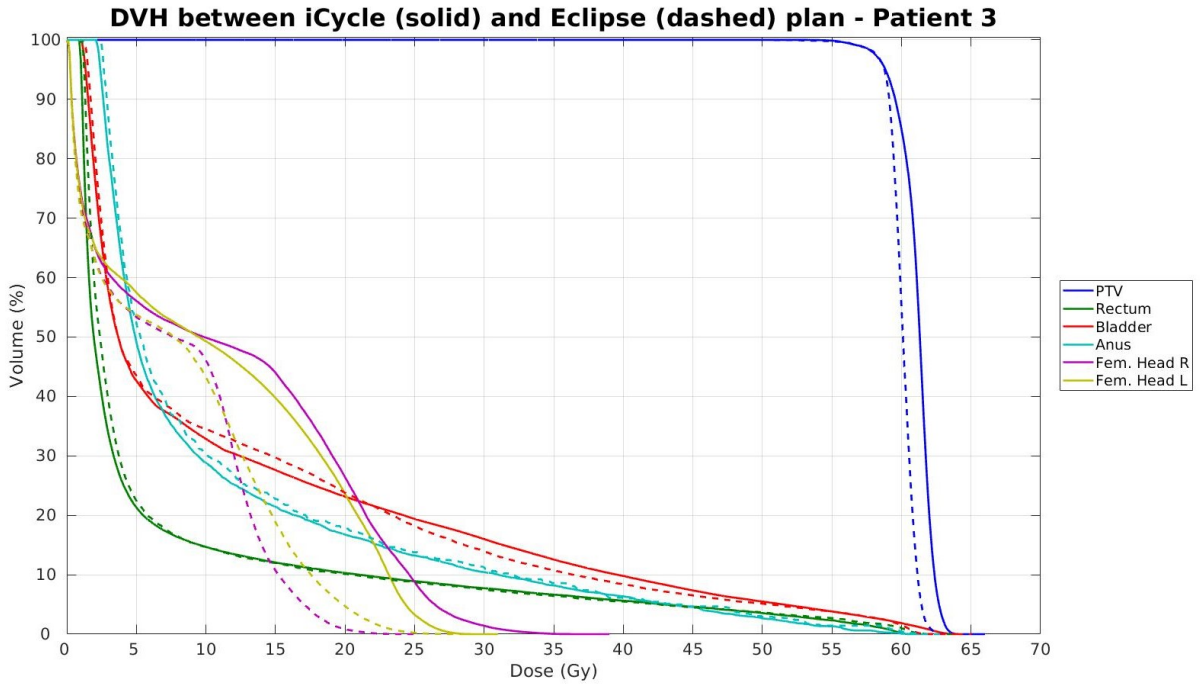

(a) Dose-Volume Histogram : DVH comparison for Patient 3, showing dose distributions for the PTV and OARs. The iCycle plan (solid lines) achieves better OAR sparing, particularly for the bladder and rectum, while maintaining target coverage, compared to the Eclipse plan (dashed lines).

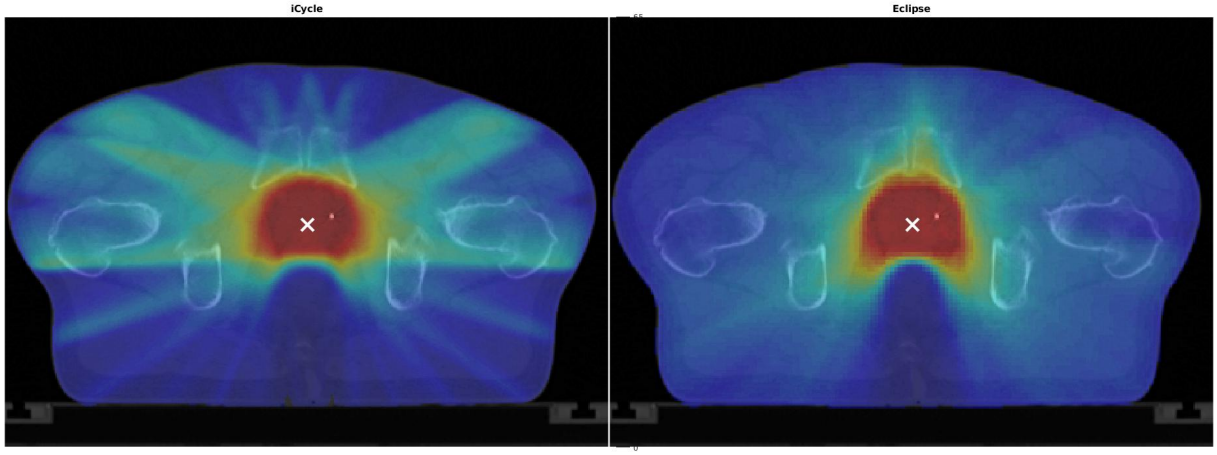

(b) Transverse Dose Distribution: Transverse dose distribution for iCycle (left) and Eclipse (right) plans. The iCycle plan exhibits a more modulated dose pattern, whereas Eclipse results in a smoother dose fall-off. The PTV coverage is comparable, but there are visible differences in dose spillage and modulation.

Figure A.4: Comparison of Dose Distribution and DVH Between Erasmus-iCycle and Eclipse Plans: Comparison of the dose distribution and DVHs for Patient 4, illustrating the differences between the iCycle (pre-optimized) and Eclipse (final optimized) VMAT plans. The bottom subfigure shows the transverse dose distributions, while the top subfigure presents the DVH analysis of the PTV and OARs.

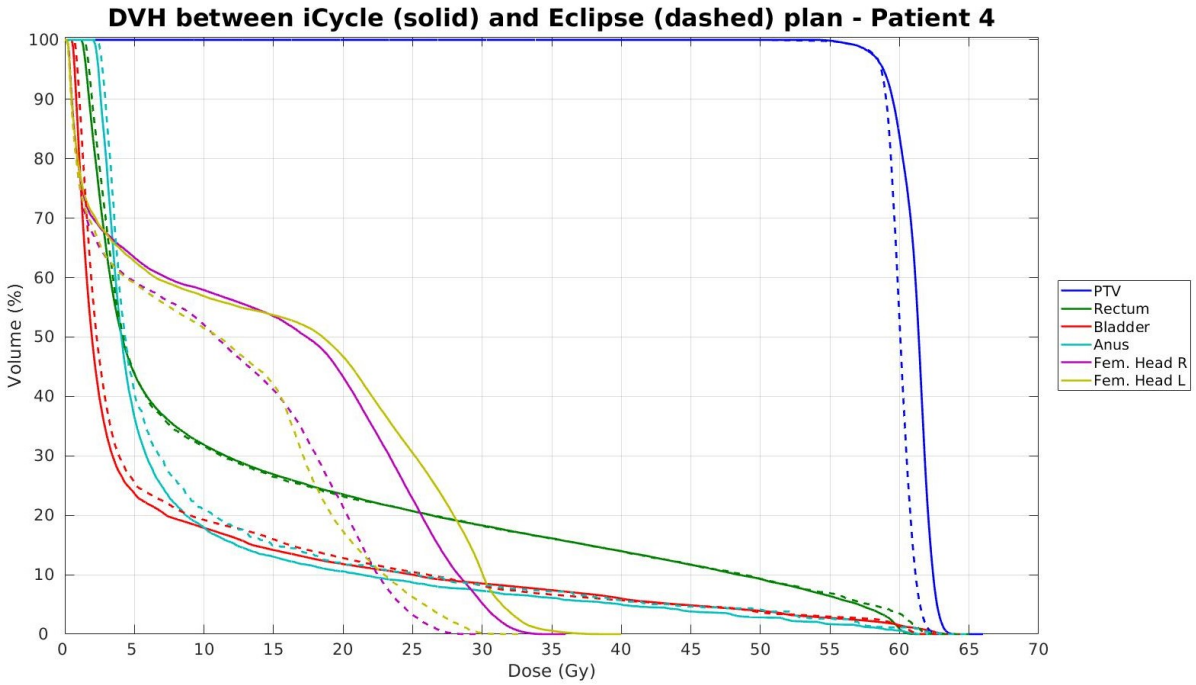

(a) Dose-Volume Histogram : DVH comparison for Patient 4, showing dose distributions for the PTV and OARs. The iCycle plan (solid lines) achieves better OAR sparing, particularly for the bladder and rectum, while maintaining target coverage, compared to the Eclipse plan (dashed lines).

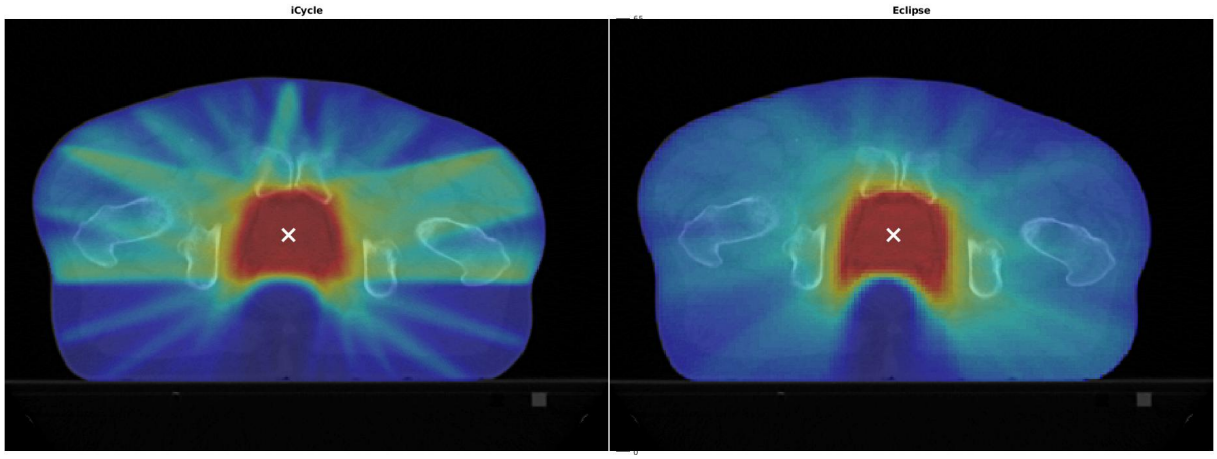

(b) Transverse Dose Distribution: Transverse dose distribution for iCycle (left) and Eclipse (right) plans. The iCycle plan exhibits a more modulated dose pattern, whereas Eclipse results in a smoother dose fall-off. The PTV coverage is comparable, but there are visible differences in dose spillage and modulation.

Figure A.5: Comparison of Dose Distribution and DVH Between Erasmus-iCycle and Eclipse Plans: Comparison of the dose distribution and DVHs for Patient 5, illustrating the differences between the iCycle (pre-optimized) and Eclipse (final optimized) VMAT plans. The bottom subfigure shows the transverse dose distributions, while the top subfigure presents the DVH analysis of the PTV and OARs.

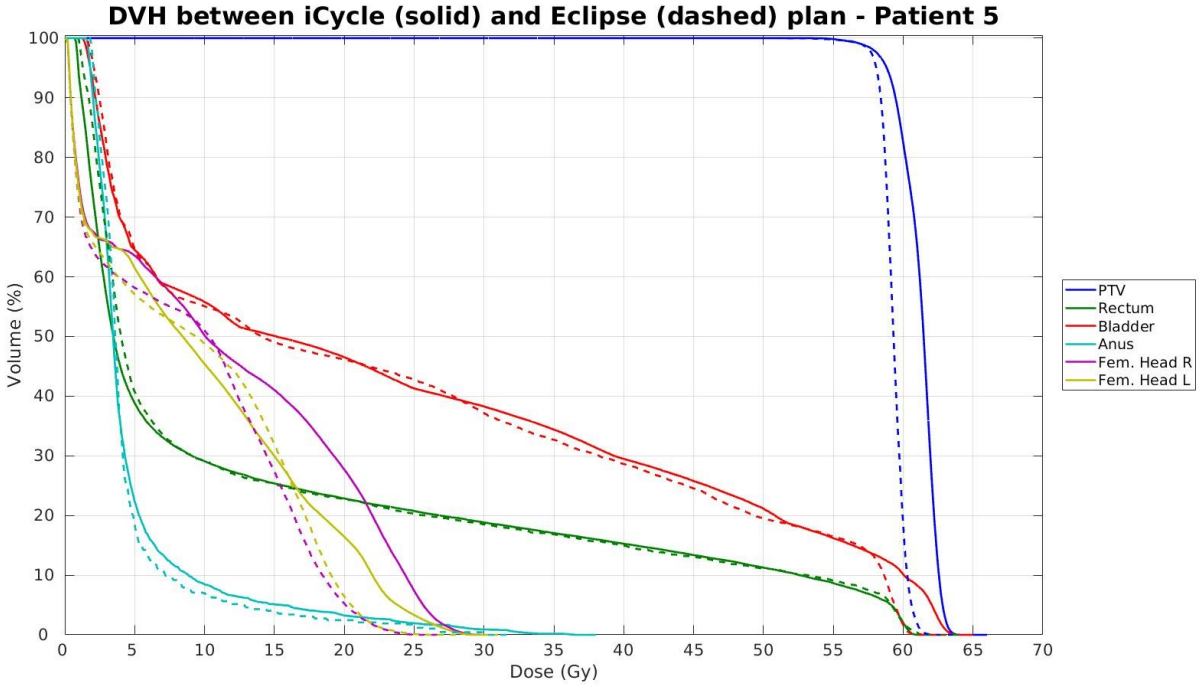

(a) Dose-Volume Histogram : DVH comparison for Patient 5, showing dose distributions for the PTV and OARs. The iCycle plan (solid lines) achieves better OAR sparing, particularly for the bladder and rectum, while maintaining target coverage, compared to the Eclipse plan (dashed lines).

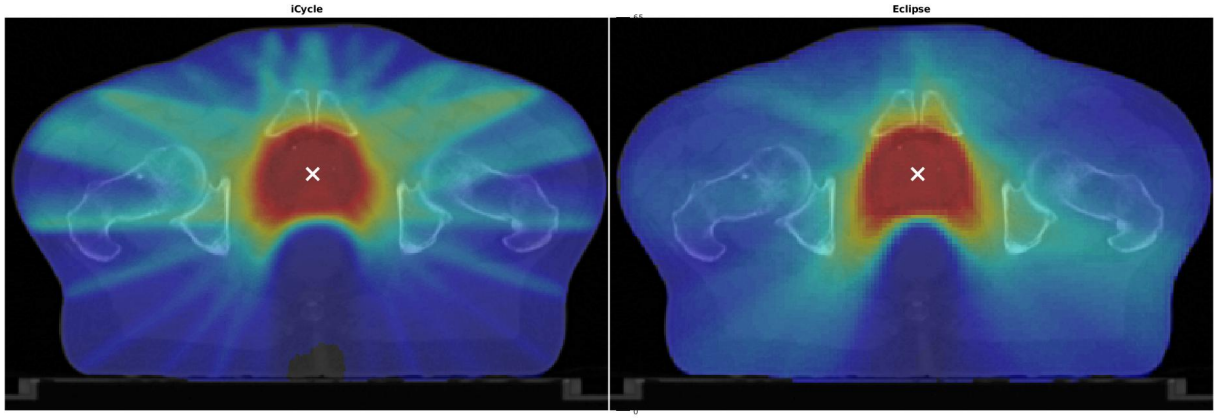

(b) Transverse Dose Distribution: Transverse dose distribution for iCycle (left) and Eclipse (right) plans. The iCycle plan exhibits a more modulated dose pattern, whereas Eclipse results in a smoother dose fall-off. The PTV coverage is comparable, but there are visible differences in dose spillage and modulation.

Figure A.6: Comparison of Dose Distribution and DVH Between Erasmus-iCycle and Eclipse Plans: Comparison of the dose distribution and DVHs for Patient 7, illustrating the differences between the iCycle (pre-optimized) and Eclipse (final optimized) VMAT plans. The bottom subfigure shows the transverse dose distributions, while the top subfigure presents the DVH analysis of the PTV and OARs.

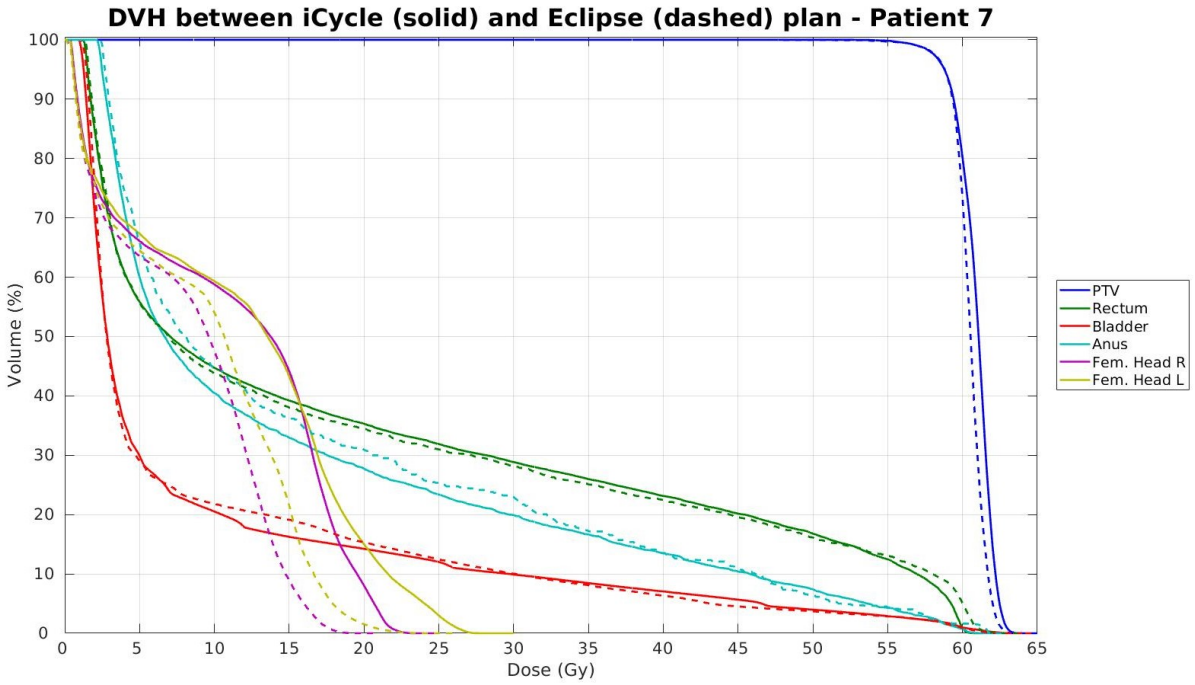

(a) Dose-Volume Histogram : DVH comparison for Patient 7, showing dose distributions for the PTV and OARs. The iCycle plan (solid lines) achieves better OAR sparing, particularly for the bladder and rectum, while maintaining target coverage, compared to the Eclipse plan (dashed lines).

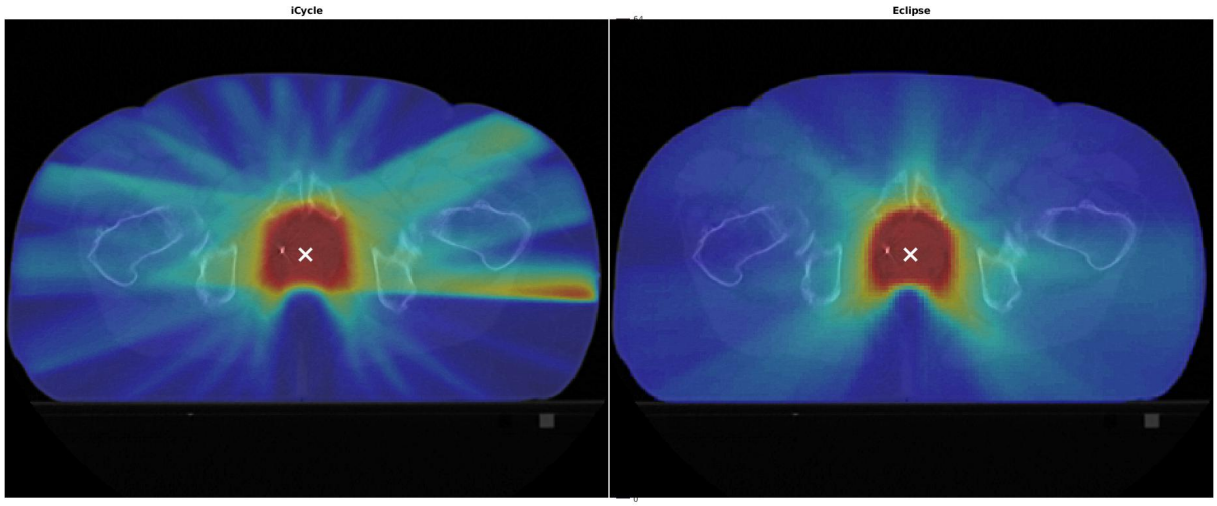

(b) Transverse Dose Distribution: Transverse dose distribution for iCycle (left) and Eclipse (right) plans. The iCycle plan exhibits a more modulated dose pattern, whereas Eclipse results in a smoother dose fall-off. The PTV coverage is comparable, but there are visible differences in dose spillage and modulation.

Figure A.7: Comparison of Dose Distribution and DVH Between Erasmus-iCycle and Eclipse Plans: Comparison of the dose distribution and DVHs for Patient 8, illustrating the differences between the iCycle (pre-optimized) and Eclipse (final optimized) VMAT plans. The bottom subfigure shows the transverse dose distributions, while the top subfigure presents the DVH analysis of the PTV and OARs.

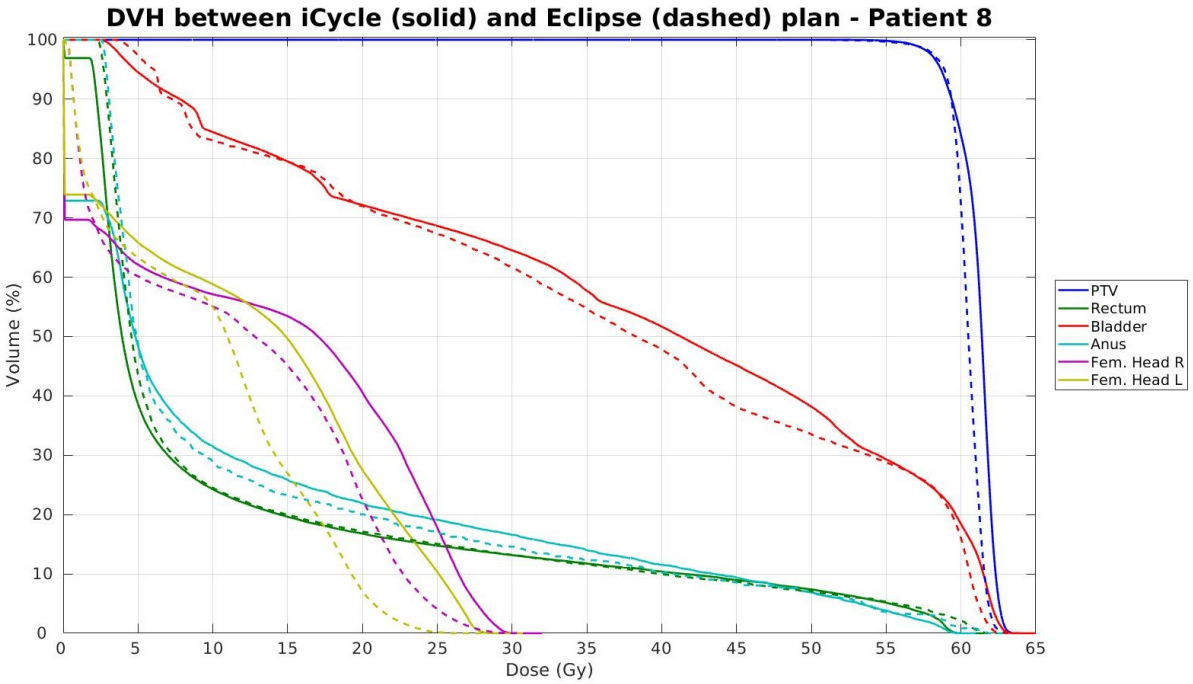

(a) Dose-Volume Histogram : DVH comparison for Patient 8, showing dose distributions for the PTV and OARs. The iCycle plan (solid lines) achieves better OAR sparing, particularly for the bladder and rectum, while maintaining target coverage, compared to the Eclipse plan (dashed lines).

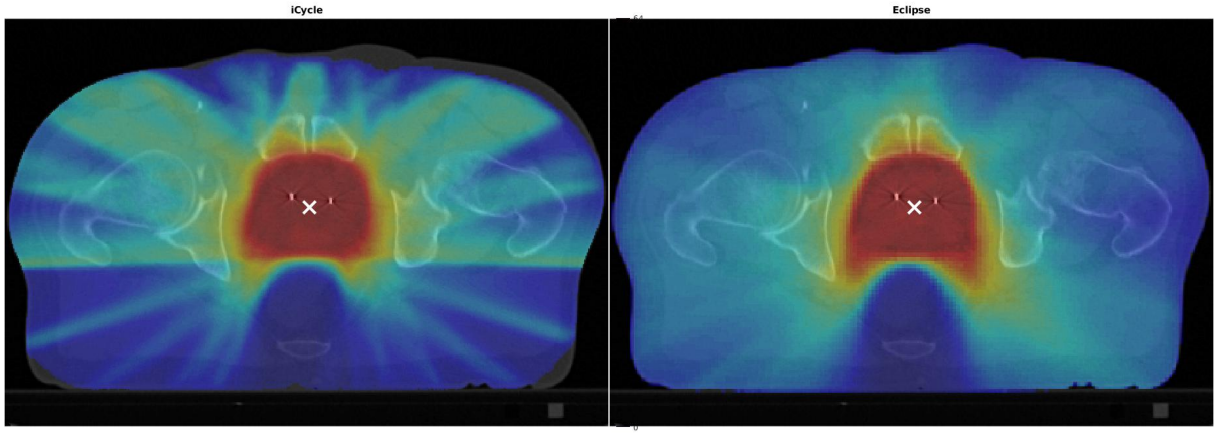

(b) Transverse Dose Distribution: Transverse dose distribution for iCycle (left) and Eclipse (right) plans. The iCycle plan exhibits a more modulated dose pattern, whereas Eclipse results in a smoother dose fall-off. The PTV coverage is comparable, but there are visible differences in dose spillage and modulation.

Figure A.8: Comparison of Dose Distribution and DVH Between Erasmus-iCycle and Eclipse Plans: Comparison of the dose distribution and DVHs for Patient 9, illustrating the differences between the iCycle (pre-optimized) and Eclipse (final optimized) VMAT plans. The bottom subfigure shows the transverse dose distributions, while the top subfigure presents the DVH analysis of the PTV and OARs.

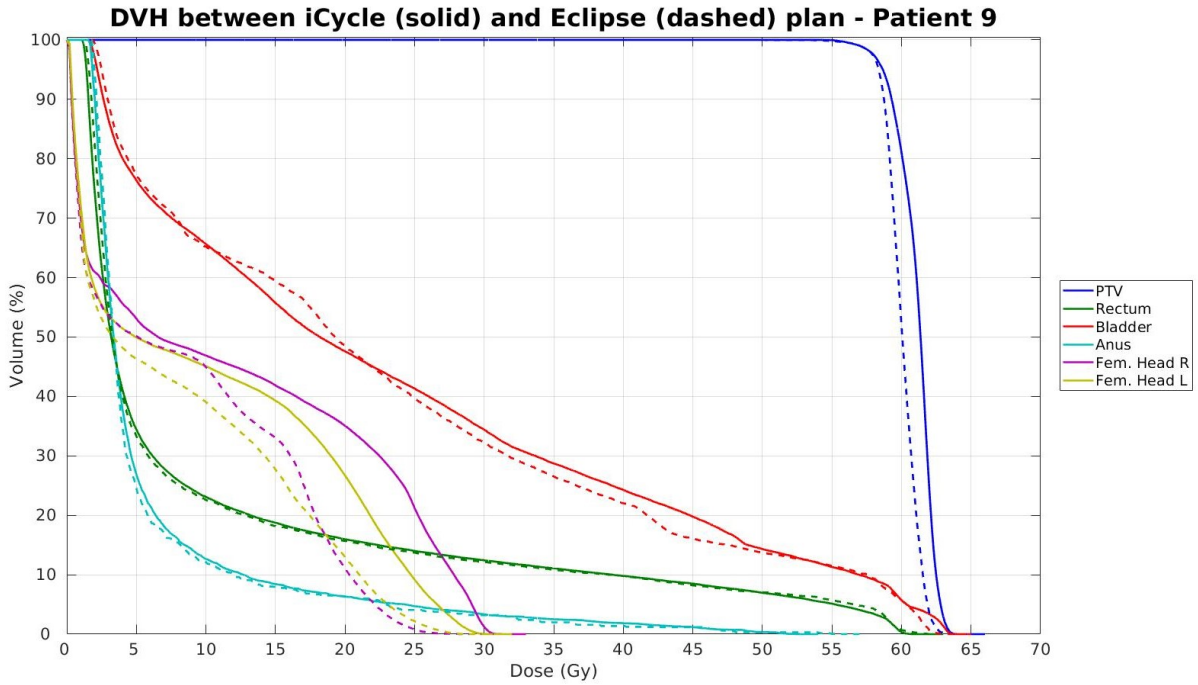

(a) Dose-Volume Histogram : DVH comparison for Patient 9, showing dose distributions for the PTV and OARs. The iCycle plan (solid lines) achieves better OAR sparing, particularly for the bladder and rectum, while maintaining target coverage, compared to the Eclipse plan (dashed lines).

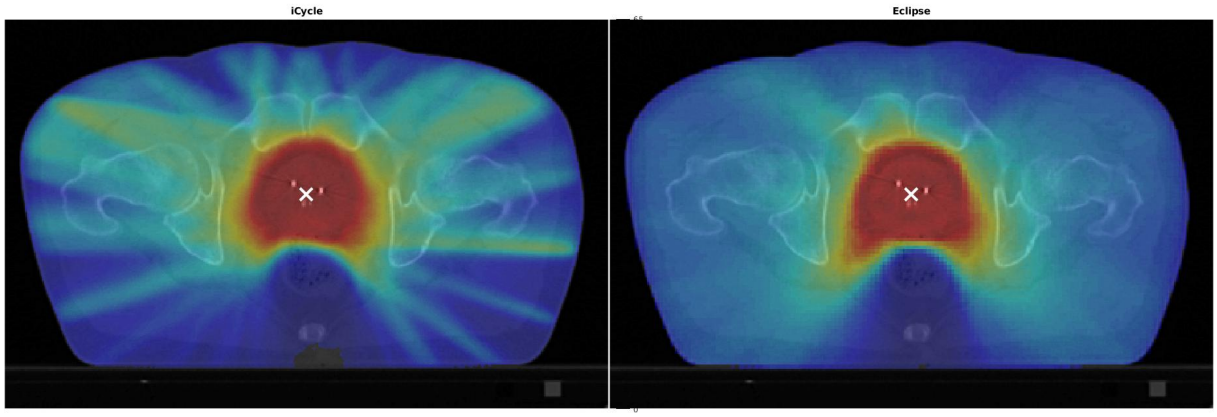

(b) Transverse Dose Distribution: Transverse dose distribution for iCycle (left) and Eclipse (right) plans. The iCycle plan exhibits a more modulated dose pattern, whereas Eclipse results in a smoother dose fall-off. The PTV coverage is comparable, but there are visible differences in dose spillage and modulation.

Figure A.9: Comparison of Dose Distribution and DVH Between Erasmus-iCycle and Eclipse Plans: Comparison of the dose distribution and DVHs for Patient 10, illustrating the differences between the iCycle (pre-optimized) and Eclipse (final optimized) VMAT plans. The bottom subfigure shows the transverse dose distributions, while the top subfigure presents the DVH analysis of the PTV and OARs.

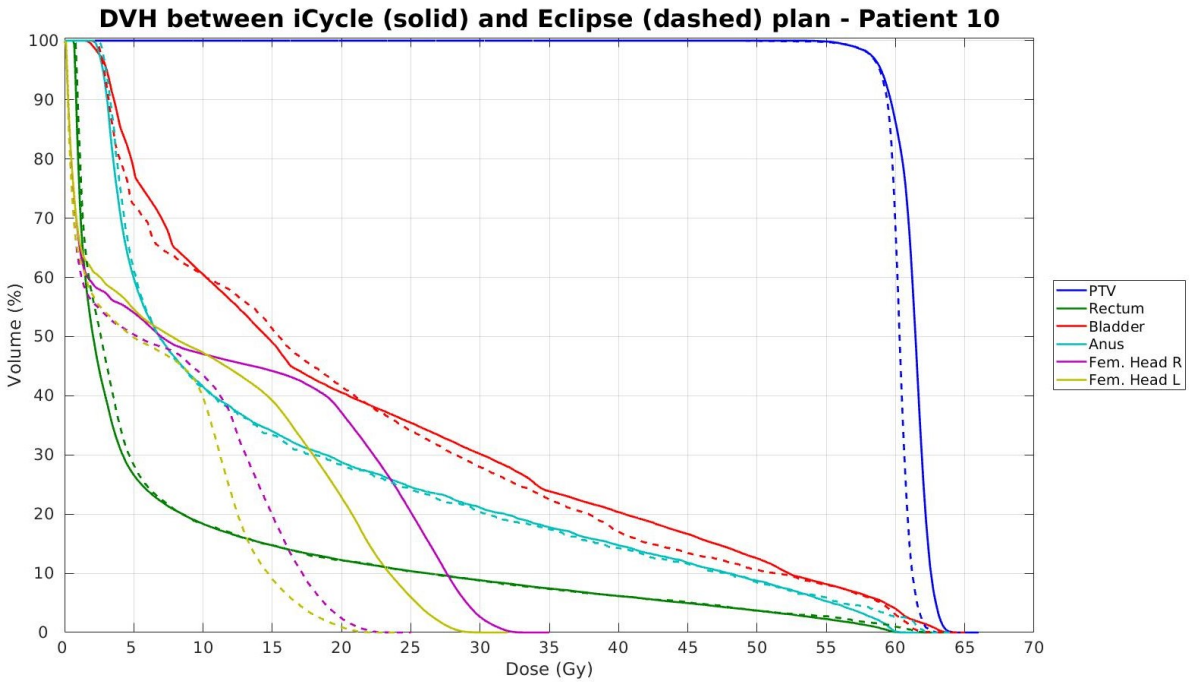

(a) Dose-Volume Histogram : DVH comparison for Patient 10, showing dose distributions for the PTV and OARs. The iCycle plan (solid lines) achieves better OAR sparing, particularly for the bladder and rectum, while maintaining target coverage, compared to the Eclipse plan (dashed lines).

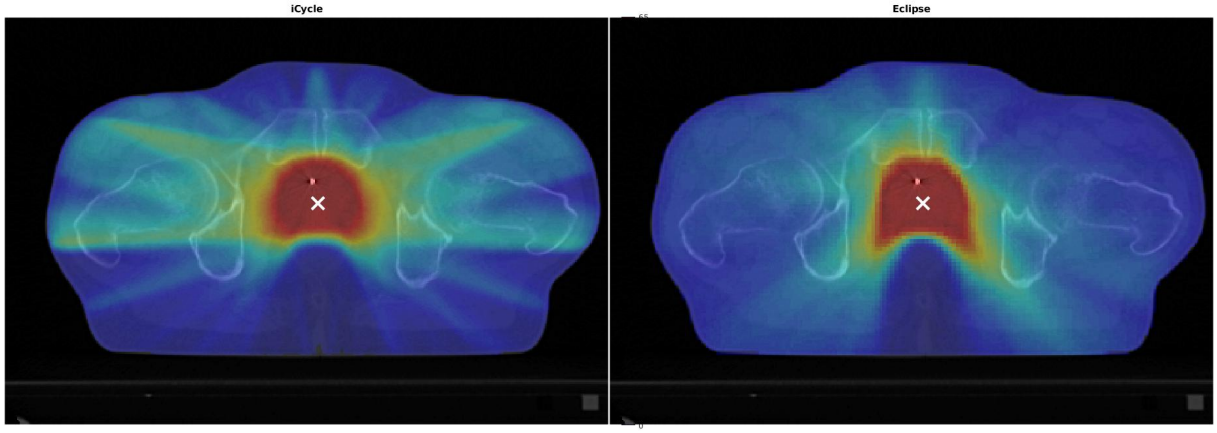

(b) Transverse Dose Distribution: Transverse dose distribution for iCycle (left) and Eclipse (right) plans. The iCycle plan exhibits a more modulated dose pattern, whereas Eclipse results in a smoother dose fall-off. The PTV coverage is comparable, but there are visible differences in dose spillage and modulation.

B SCP-based Optimization: Patient-Specific DVHs and Dose Distributions

Figure B.1: Comparison of dosimetric outcomes between Erasmus-iCycle (left) and SCP-based algorithm (right) for Patient 1. The set includes DVH plots and axial dose distribution images. The DVH demonstrates the consistency in PTV coverage and OAR sparing, while the dose distribution images highlight spatial dose conformity and gradients. The SCP-based plans show comparable dosimetric quality while maintaining clinically acceptable dose limits.

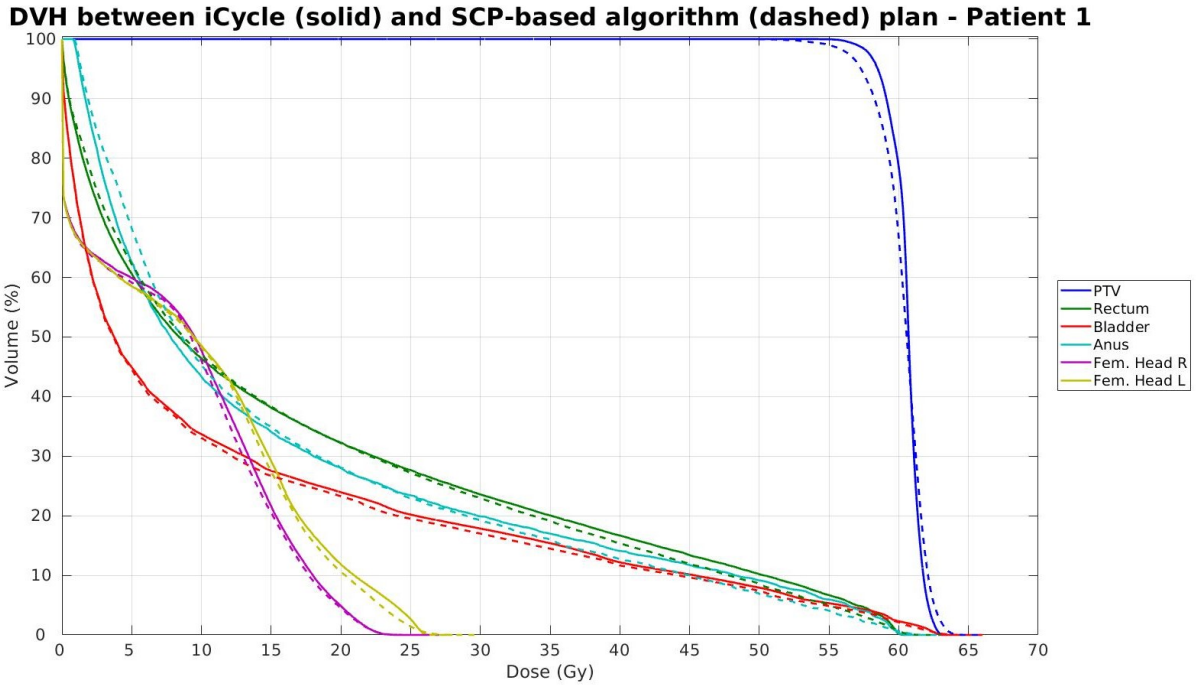

(a) DVH comparison between Erasmus-iCycle (solid) and SCP-based algorithm (dashed) for Patient 1. The plan was generated using 72 control points and a beamlet resolution of $5 \times 5mm$, optimizing all relevant structures. The plot demonstrates the consistency in PTV coverage and OAR sparing achieved by the SCP-based method relative to the benchmark plan.

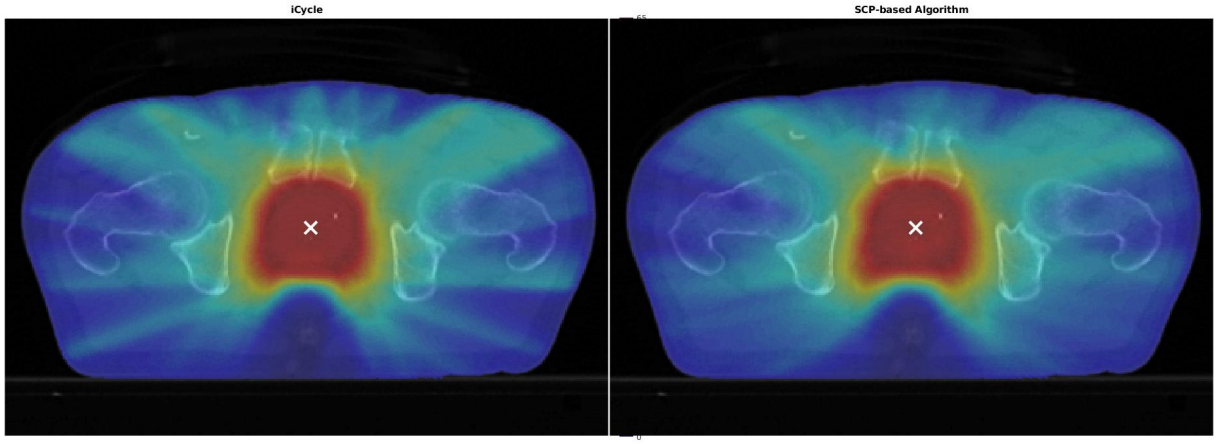

(b) Axial dose distribution, at the isocenter, comparison between Erasmus-iCycle (left) and SCP-based algorithm (right) for Patient 1. The plans were generated using 72 control points and a beamlet resolution of $5 \times 5mm$, optimizing all relevant structures. The images illustrate the spatial dose distribution, highlighting differences in dose conformity and gradients near critical structures.

Figure B.2: Comparison of dosimetric outcomes between Erasmus-iCycle (left) and SCP-based algorithm (right) for Patient 2. The set includes DVH plots and axial dose distribution images. The DVH demonstrates the consistency in PTV coverage and OAR sparing, while the dose distribution images highlight spatial dose conformity and gradients. The SCP-based plans show comparable dosimetric quality while maintaining clinically acceptable dose limits.

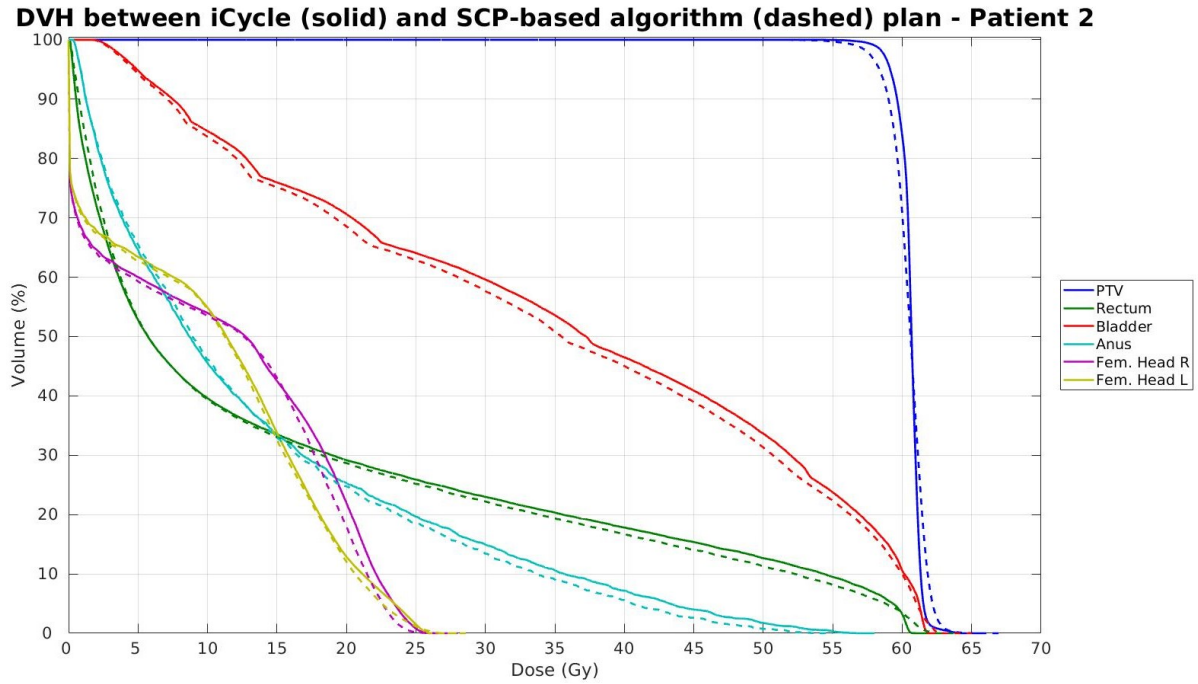

(a) DVH comparison between Erasmus-iCycle (solid) and SCP-based algorithm (dashed) for Patient 2. The plan was generated using 72 control points and a beamlet resolution of $5 \times 5mm$, optimizing all relevant structures. The plot demonstrates the consistency in PTV coverage and OAR sparing achieved by the SCP-based method relative to the benchmark plan.

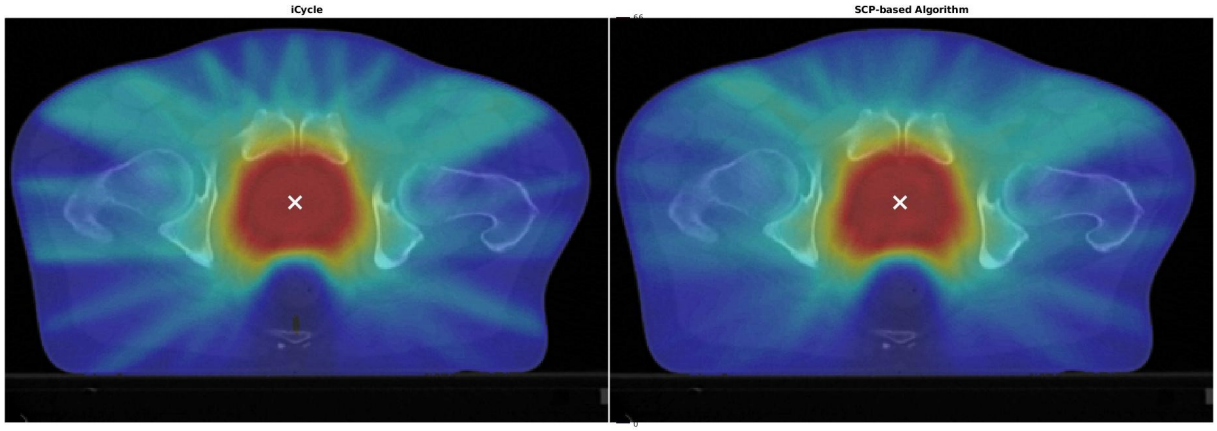

(b) A2ial dose distribution, at the isocenter, comparison between Erasmus-iCycle (left) and SCP-based algorithm (right) for Patient 2. The plans were generated using 72 control points and a beamlet resolution of $5 \times 5mm$, optimizing all relevant structures. The images illustrate the spatial dose distribution, highlighting differences in dose conformity and gradients near critical structures.

Figure B.3: Comparison of dosimetric outcomes between Erasmus-iCycle (left) and SCP-based algorithm (right) for Patient 3. The set includes DVH plots and axial dose distribution images. The DVH demonstrates the consistency in PTV coverage and OAR sparing, while the dose distribution images highlight spatial dose conformity and gradients. The SCP-based plans show comparable dosimetric quality while maintaining clinically acceptable dose limits.

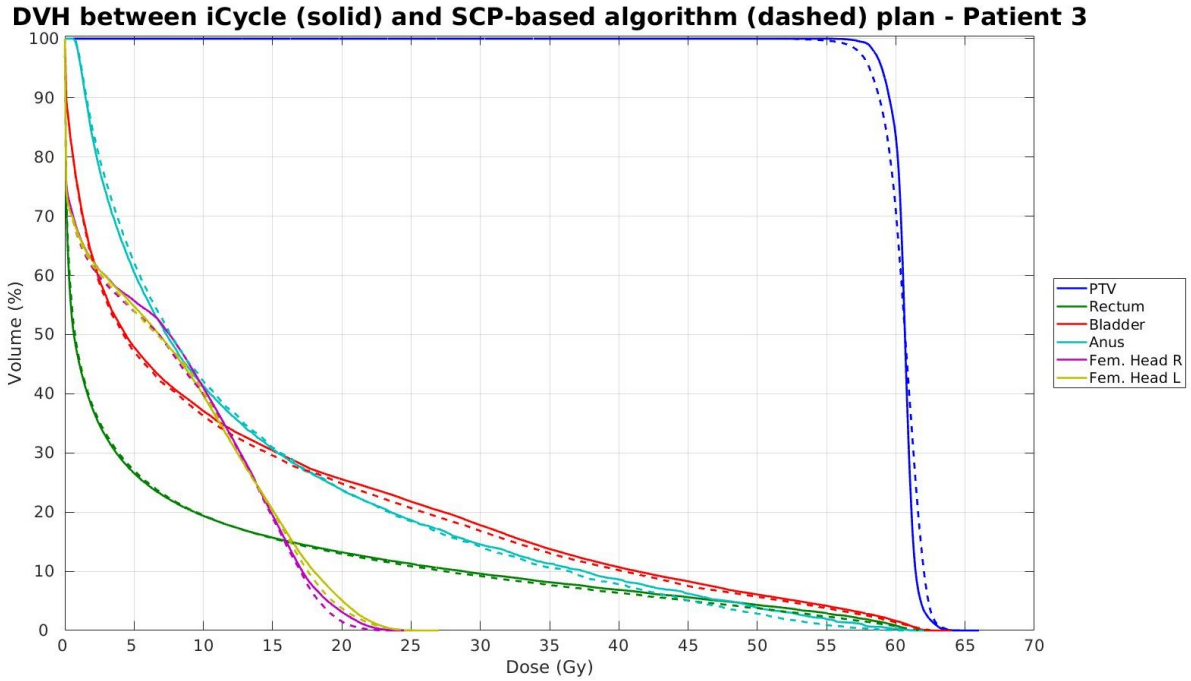

(a) DVH comparison between Erasmus-iCycle (solid) and SCP-based algorithm (dashed) for Patient 3. The plan was generated using 72 control points and a beamlet resolution of $5 \times 5mm$, optimizing all relevant structures. The plot demonstrates the consistency in PTV coverage and OAR sparing achieved by the SCP-based method relative to the benchmark plan.

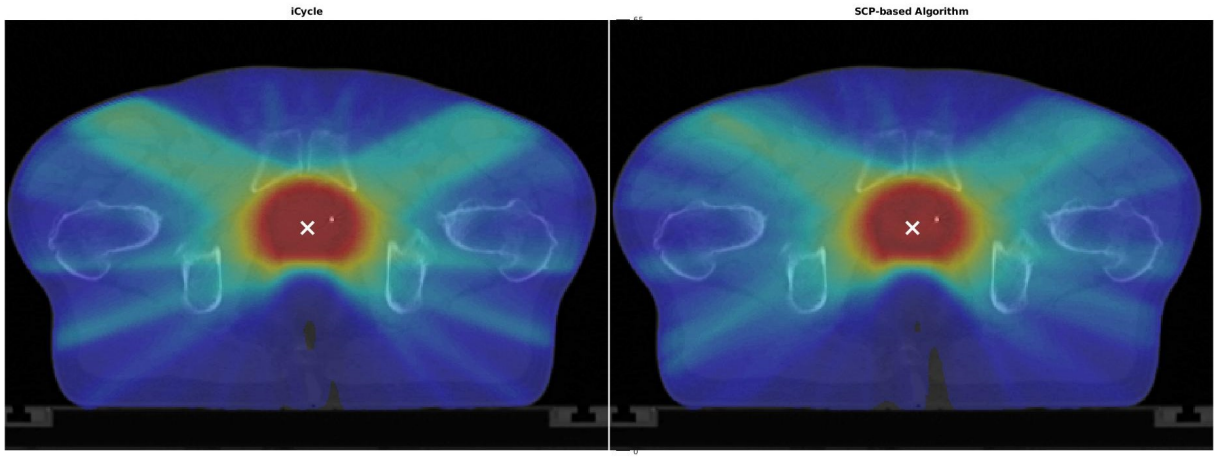

(b) Axial dose distribution, at the isocenter, comparison between Erasmus-iCycle (left) and SCP-based algorithm (right) for Patient 3. The plans were generated using 72 control points and a beamlet resolution of $5 \times 5mm$, optimizing all relevant structures. The images illustrate the spatial dose distribution, highlighting differences in dose conformity and gradients near critical structures.

Figure B.4: Comparison of dosimetric outcomes between Erasmus-iCycle (left) and SCP-based algorithm (right) for Patient 4. The set includes DVH plots and axial dose distribution images. The DVH demonstrates the consistency in PTV coverage and OAR sparing, while the dose distribution images highlight spatial dose conformity and gradients. The SCP-based plans show comparable dosimetric quality while maintaining clinically acceptable dose limits.

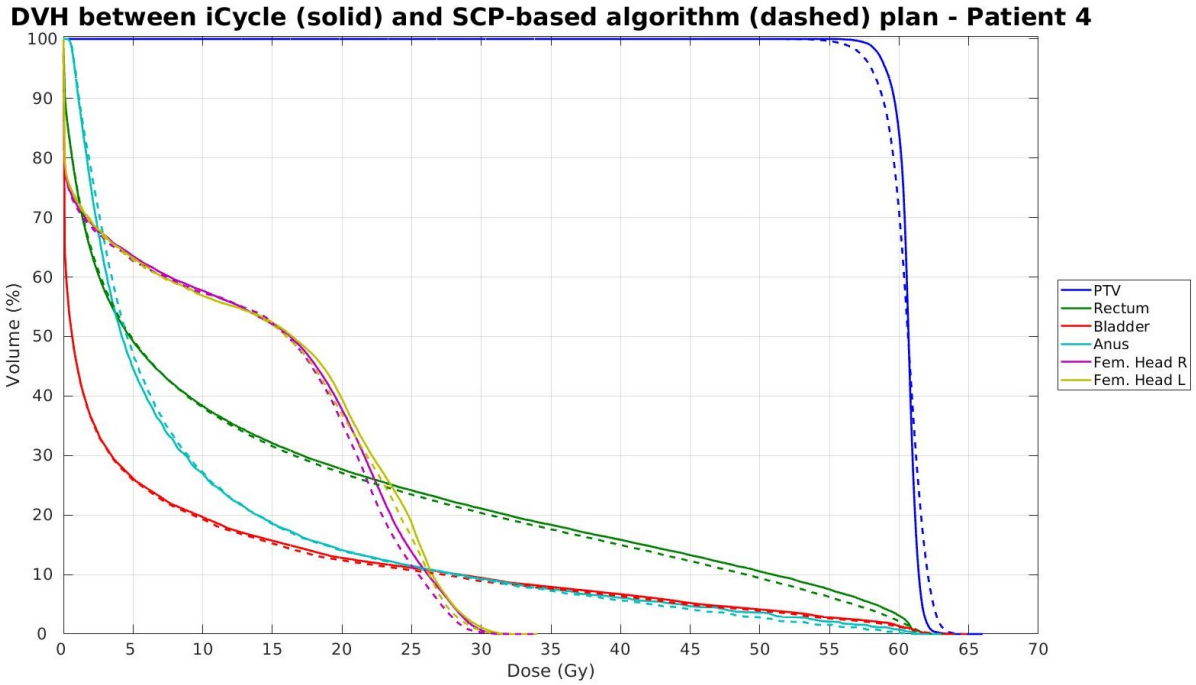

(a) DVH comparison between Erasmus-iCycle (solid) and SCP-based algorithm (dashed) for Patient 4. The plan was generated using 72 control points and a beamlet resolution of $5 \times 5mm$, optimizing all relevant structures. The plot demonstrates the consistency in PTV coverage and OAR sparing achieved by the SCP-based method relative to the benchmark plan.

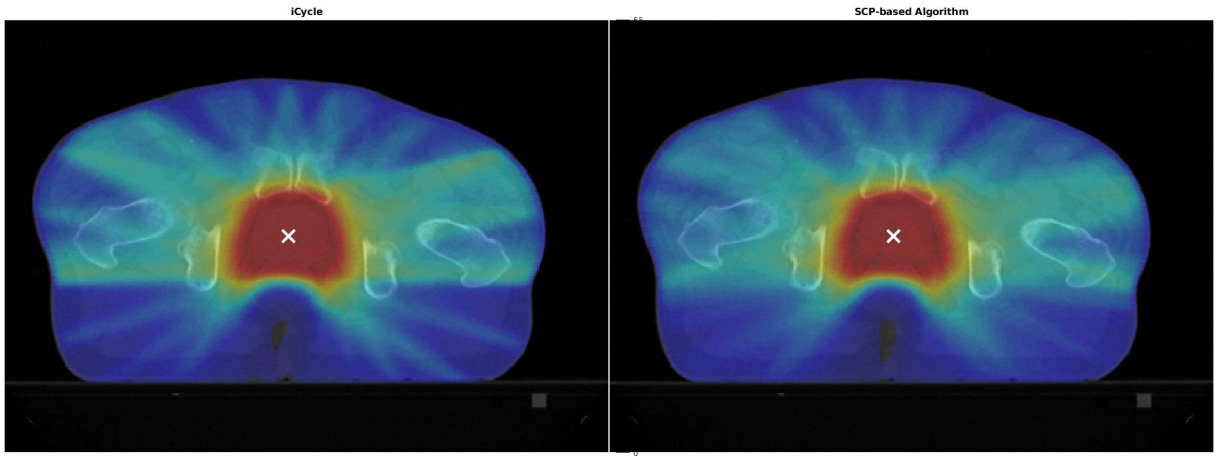

(b) Axial dose distribution, at the isocenter, comparison between Erasmus-iCycle (left) and SCP-based algorithm (right) for Patient 4. The plans were generated using 72 control points and a beamlet resolution of $5 \times 5mm$, optimizing all relevant structures. The images illustrate the spatial dose distribution, highlighting differences in dose conformity and gradients near critical structures.

Figure B.5: Comparison of dosimetric outcomes between Erasmus-iCycle (left) and SCP-based algorithm (right) for Patient 5. The set includes DVH plots and axial dose distribution images. The DVH demonstrates the consistency in PTV coverage and OAR sparing, while the dose distribution images highlight spatial dose conformity and gradients. The SCP-based plans show comparable dosimetric quality while maintaining clinically acceptable dose limits.

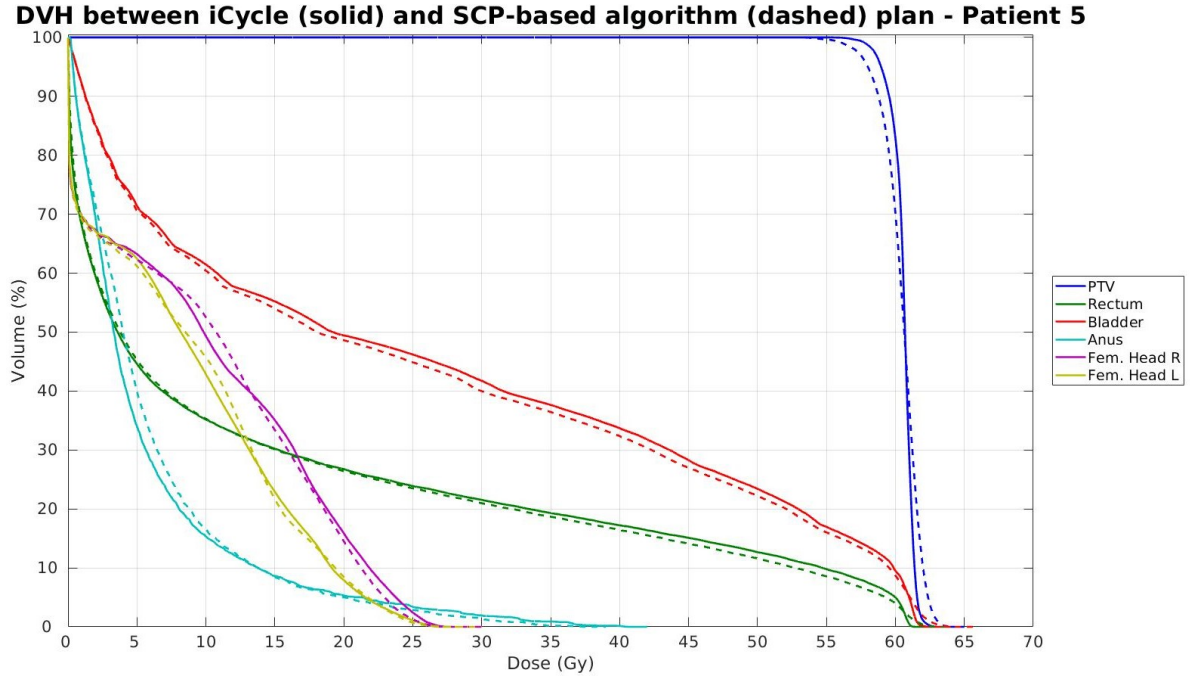

(a) DVH comparison between Erasmus-iCycle (solid) and SCP-based algorithm (dashed) for Patient 5. The plan was generated using 72 control points and a beamlet resolution of $5 \times 5mm$, optimizing all relevant structures. The plot demonstrates the consistency in PTV coverage and OAR sparing achieved by the SCP-based method relative to the benchmark plan.

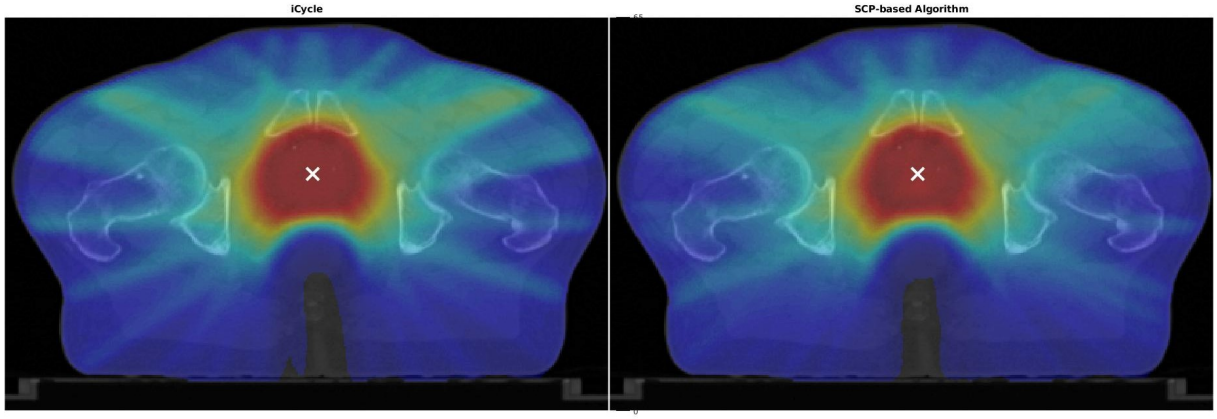

(b) Axial dose distribution, at the isocenter, comparison between Erasmus-iCycle (left) and SCP-based algorithm (right) for Patient 5. The plans were generated using 72 control points and a beamlet resolution of $5 \times 5mm$, optimizing all relevant structures. The images illustrate the spatial dose distribution, highlighting differences in dose conformity and gradients near critical structures.

Figure B.6: Comparison of dosimetric outcomes between Erasmus-iCycle (left) and SCP-based algorithm (right) for Patient 7. The set includes DVH plots and axial dose distribution images. The DVH demonstrates the consistency in PTV coverage and OAR sparing, while the dose distribution images highlight spatial dose conformity and gradients. The SCP-based plans show comparable dosimetric quality while maintaining clinically acceptable dose limits.

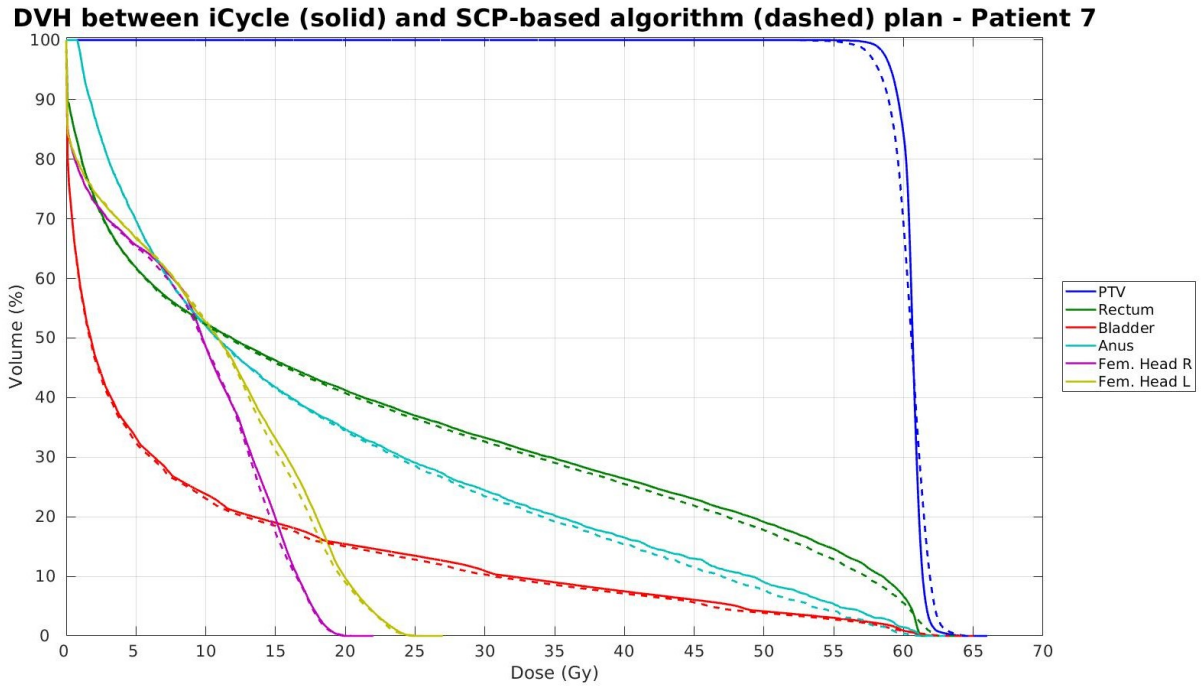

(a) DVH comparison between Erasmus-iCycle (solid) and SCP-based algorithm (dashed) for Patient 7. The plan was generated using 72 control points and a beamlet resolution of $5 \times 5mm$, optimizing all relevant structures. The plot demonstrates the consistency in PTV coverage and OAR sparing achieved by the SCP-based method relative to the benchmark plan.

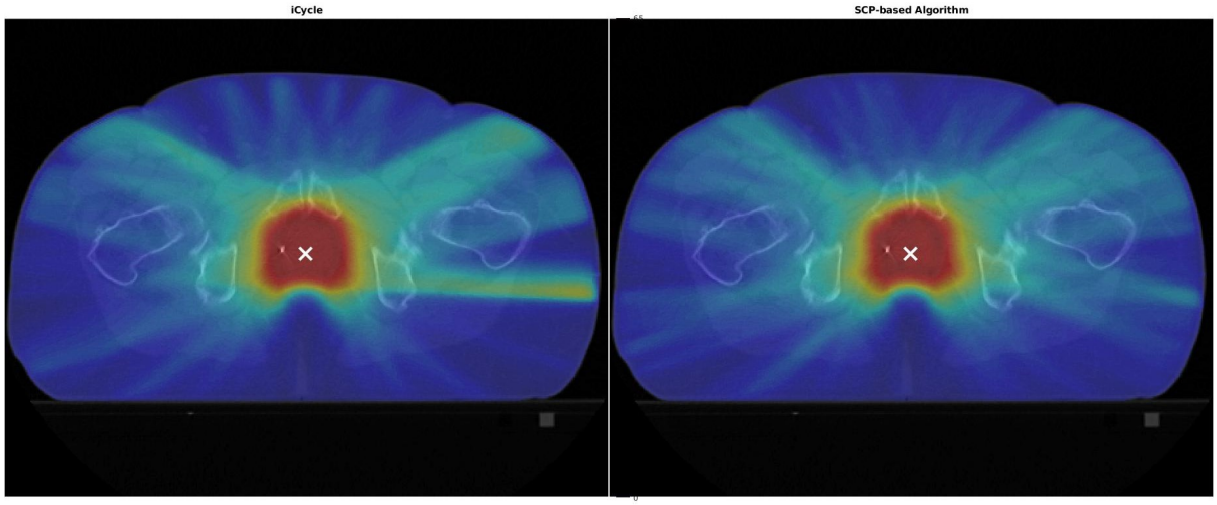

(b) Axial dose distribution, at the isocenter, comparison between Erasmus-iCycle (left) and SCP-based algorithm (right) for Patient 7. The plans were generated using 72 control points and a beamlet resolution of $5 \times 5mm$, optimizing all relevant structures. The images illustrate the spatial dose distribution, highlighting differences in dose conformity and gradients near critical structures.

Figure B.7: Comparison of dosimetric outcomes between Erasmus-iCycle (left) and SCP-based algorithm (right) for Patient 8. The set includes DVH plots and axial dose distribution images. The DVH demonstrates the consistency in PTV coverage and OAR sparing, while the dose distribution images highlight spatial dose conformity and gradients. The SCP-based plans show comparable dosimetric quality while maintaining clinically acceptable dose limits.

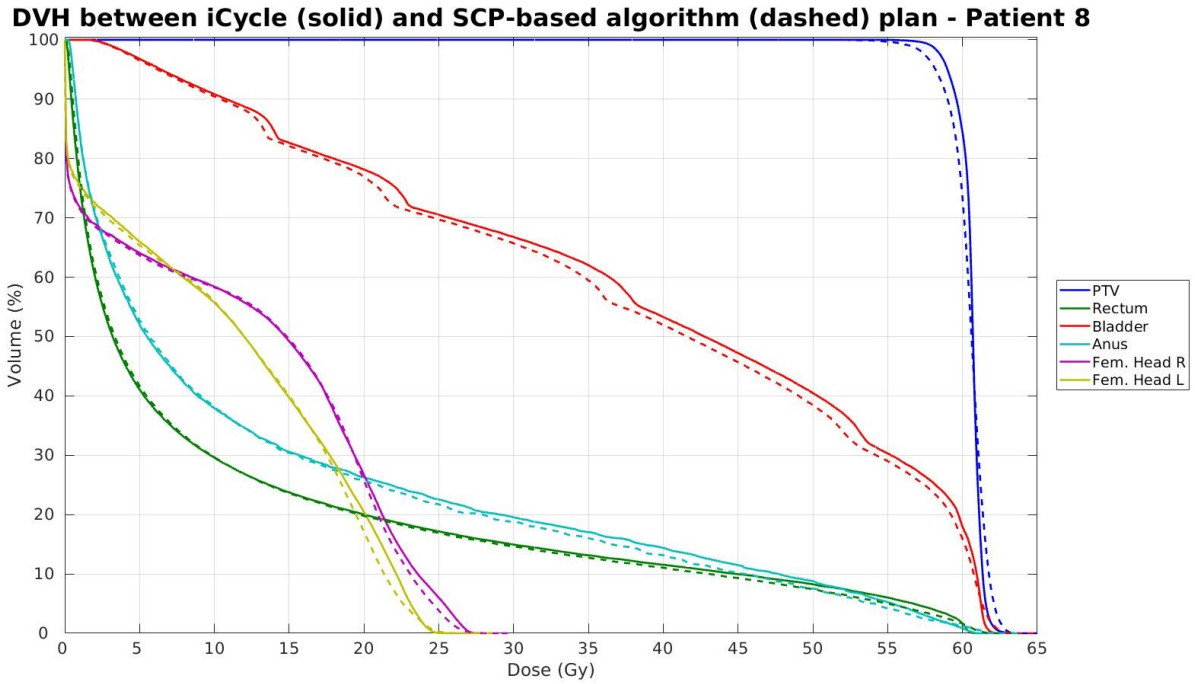

(a) DVH comparison between Erasmus-iCycle (solid) and SCP-based algorithm (dashed) for Patient 8. The plan was generated using 72 control points and a beamlet resolution of $5 \times 5mm$, optimizing all relevant structures. The plot demonstrates the consistency in PTV coverage and OAR sparing achieved by the SCP-based method relative to the benchmark plan.

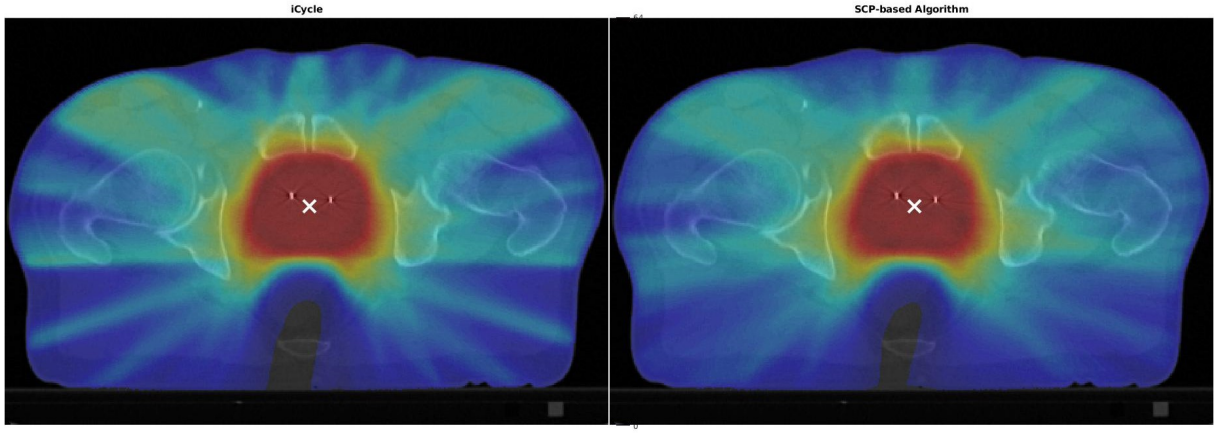

(b) Axial dose distribution, at the isocenter, comparison between Erasmus-iCycle (left) and SCP-based algorithm (right) for Patient 8. The plans were generated using 72 control points and a beamlet resolution of $5 \times 5mm$, optimizing all relevant structures. The images illustrate the spatial dose distribution, highlighting differences in dose conformity and gradients near critical structures.

Figure B.8: Comparison of dosimetric outcomes between Erasmus-iCycle (left) and SCP-based algorithm (right) for Patient 9. The set includes DVH plots and axial dose distribution images. The DVH demonstrates the consistency in PTV coverage and OAR sparing, while the dose distribution images highlight spatial dose conformity and gradients. The SCP-based plans show comparable dosimetric quality while maintaining clinically acceptable dose limits.

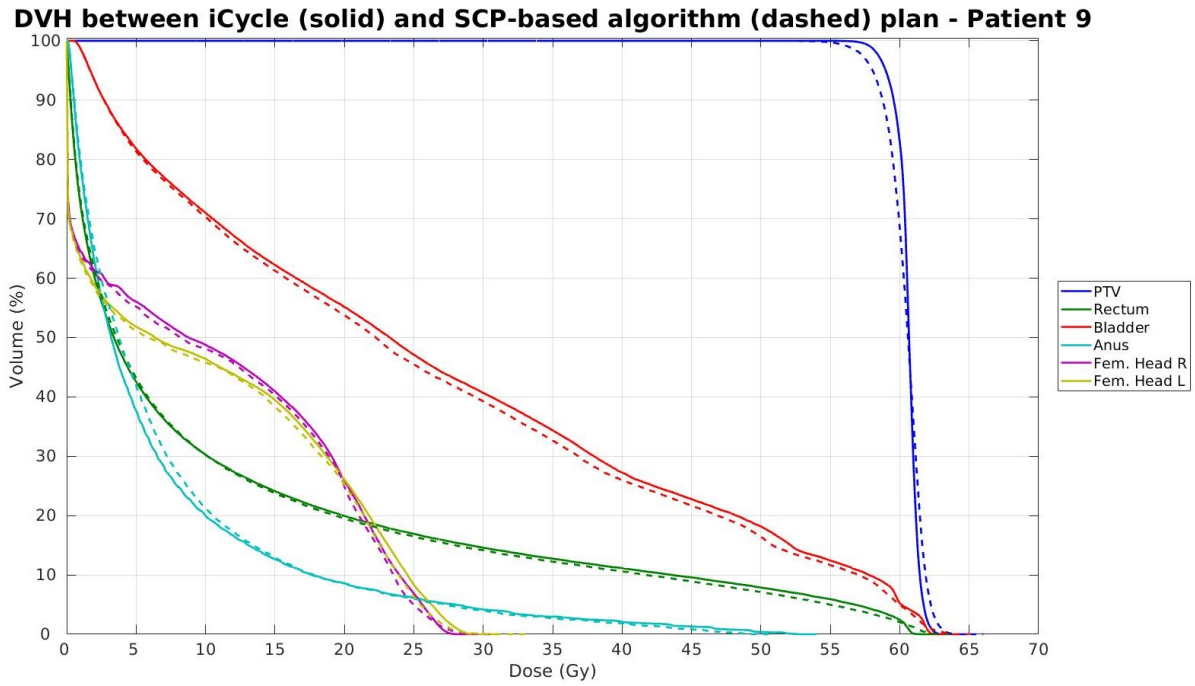

(a) DVH comparison between Erasmus-iCycle (solid) and SCP-based algorithm (dashed) for Patient 9. The plan was generated using 72 control points and a beamlet resolution of $5 \times 5mm$, optimizing all relevant structures. The plot demonstrates the consistency in PTV coverage and OAR sparing achieved by the SCP-based method relative to the benchmark plan.

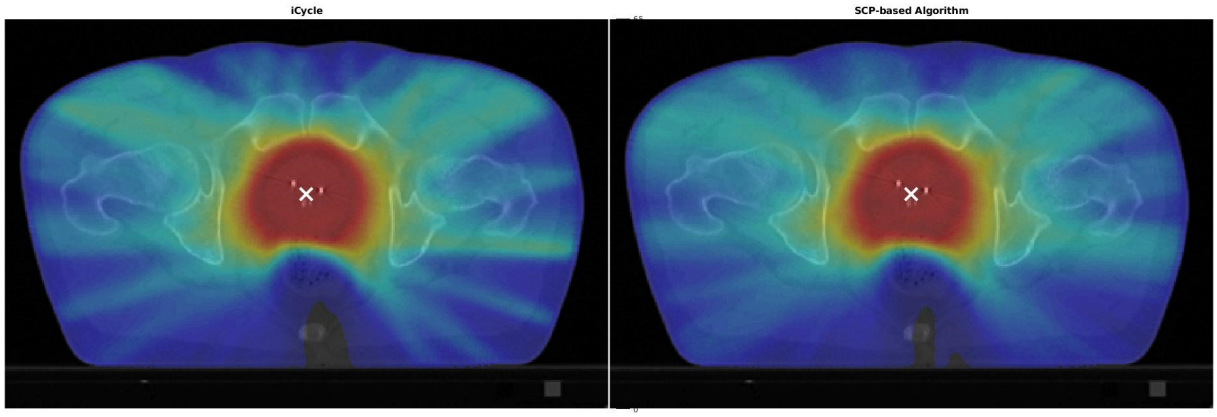

(b) Axial dose distribution, at the isocenter, comparison between Erasmus-iCycle (left) and SCP-based algorithm (right) for Patient X. The plans were generated using 72 control points and a beamlet resolution of $5 \times 5mm$, optimizing all relevant structures. The images illustrate the spatial dose distribution, highlighting differences in dose conformity and gradients near critical structures.

Figure B.9: Comparison of dosimetric outcomes between Erasmus-iCycle (left) and SCP-based algorithm (right) for Patient 10. The set includes DVH plots and axial dose distribution images. The DVH demonstrates the consistency in PTV coverage and OAR sparing, while the dose distribution images highlight spatial dose conformity and gradients. The SCP-based plans show comparable dosimetric quality while maintaining clinically acceptable dose limits.

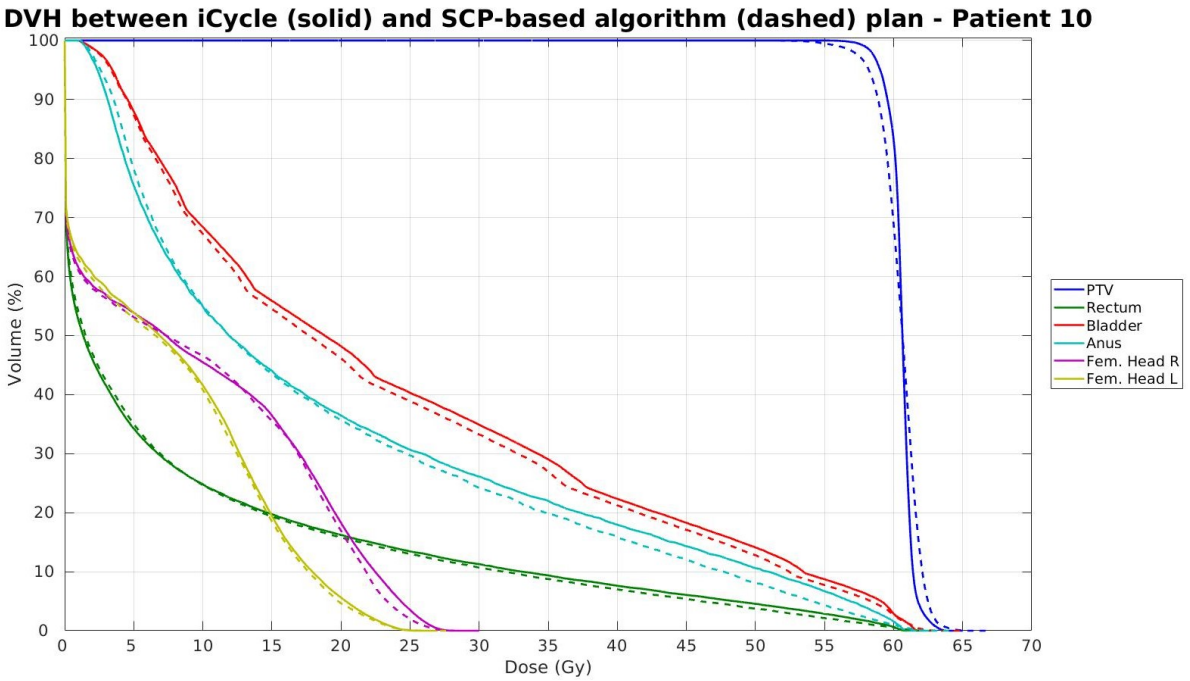

(a) DVH comparison between Erasmus-iCycle (solid) and SCP-based algorithm (dashed) for Patient 10. The plan was generated using 72 control points and a beamlet resolution of $5 \times 5mm$, optimizing all relevant structures. The plot demonstrates the consistency in PTV coverage and OAR sparing achieved by the SCP-based method relative to the benchmark plan.

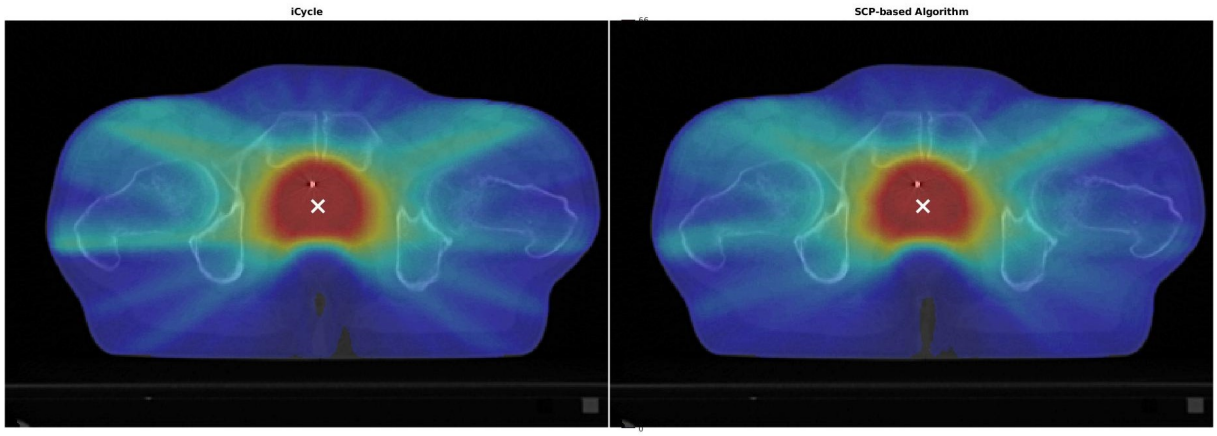

(b) Axial dose distribution, at the isocenter, comparison between Erasmus-iCycle (left) and SCP-based algorithm (right) for Patient 10. The plans were generated using 72 control points and a beamlet resolution of $5 \times 5mm$, optimizing all relevant structures. The images illustrate the spatial dose distribution, highlighting differences in dose conformity and gradients near critical structures.

C Beam-Eye-View (BEV) Segments for Patient 6 - SCP-Based VMAT Plan

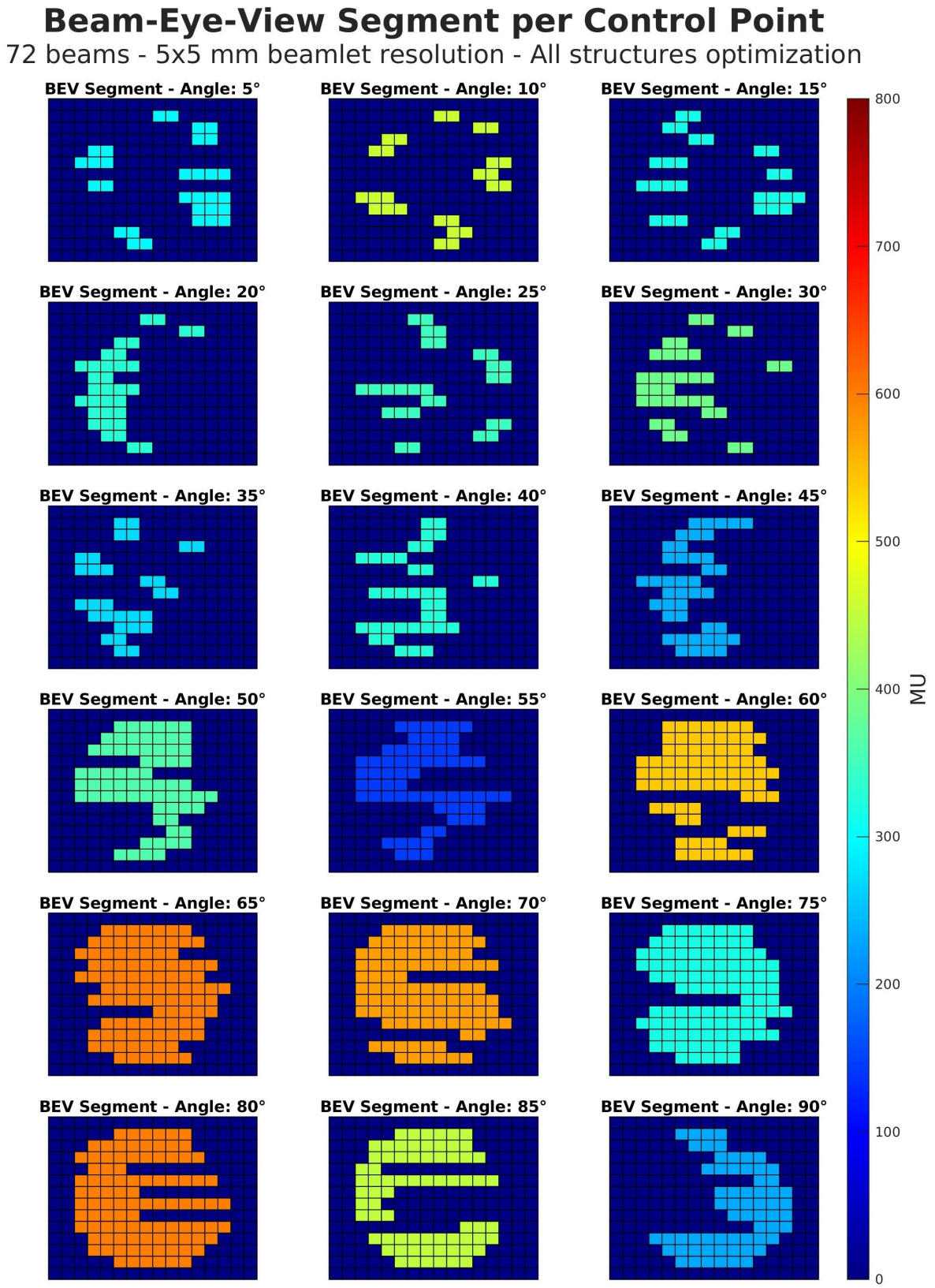

Figure C.1: Beam-Eye-View (BEV) segments for Patient 6, generated by the SCP-based VMAT algorithm with 72 control points and $5 \times 5mm$ beamlet resolution. The figure shows the segment shapes for control point angles from 5° to 90°, highlighting the variability in segment intensity and shape throughout the arc.

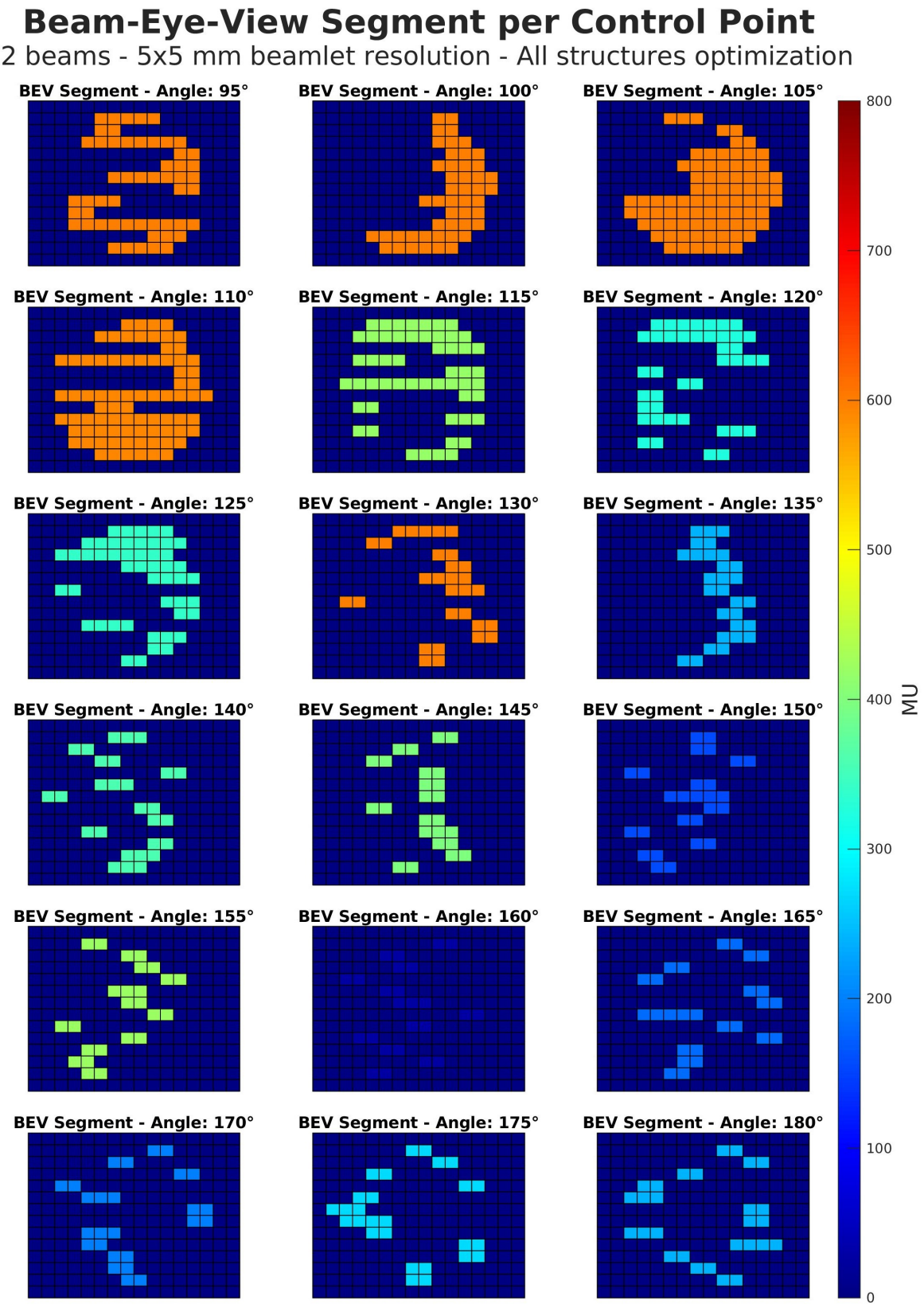

Figure C.2: Beam-Eye-View (BEV) segments for Patient 6, generated by the SCP-based VMAT algorithm with 72 control points and $5 \times 5mm$ beamlet resolution. The figure displays the segment shapes for control point angles from 95° to 180°, demonstrating changes in segment morphology as the gantry rotates.

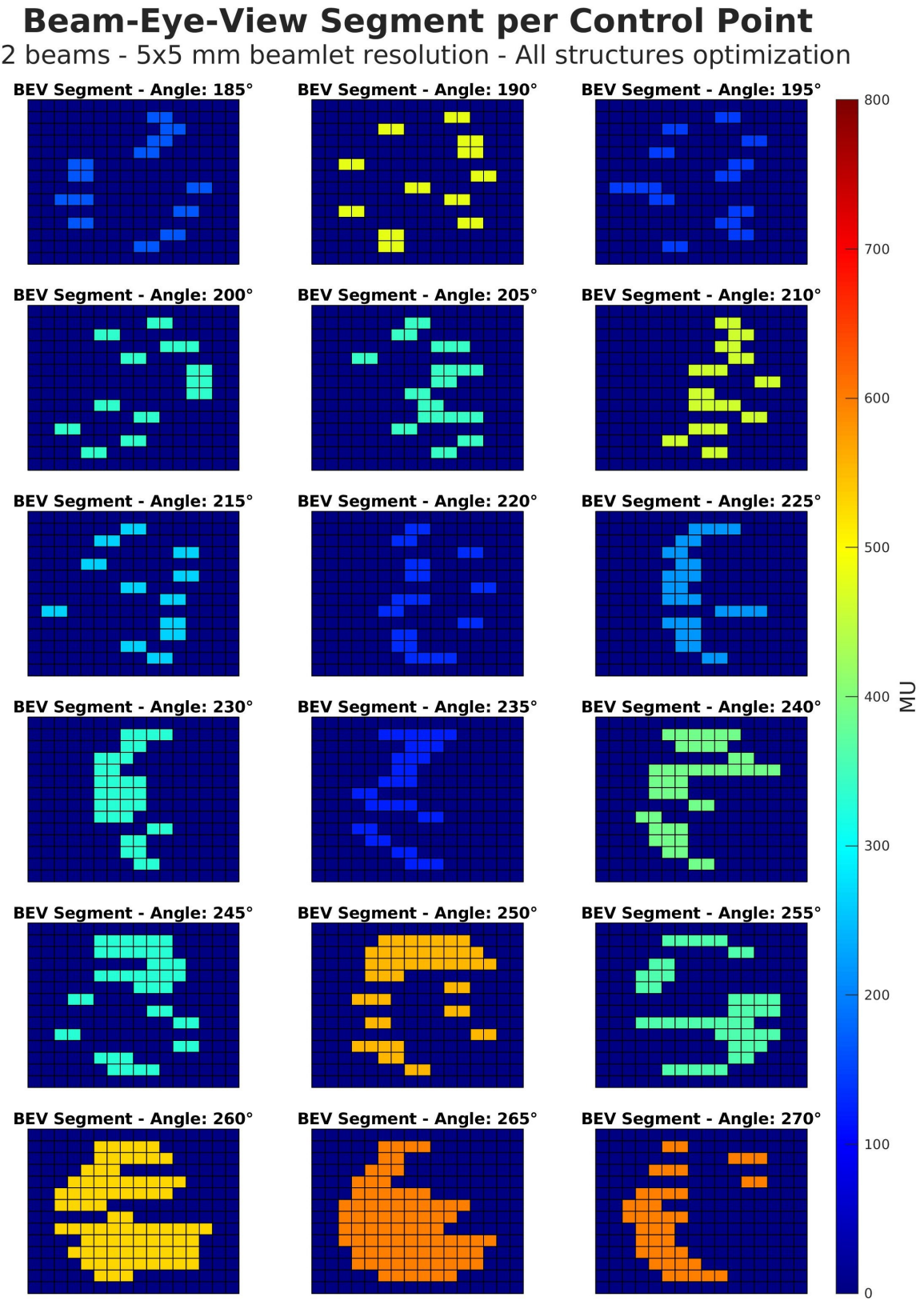

Figure C.3: Beam-Eye-View (BEV) segments for Patient 6, generated by the SCP-based VMAT algorithm with 72 control points and $5 \times 5mm$ beamlet resolution. The figure presents the segment shapes for control point angles from 185° to 270°, illustrating the beam modulation across the posterior and lateral views.

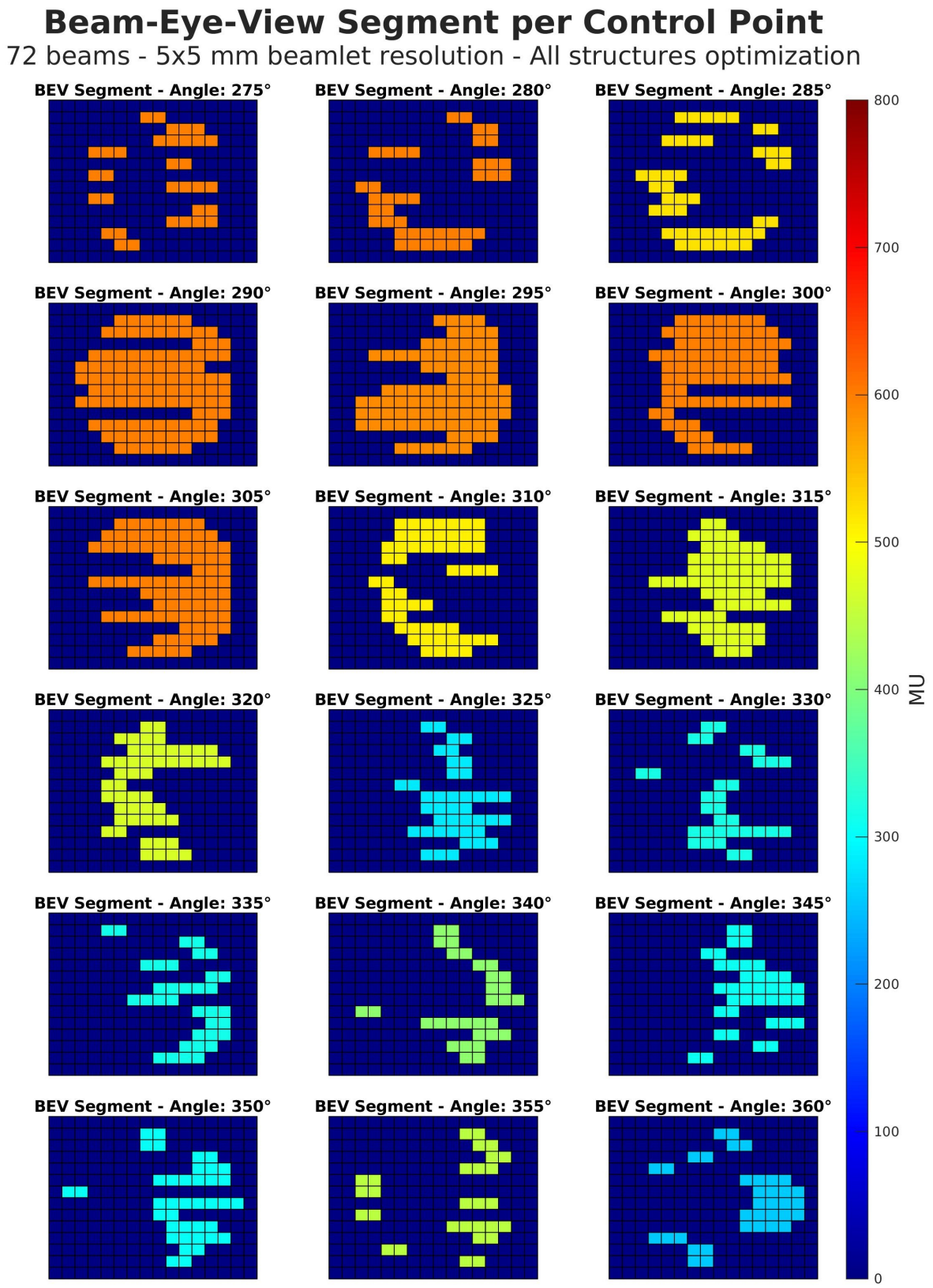

Figure C.4: Beam-Eye-View (BEV) segments for Patient 6, generated by the SCP-based VMAT algorithm with 72 control points and $5 \times 5mm$ beamlet resolution. The figure shows the segment shapes for control point angles from 275° to 360°, covering the final rotation of the gantry.